# Non-Equilibrium Dynamics of Chern Insulators

Caio, Marcello Davide

*Awarding institution:*
King's College London

# Non-Equilibrium Dynamics of Chern Insulators

**Marcello Davide Caio**

*A thesis submitted in partial fulfilment*

*of the requirements for the degree of*

*Doctor of Philosophy in Physics*

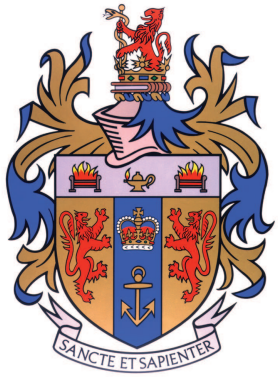


King's College London

Department of Physics

United Kingdom

# Abstract

Topological states of matter exhibit a wealth of novel properties including the exact quantisation of macroscopic observables and the presence of edge states. In this thesis, we study the non-equilibrium dynamics of a class of topological phases, known as Chern insulators. By focusing on the Haldane model, we study quenches between the topological and non-topological phases, and the dynamics induced on physical observables. A notable feature is that the Chern number, calculated for an infinite system, is unchanged under the dynamics following such a quench. However, in finite-size geometries, the initial and final Hamiltonians are distinguished by the presence or absence of edge states. We study the edge excitations and describe their impact on the dynamics of the edge currents and the magnetisation. We show that, following a quantum quench, the edge currents relax towards new steady-state values, and that there is light-cone spreading of the currents into the interior of the sample. The late-time behaviour of the edge currents, after multiple traversals of the sample, is captured by a Generalised Gibbs Ensemble. We further provide an analysis of the Hall response following a quantum quench in an isolated system, with explicit results for the Haldane model. We show that the Hall conductance is no longer related to the Chern number in the post-quench state, in contrast to the equilibrium case. We also discuss the effects of generic open boundary conditions and confinement potentials. Finally, we discuss the impact of disorder on the phases of the Haldane model, both in and out of equilibrium. We conclude with a discussion of ongoing work on the non-equilibrium dynamics of the entanglement spectrum of the Haldane model, and with prospects for further research.

The results presented in Chapters 2 and 3 are published in Refs [1, 2]. The results in Chapter 4 are currently in preparation for publication [3].

*To my parents*

*Giovanna and Mauro Caio*

*with gratitude*

# Acknowledgements

First and foremost, I would like to thank Dr Joe Bhaseen. Throughout my PhD, he has been a mentor for me, more than an advisor. It has been a pleasure to work with him, and this thesis would not have been possible without his encouragement and inputs. I really thank him for his never-ending enthusiasm and optimism.

I am also grateful to Prof. Nigel Cooper, for his expert and invaluable advice, and to Dr Gunnar Möller, for his precious help, especially with some of the numerical aspects of this work. I have gained a lot of experience by collaborating with them.

Throughout the years at King's College London, a number of people have helped me in the most disparate ways, from helping me debugging a code, to offering me a pint, a coffee or a laugh in the right moments. For this, I thank M. Caccin, D. Allen, P. Azarhoosh, A. Le Marois, K. Bożek, A. Beedle, C. Paris, D. Botten, A. Pithis, F. Simkovic, M. Bieniek, M. Stella, A. Fekete, G. Peralta, F. Bianchini, G. Zanda, L. Sponza, G. Doni, *et al.*

Thanks also to Dr David Luke and the Eleusis team for enlightening experiences.

Heartfelt thanks also to D. Gallo, A. Cesari, E. Dipierro, and all of my friends in Milan and around the world for always being close to me despite the distance.

Endless and boundless gratitude goes to my parents Giovanna and Mauro, and to my brother Antonio. Without them, I would not be where I am.

Finally, I am grateful to Claire, for being by my side, for her unconditional support, and for making my days bright.

# Contents

**Abstract** **2**

**Acknowledgements** **4**

**Contents** **5**

**List of Figures** **7**

**Preface** **12**

**1 Introduction** **15**

1.1 Landau Theory . . . . . 15

1.2 Kosterlitz–Thouless Transition . . . . . 16

1.3 Quantum Hall Effect . . . . . 19

1.4 Topological Invariants . . . . . 20

1.5 Haldane Model . . . . . 25

1.6 Topological Insulators . . . . . 29

1.7 Non-Equilibrium Systems . . . . . 30

1.8 Thesis Layout . . . . . 34

**2 Chern Insulators Out of Equilibrium** **36**

2.1 Contributions from the Dirac Points . . . . . 38

2.2 Preservation of the Chern Number . . . . . 43
2.3 Spin Textures in Quasi-Momentum Space . . . . . 44
2.4 Edge States . . . . . 46
2.5 Dynamics of the Edge Currents . . . . . 49
2.6 Summary . . . . . 54

**3 Hall Response and Non-Equilibrium Dynamics 55**
3.1 Hall Response . . . . . 57
3.2 Low-Energy Approximation . . . . . 62
3.3 Generalised Gibbs Ensemble . . . . . 64
3.4 Confinement Potentials . . . . . 67
3.5 Summary . . . . . 71

**4 Role of Disorder 72**
4.1 Topological Characterisation in Coordinate Space . . . . . 73
4.2 Equilibrium Phase Diagram . . . . . 76
4.3 Dynamics of the Local Chern Marker . . . . . 82
4.4 Summary . . . . . 84

**5 Conclusions 86**
5.1 Work in progress . . . . . 87
5.2 Future Directions . . . . . 89

**A Quantum Hall Effect 90**

**B Experimental Realisation of the Haldane Model 94**

**C Edge Currents and Orbital Magnetisation 98**

**Bibliography 103**

# List of Figures

**Preface** **12**

1 Observation of the quantum Hall effect. . . . . 13

**Introduction** **15**

1.1 Spin configuration in the classical XY model, in the presence of vortices. 18

1.2 Examples of topologically equivalent surfaces. . . . . 21

1.3 Schematics for the Aharonov–Bohm effect. . . . . 23

1.4 Honeycomb lattice of the Haldane model. . . . . 25

1.5 Phase diagram of the Haldane model. . . . . 26

1.6 Band structure of the Haldane model. . . . . 27

1.7 "Quantum Newton's cradle" experiment . . . . . 32

**Chern Insulators Out of Equilibrium** **36**

2.1 (a) Quantum quenches in the Haldane model. (b) Excitations at the Dirac points. . . . . 36

2.2 Probability of occupying the upper band for a single Dirac point, following mass quench. . . . . 40

2.3 (a) Symmetries of the time derivative of the Berry connection in the Brillouin Zone. (b) Time derivative of the Berry Curvature. . . . . 44

2.4 Spin textures in quasi-momentum space. . . . . 45
2.5 Energy spectrum of the Haldane model obtained by exact diagonalisation on a finite-size strip. . . . . 46
2.6 Equilibrium properties of the Haldane model on a finite-size strip. . . . . 48
2.7 Dynamics of the edge current $J_N^x(t)$. . . . . 50
2.8 Late-time dynamics of the edge current $J_N^x(t)$ following a quantum quench from the topological to the non-topological phase. . . . . 50
2.9 Further examples of edge current dynamics, following a quantum quench between different points of the phase diagram. . . . . 51
2.10 Edge current $J_N^x(t)$ following multiple quenches to the same final Hamiltonian. . . . . 52
2.11 Light-cone spreading of the currents into the interior of the sample, following a quantum quench. . . . . 52
2.12 Appearance of resurgent oscillations of the edge currents, corresponding to the onset of finite-size effects. . . . . 53

**Hall Response and Non-Equilibrium Dynamics** **55**

3.1 Phase diagram of the Haldane model, showing the quantum quenches analysed in Chapter 3. . . . . 56
3.2 Setup used to evaluate the Hall response in the presence of periodic boundary conditions. . . . . 57
3.3 Hall conductance following a quench from the topological phase. . . . . 60
3.4 Hall conductance following a quench from the non-topological phase. . . 61
3.5 Hall response $\sigma_{xy}(\omega)$ for frequencies below the direct band gap, following a quench from the topological phase to the non-topological phase. . . . . 61
3.6 Post-quench Hall conductance for a single Dirac point. . . . . 63

3.7 Finite-size cylindrical geometry with periodic (open) boundary conditions along the $x$- ($y$-) direction. . . . . 65

3.8 Total edge current following a quantum quench within the topological phase. The time-average of the late-time data agrees with the prediction of the GGE. . . . . 65

3.9 Comparison of the time-averaged total edge current in the Haldane model at late times and the prediction of the GGE . . . . . 66

3.10 Equilibrium properties of the Haldane model in the cylindrical geometry, with an additional harmonic confinement potential. . . . . 68

3.11 Spreading of currents following a quench from the topological phase to the non-topological phase, in the presence of a confining potential. . . . 69

3.12 Dynamics of the currents following a sudden release of the confining potential. . . . . 69

3.13 (a) Illustration of an optical lattice with a rotationally symmetric harmonic trap. (b) Circulating equilibrium currents in the resulting disk geometry. . . . . 70

**Role of Disorder** **72**

4.1 Finite-size diamond shape geometry used to compute the local Chern marker. . . . . 76

4.2 Local Chern marker $\nu(\mathbf{r})$ showing the broadening of the boundary region near the phase transition. . . . . 77

4.3 Phase diagram of the disordered Haldane model, with increasing disorder strength. . . . . 78

4.4 Spatially and disorder averaged Chern marker for a sub-region of the sample, with increasing disorder strength. . . . . 78

4.5 Sharpening of the transition with increasing system size. . . . . 79

4.6 Extrapolation of the transition point to the thermodynamic limit. . . . . 80
4.7 Expansion of the topological regions of the phase diagram with increasing disorder strength. . . . . 80
4.8 Spatially and disorder averaged Chern marker as a function of the disorder strength. . . . . 81
4.9 Spatially and disorder averaged Chern marker as a function of the disorder strength, for different system sizes. . . . . 82
4.10 Time-evolution of the averaged Chern marker. . . . . 83
4.11 Dynamics of the local Chern marker along a cut through the middle of the finite-size sample, for the clean case, $V = 0$. . . . . 84
4.12 Dynamics of the local Chern marker along a cut through the middle of the finite-size sample, in the presence of disorder, $V = t_1$. . . . . 85

**Conclusions** **86**

5.1 Single-particle entanglement spectrum of the Haldane model in the topological phase. . . . . 88

**Quantum Hall Effect** **90**

A.1 Quantum Hall effect setting. . . . . 90
A.2 Potential landscape for the quantum Hall effect. . . . . 92
A.3 Broadening of the Landau levels with disorder. . . . . 93

**Experimental Realisation of the Haldane Model** **94**

B.1 Unit cell of the Haldane model, as realised in the experiment at ETH Zürich. . . . . 95
B.2 Laser beam set-up for the experimental realisation of the Haldane model. 95

B.3 Experimental measurement of the fraction of particles in the upper band following the application of a constant force for the duration of a Bloch oscillation. . . . . 96
B.4 Experimental data for the differential drift. . . . . 97

**Edge Currents and Orbital Magnetisation** **98**

C.1 Strip geometry used for the finite-size computations. . . . . 99
C.2 Momentum space contributions to the equilibrium transverse currents. . 101
C.3 Equilibrium edge current with particle or hole doping. . . . . 102
C.4 Equilibrium orbital magnetisation. . . . . 102

# Preface

A central aspect of condensed matter physics is the study of new phases of matter, the macroscopic behaviour of which is due to the quantum mechanical properties of their constituents, whether they are electrons, spins or ions. The vast majority of phases of matter are distinguished by the presence or absence of some kind of ordering of the particles in the system. Until the 1970s, the emergence of order was understood in terms of symmetry breaking. For instance, a solid is a system in which the lattice arrangement of the atoms is due to the breaking of the continuous translational symmetry. This description of phase transitions has proven to be successful in a wide range of systems, from liquid crystals to ferromagnets. A general theory for phase transitions from the first half of the 20th century, Landau theory [4], finds one of its spectacular flagships in superconductivity [5]. However, some phases of matter cannot be described in terms of symmetry breaking. Indeed, in 1972, Kosterlitz and Thouless discovered a new type of phase transition in two-dimensional systems [6, 7], where topology plays a crucial role, and which cannot be understood in terms of Landau theory. Their predictions were confirmed in experiments on superfluid Helium [8]. Another striking example of a topological phase is provided by the integer quantum Hall effect [9, 10], where topological properties of the ground state lead to the precise quantisation of the Hall conductance in multiples of $q^2/h$, where $q = -e$ is the electric charge, and $h$ is the Planck constant; see Fig. 1. This was observed in 1980 by von Klitzing [10]. Subsequently to early work by Laughlin [12], in 1982, Thouless, Kohmoto, Nightingale, and den Nijs exposed the

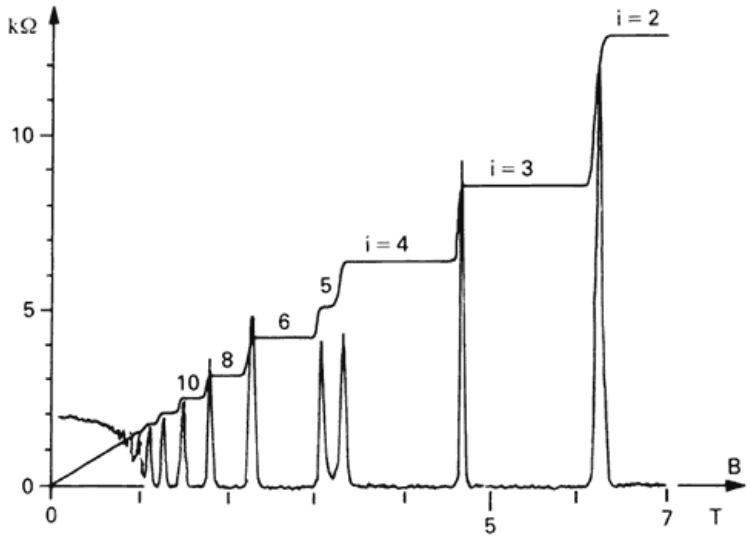


Figure 1: Observation of the quantum Hall effect. Experimental data for the longitudinal $\rho_{xx}$ and Hall $\rho_{xy}$ resistance upon varying the magnetic field $B$ perpendicular to the two-dimensional sample. Each step in the Hall resistance is given by $\frac{1}{\nu}\frac{h}{q^2}$, with integer $\nu$. It follows that the Hall conductance $\sigma_{xy} = \rho_{xy}^{-1}$ is quantised in units of $q^2/h$. Figure adapted from Ref. [11].

intimate relation of the quantised Hall conductance to topological invariants [13], via their famous TKNN formula. In 1982, the even more remarkable fractional quantum Hall effect was discovered [14, 15]. In contrast to the integer quantum Hall effect, where electron-electron interactions are less important than disorder, here interactions play a crucial role. In particular, they lead to the appearance of plateaus of the Hall conductance at precise fractional values of $e^2/h$. One of the important ramifications of this observation is that the quasi-particles in the system carry a fractional charge [15], as observed in experiment [16–18]. In the same period, Haldane discussed the role of topology in discriminating between integer and half-integer spin chains [19, 20], which also received experimental validation [21, 22]. These breakthroughs were followed by a number of Nobel prizes: von Klitzing was awarded the 1985 Nobel prize for his observation of the integer quantum Hall effect; the 1998 Nobel prize was awarded to Laughlin, Störmer and Tsui for their work on the fractional quantum Hall effect; and in 2016 the

Nobel prize was awarded to Thouless, Kosterlitz and Haldane, in recognition of their pioneering theoretical work.

In the light of these discoveries, topological phases of matter were believed to be exceptional in nature, and to occur only in one or two dimensions. However, with the recent discovery of topological insulators and topological superconductors, topological phases have been shown to exist also in three dimensions [23–40]. This has rendered topological phases more prevalent in condensed-matter research.

A fundamental property of many examples of topological matter is the presence of gapless edge states which are robust to local perturbations[1]. This, in combination with the quantisation of macroscopic observables, makes topological systems ideal for technological applications. For example, the exact quantisation of the Hall response is crucial for applications in metrology. The spin-momentum locking in topological insulators makes them suitable candidates for "spintronic" devices [41]. Quantum computing is a further attractive application: the building block of a quantum computer, the "quantum bit", could find its realisation in topological materials [42]. For such applications, it is important that the information imprinted in the "quantum bit" is safely stored, and not lost due to external perturbations. It is therefore crucial to investigate the response of topological phases of matter to strong perturbations and, more in general, their behaviour when driven out of equilibrium.

The work presented in this thesis places itself at the interface of the fields of topological phases of matter and of non-equilibrium physics. We investigate the non-equilibrium dynamics of Chern insulators, i.e. quantum Hall systems on a lattice, focusing on fast processes known as quantum quenches. Ultimately, the insights contained in this thesis may provide some orientation for further research on the non-equilibrium properties of topological insulators and of topological phases of matter in general.

[1]Note, however, that there are examples of topological systems without edge states, e.g. the toric code.

# Chapter 1

# Introduction

In this introduction, we give a broad but brief overview of topological phases of matter. We focus on the quantum Hall effect and its realisation on a lattice, the Chern insulator. We also introduce the Haldane model and its equilibrium phase diagram. This has no presumption to be a comprehensive survey of the vast body of work in this field, but we try to cover the advances that set the context for this thesis. Moreover, we believe this overview to be timely, given the recognition and attention which topological phases of matter have received with the 2016 Nobel Prize in Physics. We also discuss some advances in the field of many-body quantum systems out of equilibrium, focusing on the concepts of a quantum quench and the Generalised Gibbs Ensemble.

## 1.1 Landau Theory

Before Thouless and Kosterlitz's work [6, 7], it was believed that phase transitions occur following the spontaneous breaking of a symmetry (or its restoration). A general theory of phase transitions is provided by Landau theory [4]. In Landau theory, the symmetry breaking is accompanied by the appearance of an order parameter, i.e. a non-vanishing expectation value of some local observable. An example is provided by magnets. To

each position in space $\mathbf{r}$, one can associate a local magnetisation vector $\mathbf{M}(\mathbf{r})$, which, in a non-magnetic material, can point in any direction, resulting in a vanishing averaged value. The material becomes magnetised when the rotational symmetry of this local order parameter is broken, and the system fixes a magnetisation direction for the whole sample. A further example is given by liquid crystals, where again the rotational symmetry is broken, in favour of the alignment of the molecules in the system. As a last example, we mention the BCS theory of superconductivity (named after the Nobel prize winners Bardeen, Cooper and Schrieffer) [43], in which electrons form bound states called *Cooper pairs* and the spontaneously broken symmetry is a U(1) gauge symmetry. In the superconducting phase, the locking of the U(1) phase throughout the whole system is accompanied by the appearance of an energy gap, which is the order parameter of superconductivity.

Topological phase transitions are very different, as they do not manifest any order parameter, nor spontaneous symmetry breaking. Rather, in topological phases, the "ordering" is associated with extensive geometrical properties of the quantum wave function.

## 1.2 Kosterlitz–Thouless Transition

In the context of transitions to ordered phases following spontaneous symmetry breaking, the Mermin–Wagner theorem [44–46] plays an important role. It states that, in one and two dimensions, for systems with short-range interactions, continuous symmetries cannot be spontaneously broken at finite temperature. Intuitively, quantum fluctuations, in low dimensions, suppress the appearance of long-range order. In the 1980s, the study of low-dimensional systems flourished, especially in view of the exotic behaviours enhanced by quantum fluctuations. We here follow Ref. [47] for the discussion of the Kosterlitz–Thouless transition.

Kosterlitz and Thouless were interested in the stability of order in two-dimensional systems and, in particular, in the role of dislocations and topological defects. In their 1973 paper [7], they consider the classical XY model for spins confined to a plane. The Hamiltonian, parameterised by the angle $0 \leq \theta \leq 2\pi$ of the spins with respect to an axis, is

$$H_{\mathrm{XY}} = -J \sum_{\langle i,j \rangle} \cos(\theta_i - \theta_j). \tag{1.1}$$

For $J > 0$, the lowest energy is obtained when all the spins are aligned. When considering this system in three dimensions, one finds that, above a critical temperature $T_c$, the correlation function $\lim_{r\to\infty} \left\langle e^{i(\theta(\mathbf{r})-\theta(0))} \right\rangle$ is exponentially decreasing ($\sim e^{-r/\xi}$). Below this temperature, on the other hand, it approaches a constant, indicating long-range order. Things become more interesting in two dimensions. The continuum limit of the XY model corresponds to the Hamiltonian for a free scalar field

$$H_{\mathrm{XY}} = J/2 \int d^2r \, (\nabla\theta(\mathbf{r}))^2. \tag{1.2}$$

Assuming that $-\infty < \theta < \infty$, one finds that the correlation function decays as a power law [7]. The power law behaviour, which is not incompatible with the Mermin–Wagner theorem, persists even at high temperatures, where an exponential decay is expected. This paradox was resolved by Kosterlitz and Thouless [6, 7]. They realised that the periodicity of $\theta$, which gives rise to vortices, plays a crucial role in the appearance of a finite temperature phase transition. The presence of vortices is accounted for through the vorticity

$$v = \frac{1}{2\pi} \oint_{\Gamma} d\mathbf{r} \cdot \nabla\theta(\mathbf{r}) \quad \in \mathbb{Z} \tag{1.3}$$

which counts the number of times a spin configuration winds whilst varying $\mathbf{r}$ along a closed circuit $\Gamma$; see Fig. 1.1. From Eqs (1.2) and (1.3), it follows that the energy cost

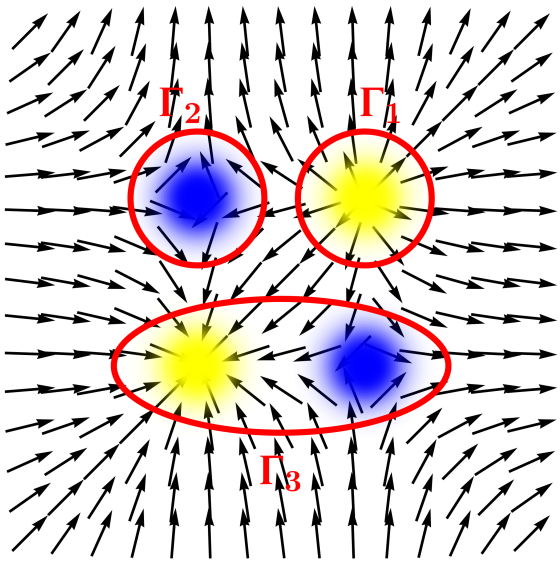


Figure 1.1: Spin configuration in the classical XY model, in the presence of vortices. The vorticity computed along a path enclosing a vortex ($\Gamma_1$) or anti-vortex ($\Gamma_2$) is respectively $v = 1$ and $-1$. For a path enclosing an equal number of vortices and anti-vortices ($\Gamma_3$), the vorticity is vanishing.

for a $v = \pm 1$ vortex is [7]

$$E_v = J/2 \int dr^2 \, (1/r)^2 = J\pi \ln(L/a), \tag{1.4}$$

where $L$ is the size of the system and $a$ is a short distance cut-off, which can be set to the size of the vortex.

For a large system, it is unfavourable to create a single vortex. However, the energy cost for creating a vortex ($v = 1$) anti-vortex ($v = -1$) pair is $2J\pi \ln(d/a)$, with $d$ the distance between the two vortices [7]. The low-temperature phase corresponds to a gas of vortex anti-vortex pairs. To identify the temperature for the transition to a phase of free vortices, Kosterlitz and Thouless turn to a thermodynamic argument. The free

energy for a single vortex is [7]

$$F = E - TS = J\pi \ln(L/a) - Tk_B \ln(L^2/a^2), \tag{1.5}$$

where $k_B$ is Boltzmann's constant, and $L^2/a^2$ is the number of possible positions for a vortex of size $a^2$. It follows that, at temperatures above $T_{KT} = J\pi/2k_B$, it becomes favourable to decouple the pairs into free vortices. Although there is no symmetry breaking, in conformity with the Mermin–Wagner theorem, there is a phase transition [6, 7], as verified experimentally [8, 48]. This is often referred to as the Berezinskii–Kosterlitz–Thouless transition, as Berezinskii had early insights into the role of topological defects [49, 50].

## 1.3 Quantum Hall Effect

The next milestone in the understanding of topological phases of matter is given by the integer quantum Hall effect. The remarkable experimental observation of the quantum Hall effect consists in the quantised Hall conductance

$$\sigma_{xy} = \nu \frac{q^2}{h}, \tag{1.6}$$

of a two-dimensional electron gas subject to a strong perpendicular magnetic field, at low temperature[1]; see Fig. 1. Here, $\nu$ is an integer and $q = -e$ is the charge of the carriers. Simultaneously, the observed dissipation is vanishing, $\sigma_{xx} = 0$. The quantisation of the Hall conductance has an accuracy of $10^{-10}$ and is independent of the microscopic details of the sample. As demonstrated by Laughlin, the precise quantisation of the Hall response is immune to sample defects. In fact, the plateaus in the Hall conductance (Fig. 1) broaden with increasing disorder [12]. The traditional understanding of this

[1] The relativistic quantum Hall effect was recently observed in graphene at room temperature [51].

effect is based on Landau quantisation. Here, we do not go into the details of this argument. However, in the spirit of keeping this thesis self-contained, we discuss the Landau quantisation and the broadening of the plateaus with disorder in Appendix A.

The early theoretical insight [9] and the experimental observation [10] of the quantum Hall effect have revolutionised our understanding of phases of matter, and, together with the discovery of the Kosterlitz–Thouless transition discussed above, have paved the way for the discovery of new topological phases of matter. The quantum Hall effect provides an exquisite example of a macroscopic quantum phenomenon, and is as fundamentally significant as superconductivity.

## 1.4 Topological Invariants

In 1982, Thouless, Kohmoto, Nightingale and den Nijs (TKNN), by means of linear response theory, demonstrated that the exact quantisation of the Hall response is intimately related to a topological invariant, known as the *Chern number* [13].

The term "topology" refers to those geometrical properties that are invariant under smooth deformations, an example being the number of holes of a torus transforming into a mug; see Fig. 1.2. Let us remind the reader of some well known results in this context. Consider a closed surface $M$. Although quantities, like the Gaussian curvature $K$, may be local and dependent on the details of the surface $M$, their integrated value is, on the contrary, a global topological property which does not change under smooth deformations of the surface. Formally,

$$\frac{1}{2\pi}\int_M K dA = \chi(M) \tag{1.7}$$

where $\chi(M)$ is the Euler characteristic of the surface $M$. For orientable compact closed surfaces, this has a clear interpretation. In this case $\chi(M) = 2(1-g)$, where $g$ is the genus of the surface, i.e. its number of holes; see Fig. 1.2. This result is known as the


Figure 1.2: Topology is the study of the geometrical properties of surfaces which are preserved under smooth deformations, i.e. twisting or stretching, but not piercing or gluing. (a) In this picture, a torus can be smoothly deformed into a mug without tearing the surface. They are topologically equivalent with the same genus $g = 1$. (b) The same applies for the double-torus and a two handled cup; both have genus $g = 2$. In this simple example, the number of holes determines the topological character of the surface.

Gauss–Bonnet theorem.

### Chern Number

A generalisation of the Gauss–Bonnet theorem by Chern [52] is instrumental to understand how topology is relevant for physics. The general idea is to monitor how the wave function of a system changes with respect to a parameter $\mathbf{X}$. The Gauss–Bonnet theorem is generalised by considering $\mathbf{X} \in M_2$, where $M_2$ is a closed orientable 2-manifold. For a system invariant under a local gauge transformation $|\psi'(\mathbf{X})\rangle = e^{-i\lambda(\mathbf{X})}\,|\psi(\mathbf{X})\rangle$, one may define a covariant derivative

$$|D_\mu\psi(\mathbf{X})\rangle = |\partial_\mu\psi(\mathbf{X})\rangle - |\psi(\mathbf{X})\rangle\,\langle\psi(\mathbf{X})\,|\,\partial_\mu\psi(\mathbf{X})\rangle\,, \tag{1.8}$$

where $|\psi(\mathbf{X})\rangle\,\langle\psi(\mathbf{X})|$ projects out the parts of $|\partial_\mu\psi(\mathbf{X})\rangle$ that are not orthogonal to $|\psi(\mathbf{X})\rangle$. Introducing the *Berry connection* $A_\mu(\mathbf{X}) = i\,\langle\psi(\mathbf{X})\,|\,\partial_\mu\psi(\mathbf{X})\rangle$, Eq. (1.8) takes the form $|D_\mu\psi(\mathbf{X})\rangle = |\partial_\mu\psi(\mathbf{X})\rangle + iA_\mu(\mathbf{X})\,|\psi(\mathbf{X})\rangle$, which is reminiscent of the gauge

covariant derivative in electromagnetism. A variation in parameter space along a closed path $\Gamma$ contributes to the wave function a phase factor

$$e^{i\phi} = e^{i \oint_\Gamma dX^\mu A_\mu(\mathbf{X})}, \tag{1.9}$$

known as the *Berry phase* [53]. In order to preserve the single-valuedness of the wave function, $\phi = 2\pi\nu$, with integer $\nu$. Equivalently, using Stokes' theorem, we can write

$$\nu = \frac{1}{2\pi} \int_{M_2} dX^\mu \wedge dX^\sigma \, \Omega_{\mu\sigma}(\mathbf{X}) \in \mathbb{Z}, \tag{1.10}$$

where $\Omega_{\mu\sigma} = \langle D_\mu \psi(\mathbf{X}) \,|\, D_\sigma \psi(\mathbf{X}) \rangle - \langle D_\sigma \psi(\mathbf{X}) \,|\, D_\mu \psi(\mathbf{X}) \rangle$ is the *Berry curvature*, and the resemblance with Eq. (1.7) is manifest.

**Aharonov–Bohm Effect**

The parallel with electromagnetism is not only formal. In fact, in this case, the Berry connection corresponds to the usual vector potential, and the parameter space $\mathbf{X}$ is real space. Let us consider a situation in which a magnetic flux $\Phi_B$ exists only in a limited region in space, for example in the presence of an infinite conducting coil. Interestingly, the vector potential is allowed to be non-vanishing even in region of space where there is no magnetic field. Let us now imagine to split an electron wave along two paths ($\Gamma_1$ and $\Gamma_2$), as shown in Fig. 1.3(a). The two partial waves will interfere at $B$, with a phase difference

$$\Delta\phi = \frac{q}{\hbar} \left[ \int_{\Gamma_1} \mathbf{A}(\mathbf{x}') \cdot d\mathbf{x}' - \int_{\Gamma_2} \mathbf{A}(\mathbf{x}') \cdot d\mathbf{x}' \right] = \frac{q}{\hbar} \oint_{\Gamma_1 + \Gamma_2} \mathbf{A}(\mathbf{x}') \cdot d\mathbf{x}', \tag{1.11}$$

where $q = -e$ is the electron charge, and $\mathbf{A}(\mathbf{x})$ is the electromagnetic vector potential. The integral on the right-hand side is the magnetic flux in the region between the two paths, and thus we obtain $\Delta\phi = \frac{q}{\hbar}\Phi_B$. This phenomenon is known as the Aharonov–

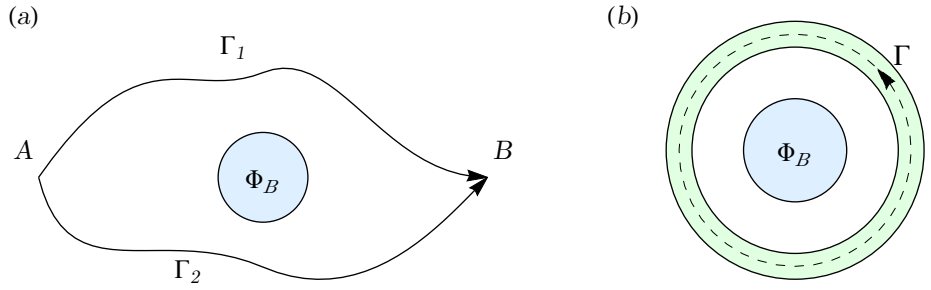


Figure 1.3: (a) Schematic illustration of the Aharonov–Bohm effect. Two partial electron waves move from point $A$ to $B$, along different paths $\Gamma_1$ and $\Gamma_2$. If a non-vanishing magnetic flux $\Phi_B$ exists in the region between the two paths, the two partial waves will display an interference pattern. (b) If the electrons flow in a superconducting circuit (green ring), the magnetic flux is quantised: $\Phi_B = \frac{h}{2e}\nu$, with integer $\nu$.

Bohm effect [54, 55]. The phase in Eq. (1.11) corresponds to the Berry phase introduced above, and does not need to be quantised. Let us instead consider the more relevant case in which the electrons move in a superconducting wire with cross section larger than the London penetration depth; see Fig. 1.3(b). In this case, the wave function must be coherent, and the phase difference for the Cooper pairs in the superconducting circuit (with charge $q = -2e$) must be vanishing. One finally finds that the magnetic flux must be quantised as $\frac{2e}{\hbar}\Phi_B = 2\pi\nu$, with $\nu \in \mathbb{Z}$. Finally, writing explicitly the magnetic flux as the integral of the magnetic field, $\Phi_B = \int d\mathbf{x}\, \mathbf{B}(\mathbf{x})$, we recognise in $\nu$ the Chern number, and in the magnetic field the analogue of a component of the Berry curvature.

### Chern Number in Periodic Potentials

After having gone through the exercise of computing the Aharonov–Bohm phase shift, we are now equipped to understand how topology affects electrons in a two-dimensional lattice. The mathematics is the same as above, however here the parameter space $\mathbf{X}$ is the quasi-momentum space, with periodic boundary conditions. For lattice models, this corresponds to the Brillouin zone. Let us then consider a Hamiltonian varying in quasi-momentum space, $\hat{H}(\mathbf{k})$, and a state $|\psi(\mathbf{k})\rangle$. As the state moves along a closed

path in quasi-momentum space, it picks up a Berry phase [53]

$$\phi = \oint_{\partial \mathrm{BZ}} d\mathbf{k} \cdot \mathbf{A}_{\mathbf{k}}, \tag{1.12}$$

where $\mathbf{A}_{\mathbf{k}} = \langle \psi(\mathbf{k}) \,|\, i\nabla \,|\, \psi(\mathbf{k}) \rangle$ is the Berry connection. In order to preserve the single-valuedness of the wave function, then one must impose $\phi = 2\pi\nu$. Here, $\nu$ is the Chern number given by Eq. (1.10). Note, however, that in order to obtain a non-vanishing Chern number, the Berry connection must have some singularities somewhere in the Brillouin zone. Indeed, the line integral of $\mathbf{A}_{\mathbf{k}}$ around the Brillouin zone boundaries must vanish if $\mathbf{A}_{\mathbf{k}}$ is a smooth function in the vicinity of that contour, since contributions from opposite edges of the Brillouin zone exactly cancel. These singularities can be avoided by using different gauge patches in different parts of the Brillouin zone; see for example Ref. [56]. More easily, the Chern number can be computed by integrating the curl of $\mathbf{A}_{\mathbf{k}}$, i.e. the gauge invariant Berry curvature $\Omega$, over the Brillouin zone. Explicitly,

$$\nu = \frac{1}{2\pi} \int_{\mathrm{BZ}} d\mathbf{k}\, \Omega \quad \in \mathbb{Z} \tag{1.13}$$

where $\Omega = \partial_{k_x} A_{k_y} - \partial_{k_y} A_{k_x}$ is the Berry curvature.

We can now appreciate the incredible breakthrough of TKNN [13]. They were able to demonstrate that the macroscopically observable Hall conductance is proportional to the rather abstract topological Chern number. Explicitly,

$$\sigma_{xy} = \frac{e^2}{2\pi h} \int_{\mathrm{BZ}} d\mathbf{k}\, \Omega. \tag{1.14}$$

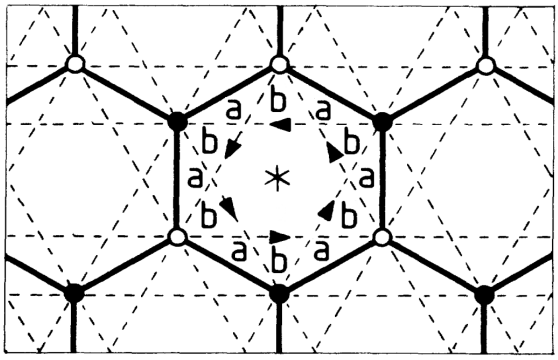


Figure 1.4: Honeycomb lattice of the Haldane model. The solid (dashed) lines correspond to the nearest (next-to-nearest) neighbour hopping. Open and solid dots are the two sub-lattices $A$ and $B$, respectively. $a$ and $b$ label regions with opposite magnetic flux. The arrows point in the direction of positive phase $\varphi$ in the next-to-nearest neighbour hopping. Figure adapted from Ref. [57].

## 1.5 Haldane Model

An important feature of Eq. (1.14) is that it is independent of any applied magnetic field. In 1988, Haldane showed that the integer quantum Hall effect does *not* require a *net* magnetic field, and in fact belongs to a wider class of phenomena associated with broken time-reversal symmetry [57]. He proposed a two-dimensional model which exhibits a quantised Hall conductance, in the absence of a net magnetic field[2] [57]. A key feature of the Haldane model is that it does not need disorder, nor interactions, to exhibit a topological phase. It is therefore ideal to address very general and broad questions about the non-equilibrium dynamics of Chern insulators.

The Haldane model describes spinless fermions hopping on a honeycomb lattice with both nearest and next-to-nearest neighbour hopping parameters; see Fig. 1.4. The

[2]In fact, this is also a property of the Hofstadter model [58], where each plaquette is pierced by a rational multiple $P/Q$ of the flux quantum. If one considers a super-cell of $Q$ plaquettes, this will be pierced by $P \in \mathbb{N}$ flux quanta. However, the magnetic flux on a lattice is only defined modulo the flux quantum. This situation is therefore equivalent to a super-cell threaded by zero flux. We thank Prof. S. Simon for bringing this aspect of the Hofstadter model to our attention.

Hamiltonian is [57]

$$\hat{H} = -t_1 \sum_{\langle i,j \rangle} \left( \hat{c}_i^\dagger \hat{c}_j + \text{h.c.} \right) - t_2 \sum_{\langle\langle i,j \rangle\rangle} \left( e^{i\varphi_{ij}} \hat{c}_i^\dagger \hat{c}_j + \text{h.c.} \right) + M \sum_{i \in A} \hat{n}_i - M \sum_{i \in B} \hat{n}_i, \quad (1.15)$$

where the fermionic operators obey the anti-commutation relations $\{\hat{c}_j, \hat{c}_j^\dagger\} = \delta_{ij}$ and $\hat{n}_i \equiv \hat{c}_i^\dagger \hat{c}_i$. Here, $\langle i,j \rangle$ and $\langle\langle i,j \rangle\rangle$ indicate the summation over the nearest and next-to-nearest neighbour sites respectively, and $A$ and $B$ label the two sub-lattices. The phase factor $\varphi_{ij} = \pm\varphi$ corresponds to the Aharonov–Bohm phase due to a staggered magnetic field with the full symmetry of the lattice, such that the local flux within a hexagonal plaquette is non-zero, but the total flux through a plaquette vanishes, and it is taken positive (negative) for anticlockwise (clockwise) next-to-nearest neighbour hopping; see Fig. 1.4. The associated time-reversal symmetry breaking leads to a quantum Hall effect in the absence of a net magnetic field. The energy off-set $\pm M$ breaks spatial inversion symmetry. Although this parameter is not necessary for the quantum Hall effect, it allows us to also explore the non-topological semi-conducting phase. The phase diagram of the Haldane model is shown in Fig. 1.5. Following Ref. [57], we assume that $|t_2/t_1| \leq 1/3$ so that the bands may touch, but not overlap; see Fig. 1.6.

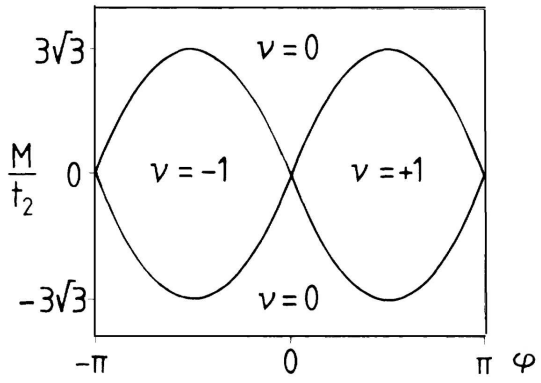


Figure 1.5: Phase diagram of the Haldane model obtained from the low-energy Dirac fermion representation, showing topological ($\nu = \pm 1$) and non-topological phases ($\nu = 0$). Figure adapted from Ref. [57].

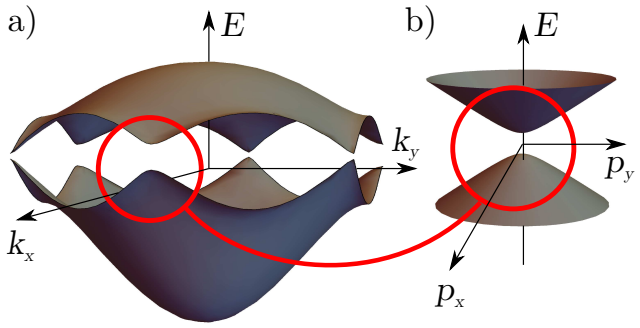


Figure 1.6: (a) Band structure of the Haldane model [57]. (b) At low-energies, the model reduces to a sum of two Dirac Hamiltonians with a gapped relativistic dispersion relation.

### Dirac Hamiltonian

In Fourier space, the Hamiltonian (1.15) is given by [57]

$$\hat{H}(\mathbf{k}) = -2t_2 \cos\varphi \left( \sum_i \cos(\mathbf{k}\cdot\mathbf{b}_i) \right) \mathrm{I} - t_1 \left( \sum_i [\cos(\mathbf{k}\cdot\mathbf{a}_i)\sigma^1 + \sin(\mathbf{k}\cdot\mathbf{a}_i)\sigma^2] \right) + \left[ M - 2t_2 \sin\varphi \left( \sum_i \sin(\mathbf{k}\cdot\mathbf{b}_i) \right) \right] \sigma^3, \quad (1.16)$$

where $\sigma^\mu$ are Pauli matrices and I is the identity matrix. Here, $\mathbf{a}_1, \mathbf{a}_2, \mathbf{a}_3$ are the displacements from a $B$ site to its three nearest-neighbour $A$ sites. The $\mathbf{b}_i$'s are defined via cyclic permutations of $\mathbf{b}_1 = \mathbf{a}_2 - \mathbf{a}_3$ and correspond to the second-neighbour displacements, $\pm\mathbf{b}_i$. For $t_2, M \ll t_1$, the Hamiltonian (1.16) has a linear dispersion near the six corners of the hexagonal Brillouin zone, but only two of these are inequivalent. We denote these by $\mathbf{k}_\alpha$, with $\alpha = \pm 1$ labelling the two Dirac points. Expanding the Hamiltonian around these two corners, with $\mathbf{\Pi}_\alpha = (\Pi^x_\alpha, \Pi^y_\alpha) = \mathbf{k} - \mathbf{k}_\alpha$, one obtains [57]

$$\hat{H}_\alpha = c(\Pi^1_\alpha \sigma^2 - \Pi^2_\alpha \sigma^1) + m_\alpha c^2 \sigma^3, \quad (1.17)$$

where $m_\alpha = (M - 3\sqrt{3}\alpha t_2 \sin\varphi)/c^2$ is the effective mass, $c = 3t_1 a/2\hbar$ is the effective speed of light, $a$ is the lattice spacing, and

$$(\Pi^1_\alpha + i\Pi^2_\alpha) = \frac{2}{3}\sum_i e^{i\mathbf{k}_\alpha\cdot\mathbf{a}_i}\frac{\mathbf{a}_i\cdot\mathbf{\Pi}_\alpha}{|\mathbf{a}_i|}. \tag{1.18}$$

In order to simplify the notations we parameterise the complex number $\Pi^2_\alpha + i\Pi^1_\alpha$ as $p\,e^{i\alpha\theta}$. As a result, close to half-filling, the low-energy description is given by the sum of two Dirac Hamiltonians

$$\hat{H}_\alpha(p,\theta) = \begin{pmatrix} m_\alpha c^2 & -c\,p\,e^{i\alpha\theta} \\ -c\,p\,e^{-i\alpha\theta} & -m_\alpha c^2 \end{pmatrix}. \tag{1.19}$$

The Chern number $\nu$, discussed previously, is integer and non-vanishing in the topological phases, and is zero in the semiconducting phase [13, 52, 53, 57]. For the ground state of the Haldane model, $\nu \in \pm 1, 0$. This may be decomposed into contributions from the two Dirac points as $\nu = \nu_+ + \nu_-$, where

$$\nu_\alpha = -\tfrac{\alpha}{2}\,\mathrm{sign}(m_\alpha) \in \pm 1/2. \tag{1.20}$$

The boundaries of the topological phases correspond to the locations where $m_\pm$ changes sign. They are thus given by $M/t_2 = \pm 3\sqrt{3}\sin\varphi$, and are independent of $t_1$; see Fig. 1.5.

### Experimental Realisation

In this thesis, we present results based on the Haldane model. This choice is particularly timely, given that it was realised experimentally in 2013 [59]. The realisation of this model went beyond Haldane's expectations. Indeed, in his 1988 paper, he concludes [57]:

> *While the particular model presented here is unlikely to be directly physically realisable, it indicates that [...] the QHE can be placed in the wider context*

*of phenomena associated with broken time-reversal invariance, and does not necessarily require external magnetic fields.*

The element of the model which made its realisation "unlikely" was the staggered magnetic field used to break time-reversal symmetry. However, this technical challenge was overcome thanks to recent advances in ultracold atoms [60–64]. In particular, the realisation of the symmetry-breaking phase factor $e^{\pm i\varphi}$ was made possible through modulation of the optical lattice [65, 66], *without* any staggered magnetic field. A more detailed description of this experiment is provided in Appendix B.

## 1.6 Topological Insulators

The importance of the Haldane model goes beyond the possibility to obtain an integer quantum Hall effect in the absence of a net magnetic field. Indeed, the Haldane model proved instrumental for the discovery of the broader class of time-reversal *symmetric* topological insulators. In 2005, motivated by work on graphene [67–70], Kane and Mele proposed a slightly more realistic model respecting the symmetries of graphene, including time-reversal invariance [23, 24]. Taking into account the spin of the electrons, and adding a spin-orbit potential, they obtained a new time-reversal invariant "topological insulator" phase, distinct from an ordinary insulator. The Kane–Mele model, in its simplest formulation, consists of two copies of the Haldane model, for the opposite spins. Each of the two copies breaks time-reversal symmetry leading to a quantised Hall conductance. Each copy has an opposite Chern number $\nu^{\uparrow} = -\nu^{\downarrow}$, and hence Hall currents flowing in opposite directions $\mathbf{J}^{\uparrow} = -\mathbf{J}^{\downarrow}$. The two copies together, however, do not break time-reversal symmetry. Although the opposite currents annihilate charge transport, one can observe a non-vanishing spin current $\mathbf{J}_s = \frac{\hbar}{2e}(\mathbf{J}^{\uparrow} - \mathbf{J}^{\downarrow})$, with a quantised spin Hall conductance of $e/2\pi$.

Together with work by Zhang and collaborators [25, 26], this model opened a new

area of research on topological insulators. Subsequently, topological insulators were further theorised and experimentally observed both in two and three dimensions [27–29, 34, 35, 37–40, 71, 72].

## 1.7 Non-Equilibrium Systems

In this thesis, we focus on the non-equilibrium dynamics of Chern insulators. So far, we have introduced the topological concepts required for this work. Here, we introduce some key notions to contextualise the non-equilibrium elements of this thesis.

Much of physics is focused on the equilibrium behaviour of classical and quantum systems. However, as faster and smaller devices become increasingly ubiquitous in modern technologies, the analysis of their response to perturbations becomes more and more important. In particular, having a clear view over the non-equilibrium behaviour of topological systems could potentially benefit fields of research oriented towards the exploitation of these phases of matter for spintronic devices and in quantum computation. For advances in this direction, see Refs [73–83]. Moreover, the interest for understanding non-equilibrium processes goes beyond its technological applications, as it interrogates the foundations of statistical mechanics. For example, classical equilibrium statistical mechanics rests on the ergodic hypothesis, according to which a system uniformly samples the phase space in time. However, little is known about the dynamics which leads to thermal equilibrium, and only in the last decade there has been a real and growing interest towards these kinds of fundamental questions [84–88]. Recent experimental advances in ultracold atoms have motivated and further bolstered the interest of the scientific community in non-equilibrium processes [89].

### Quantum Quenches

In the context of many-body systems, a typical protocol used to drive systems out of equilibrium is the *quantum quench* [83, 87, 90–103], which will be ubiquitous in this thesis. Consider a Hamiltonian $\hat{H}(g)$ which is dependent on some parameter $g$. A quantum quench consists in preparing the system in the ground state of $\hat{H}(g)$, $|\psi_g\rangle$, and, at time $t = 0$, suddenly changing $g$ to $g'$. Upon quenching the parameter $g$, the state evolves unitarily under the new Hamiltonian:

$$|\psi(t)\rangle = e^{-\frac{i}{\hbar}\hat{H}(g')t}\,|\psi_g\rangle\,, \tag{1.21}$$

and the corresponding density matrix is $\hat{\rho}(t) = |\psi(t)\rangle\langle\psi(t)|$.

A natural question which arises is whether the quenched system eventually thermalises. Thermalisation means that the expectation value of an observable $\hat{O}$, $\langle\hat{O}\rangle = \mathrm{Tr}[\hat{\rho}(t)\hat{O}]$, eventually becomes indistinguishable from the expectation value for a thermal ensemble $\mathrm{Tr}[\exp(-\beta\hat{H}(g'))\hat{O}]$, where $\beta$ is an inverse temperature. If a system thermalises, it is well described by a few macroscopic quantities only, such as the temperature and the number of particles in the system. The success of thermodynamics is mostly due to the fact that interacting systems eventually reach thermal equilibrium. However, although several thermalisation mechanisms are known [84–88], a rigorous proof for the thermalisation of quenched interacting many-body systems is still missing [104].

### Generalised Gibbs Ensemble

In spite of the success of statistical mechanics, not all systems thermalise. The first experiment showing the absence of thermalisation in a many-body system is given by the "quantum Newton's cradle" [89]. In this experiment, an array of distinct parallel one-dimensional Bose-Einstein condensates are prepared in a harmonic trap. The atoms of the Bose gas are later split into a superposition of states with opposite peaks in their

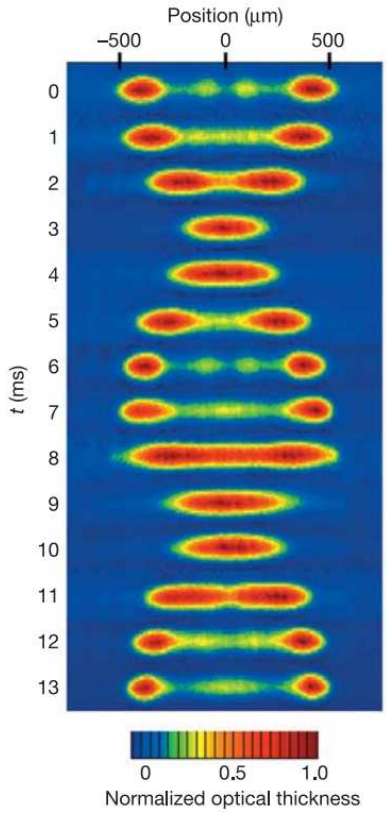


Figure 1.7: Quantum Newton's cradle experiment. An array of one-dimensional Bose-Einstein condensates are prepared in a harmonic trap. The atoms of the Bose gas are split into a superposition of states with opposite peaks in their momentum distribution, and are allowed to oscillate and collide with each other. After a variable waiting time $t$, a time of flight measurement is performed, resulting in the figure. The system does not equilibrate, even after thousands of collisions. Figure adapted from Ref. [89].

momentum distribution, and are allowed to oscillate and collide with each other; see Fig. 1.7. In spite of the collisions, the system does not equilibrate over the duration of the experiment.

Motivated by this experiment, research on the equilibration properties of integrable systems intensified. Integrable systems, typically systems with a large number of conserved quantities, fail to thermalise, due to the constraints imposed by the constants of the motion. Nevertheless, their long time behaviour is captured by a Generalised Gibbs

Ensemble (GGE) [87, 94, 96, 103, 105]

$$\hat{\rho}_{\mathrm{GGE}} = Z^{-1} \exp\left( - \sum_{\gamma} \lambda_{\gamma} \hat{I}_{\gamma} \right), \tag{1.22}$$

where $Z = \mathrm{Tr} \exp\left( - \sum_{\gamma} \lambda_{\gamma} \hat{I}_{\gamma} \right)$, $\hat{I}_{\gamma}$ is the set of conserved quantities in the system, and $\lambda_{\gamma}$ is the corresponding set of generalised inverse temperatures. The Generalised Gibbs Ensemble is relevant for the work presented in Chapter 3.

### Alternative protocols

Global quantum quenches are not the only protocols used to drive systems out of equilibrium. A popular alternative choice are sweeps or ramps [100, 106–110]. In this case, the change of the parameter $g \to g'$ is not instantaneous but happens in a finite time interval. Another example is given by local, rather than global, quantum quenches [111–113]. The experimental side of this field is also thriving, especially thanks to the high degree of control available in cold atom experiments [89, 102, 114, 115].

A further research field in non-equilibrium physics is provided by the study of driven systems, where the non-equilibrium aspects are inherently embedded in the system. In this class, we mention photonic systems, which can be used, alternatively to cold atom experiments, as quantum simulators [116–124]. Another example is provided by Floquet systems [66, 125–138], where time-dependent Hamiltonians with periodic driving are considered. It is worth noting that the experimental realisation of the Haldane model via periodic modulation of the lattice [59] is theoretically described in terms of the Floquet theory. In this thesis, however, we take a step back from the details of the specific periodic driving scheme, and instead we focus on the pure non-equilibrium dynamics of the Haldane model. In this way, we avoid conflating the driven dynamics of Floquet systems with the intrinsic non-equilibrium dynamics of Chern insulators, which we want to investigate.

## 1.8 Thesis Layout

In Chapter 2, we explore the non-equilibrium response of Chern insulators. We consider quantum quenches between topological and non-topological phases in the Haldane model, and study the associated non-equilibrium dynamics. A striking result is that the Chern number, calculated for an infinite system, is preserved following such a quench. In spite of this preservation, physical observables such as the edge currents and the magnetisation undergo non-trivial dynamics in finite-size systems. This is due to the formation or disappearance of the edge modes, and their re-population. In particular we show that, following a quantum quench, the edge currents reach new steady-state values. We also provide evidence for the light-cone propagation of the currents into the interior of the sample. The results presented in this Chapter are published in Ref. [1].

In Chapter 3, we analyse the unitary evolution of the Hall response following a quantum quench, providing explicit results, both numerical and analytical, for the Haldane model. Out of equilibrium, the Hall response is no longer quantised. We then further explore the non-equilibrium dynamics of the edge currents, showing that, at late times, these can be described in terms of a Generalised Gibbs Ensemble. To make connections with experiments in cold atom settings, we also consider the effects of an external trapping potential. The results presented in this Chapter are published in Ref. [2].

In Chapter 4, we discuss the role of disorder on the non-equilibrium dynamics of finite-size Chern insulators. We provide an overview of the equilibrium phase diagram of the Haldane model in the presence of on-site potential disorder, characterising the topological phases by means of the local Chern marker introduced by Bianco and Resta [139]. We then explore the time-evolution of the local Chern marker, and its average over many lattice sites and disorder realisations, following quantum quenches between the topological and non-topological phases. We observe light-cone propagation of "Chern currents" from the boundaries towards the interior of the sample, reminiscent of the evolution of

the edge currents discussed in Chapter 2. The results presented in this Chapter are currently in preparation for publication [3].

Finally, in Chapter 5, we present the Conclusions of this thesis and discuss some ongoing work on the non-equilibrium dynamics of the entanglement entropy and entanglement spectrum of the Haldane model. We conclude the thesis by discussing potential future research directions.

# Chapter 2

# Chern Insulators Out of Equilibrium

In this Chapter[1], we explore the non-equilibrium response of Chern insulators, focusing on the paradigmatic Haldane model. We study the dynamics induced by quantum quenches and sweeps between the topological and non-topological phases; see Fig. 2.1.

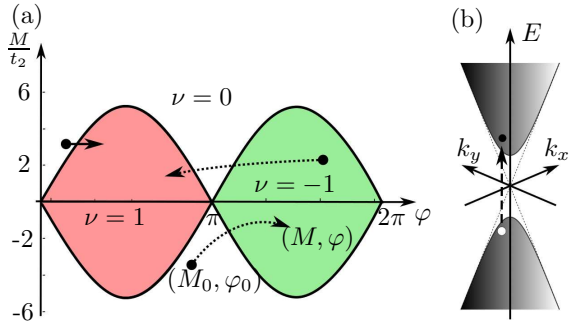


Figure 2.1: (a) Phase diagram of the Haldane model obtained from the low-energy Dirac fermion representation, showing topological ($\nu = \pm 1$) and non-topological ($\nu = 0$) phases [57]. We study quantum quenches and sweeps between different regions of the phase diagram, as illustrated by the arrows. (b) The low-energy spectrum of the Haldane model is described by excitations around the two Dirac points. After a quench, carriers in the lower band are excited to the upper band.

Out of equilibrium, on physical grounds, one expects the Hall response to depart from its quantised value. A natural starting point is therefore to explore the evolution

[1]The results presented in this Chapter are published in Ref. [1].

of the Chern number. A striking result is that the Chern number, in an infinite system, is unchanged under the dynamics following such a quench. The topological Chern index, by definition robust to local perturbations, is robust even against strong, global, quenches. We return to the calculation of the Hall response in Chapter 3.

Another defining characteristic of Chern insulators is the appearance of edge states in the energy spectrum for finite-size samples. In order to probe the edge physics in finite-size geometries, we analyse the dynamics of physical observables which are sensitive to the presence or absence of the edge states, such as the edge currents and the orbital magnetisation. In spite of the preservation of the Chern number in the absence of sample boundaries, these observables undergo non-trivial dynamics. We show that, following a quantum quench, the edge currents relax towards new steady-state values, and that there is light-cone spreading of the currents into the interior of the finite-size sample.

### Quantum Quenches

In order to gain insight into the non-equilibrium dynamics of the Haldane model, we make use of the quantum quench protocol introduced in Section 1.7. Throughout this thesis, we consider quantum quenches between different points $(M, \varphi)$ on the phase diagram shown in Fig. 2.1(a), for fixed values of $t_1$ and $t_2$. At time $t = 0$, the system is prepared in the ground state of the Haldane model with parameters $(M_0, \varphi_0)$. At half-filling, the initial state fills the lower band of Fig. 1.6. We then abruptly change the parameters of $\hat{H}$ to $(M, \varphi)$, and let the system evolve unitarily under the action of this new Hamiltonian. In general, this will lead to a non-trivial occupation of both the lower and the upper bands; see Fig. 2.1.

We first demonstrate the preservation of the Chern number following a quantum quench by focusing on the contributions from the two Dirac points. This analysis captures the physics of this non-equilibrium process, in spite of the fact that high-energy states, far from the Dirac points, can be populated. In this low-energy framework, we

also show that the Chern number is preserved under linear sweeps. We then show that the Chern number is preserved for the Haldane model, beyond the low-energy description. Finally, we give a general intuitive argument for this preservation, based on spin textures in quasi-momentum space. Similar results were also obtained by D'Alessio and Rigol [132].

## 2.1 Contributions from the Dirac Points

We begin by examining the non-equilibrium response of the effective Dirac Hamiltonian $\hat{H} = \hat{H}_+ + \hat{H}_-$, with $\hat{H}_\alpha$ given by Eq. (1.19). From Eq. (1.20), we recall that $\nu = -\frac{1}{2}\left[\mathrm{sign}(m_+) - \mathrm{sign}(m_-)\right]$. Quenching between different phases corresponds to changing the sign of one or both of the masses $m_\alpha$. For a given Dirac point, such changes will lead to a re-distribution of carriers between the two bands, which may be measured through band-mapping techniques [59]; see Fig. 2.1. We denote the energies in the lower and upper bands by $E_\alpha^{l,u}(p)$, and the corresponding eigenstates by $|l_\alpha(p,\theta)\rangle$ and $|u_\alpha(p,\theta)\rangle$. We recall that the quasi-momenta near the Dirac point $\alpha$ are parameterised by $p\,e^{i\alpha\theta}$. From Eq. (1.19), it is straightforward to check that the eigenvalues of $H_\alpha(p,\theta)$, $E_\alpha^{l,u}(p)$, are independent of $\theta$. For a generic state in a $\theta$-independent superposition of the upper and lower states,

$$|\psi_\alpha(p,\theta)\rangle = a_\alpha(p)e^{-iE_\alpha^l(p)t}\,|l_\alpha(p,\theta)\rangle + b_\alpha(p)e^{-iE_\alpha^u(p)t}\,|u_\alpha(p,\theta)\rangle\,, \tag{2.1}$$

the Chern number is formally given by

$$\nu_\alpha(t) = -\alpha\,\mathrm{sign}\,m_\alpha\left(\frac{1}{2} - |b_\alpha(0)|^2\right) - |b_\alpha(\infty)||a_\alpha(\infty)|\cos[(E_\alpha^u(\infty) - E_\alpha^l(\infty))t + \delta], \tag{2.2}$$

where, for the low-energy field theory, the domain of integration in Eq. (1.13) is extended to the whole two-dimensional quasi-momentum space. Here, $a_\alpha(p)$ and $b_\alpha(p)$ are complex

$c$-numbers, and $\delta = \arg(a_\alpha(\infty)) - \arg(b_\alpha(\infty))$. In general, $\nu_\alpha(t)$ is time-dependent, and differs from its ground-state values of $\pm 1/2$. However, the time-dependence only enters via the superposition coefficients evaluated at $k = \infty$.

**Proof of Equation (2.2)**

In order to prove Eq. (2.2), we focus here on the $\alpha = -1$ Dirac point. The case $\alpha = +1$ can be treated analogously. For the Dirac Hamiltonian, given by Eq. (1.19) with $\alpha = -1$, the Berry connection is given by $A_p^- = i \langle \psi_- | \partial_p \psi_- \rangle$ and $A_\theta^- = i \langle \psi_- | \partial_\theta \psi_- \rangle$. For the state in Eq. (2.1), with

$$|l_-(p,\theta)\rangle = \begin{pmatrix} e^{-i\theta} f_-(p, m_-) \\ f_+(p, m_-) \end{pmatrix}, \quad |u_-(p,\theta)\rangle = \begin{pmatrix} -e^{-i\theta} f_+(p, m_-) \\ f_-(p, m_-) \end{pmatrix}, \tag{2.3}$$

and[2]

$$f_\pm(p,m) = \sqrt{\frac{1}{2}\left(1 \pm \frac{m_-}{\sqrt{p^2 + m_-^2}}\right)}, \tag{2.4}$$

the coefficients $A_p^-$ and $A_\theta^-$ are independent of $\theta$. As a result, the contribution of this Dirac point to the Chern number, $\nu = \nu_+ + \nu_-$, is

$$\nu_- = \frac{1}{2\pi} \int_0^{2\pi} d\theta \int_0^\infty dp\, \Omega^- = \int_0^\infty dp\, \partial_p A_\theta^- = A_\theta^- |_0^\infty , \tag{2.5}$$

where $\Omega^- = \partial_p A_\theta^- - \partial_\theta A_p^-$. Using the explicit forms in Eq. (2.3), one obtains

$$A_\theta^- = |\tilde{a}_-(p,t)|^2 f_-^2(p, m_-) + |\tilde{b}_-(p,t)|^2 f_+^2(p, m_-) - \frac{p}{2\sqrt{p^2 + m_-^2}} \left( \tilde{a}_-^*(p,t) \tilde{b}_-(p,t) + \text{h.c.} \right), \tag{2.6}$$

[2]The index $\pm$ of $f_\pm(p,m)$ should not be confused with the Dirac point index $\alpha = \pm$.

where $\tilde{a}_-(p,t) = a_-(p)e^{-iE^l_-(p)t}$ and $\tilde{b}_-(p,t) = b_-(p)e^{-iE^u_-(p)t}$. It follows that

$$A^-_\theta(\infty) = \frac{1}{2}\left[1 - \left(\tilde{a}^*_-(\infty,t)\tilde{b}_-(\infty,t) + \text{h.c.}\right)\right] \tag{2.7}$$

$$A^-_\theta(0) = \begin{cases} |\tilde{b}_-(0,t)|^2 & m_- > 0 \\ |\tilde{a}_-(0,t)|^2 & m_- < 0. \end{cases} \tag{2.8}$$

Eq. (2.2) follows by substituting Eqs (2.7) and (2.8) into Eq. (2.5).

### Quantum Quenches at the Dirac Points

Equation (2.2) shows the contributions from a single Dirac point $\alpha$ to the Chern number, for the state defined in Eq. (2.1). Here, we explicitly show that $b_\alpha(\infty) = 0$, following a quantum quench; see Fig. 2.2. In addition, $b_\alpha(0) = 0, \pm 1$, so that the potential modification of $\nu_\alpha$, due to the factor $\left(\frac{1}{2} - |b_\alpha(0)|^2\right)$, is compensated for by the change in sign of $m_\alpha$, and $\nu_\alpha$ *is preserved*.

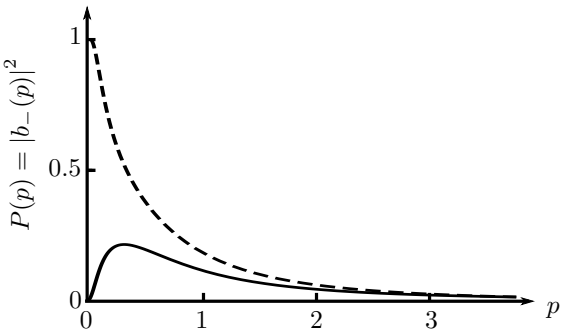


Figure 2.2: Probability of occupying the upper band for a single Dirac point ($\alpha = -1$) with the effective speed of light set to $c = 1$, following a quench of $m_\alpha$. Sign-preserving quench, $m_- = -1 \to m'_- = -0.1$ (solid line) and a sign-changing quench, $m_- = -1 \to m'_- = 0.1$ (dashed line). In both cases, $b_-(\infty) = 0$, corresponding to the time-independence of $\nu_-(t)$ using Eq. (2.2). The sign-changing quench yields $|b_-(0)|^2 = 1$, but the contribution to $\nu_-(t)$ in Eq. (2.2) is compensated for by the change in sign of $m_-$. As a result, $\nu_-$ is unchanged from its initial value.

Let us, once again, specialise to the $\alpha = -1$ Dirac point, without loss of generality. We now consider a quench $m_- \to m'_-$. The system is initially prepared in the ground state of $\hat{H}_-(m_-)$, corresponding to the filled lower band, $|l_-\rangle$. Immediately after the quench, we may decompose $|l_-\rangle$ into the eigenstates of the post-quench Hamiltonian:

$$\begin{aligned} a_-(p) &= f_-(p, m_-) f_-(p, m'_-) + f_+(p, m_-) f_+(p, m'_-), \\ b_-(p) &= f_+(p, m_-) f_-(p, m'_-) - f_-(p, m_-) f_+(p, m'_-). \end{aligned} \tag{2.9}$$

The probability of being in the upper band, $|b_-(p)|^2$, is plotted in Fig. 2.2. In particular, one obtains $b_-(\infty) = 0$ and $b_-(0) = 0$ ($b_-(0) = \pm 1$) for sign-preserving (sign-changing) mass quenches. As a result, the *Chern number is unchanged from its initial value*, even if one quenches between different phases.

### Linear Sweeps

We extend the results for the Chern number preservation to linear, time-dependent, sweeps. We again consider $\alpha = -$ and set $m_- = \frac{t}{\tau}$ in Eq. (1.19), corresponding to a sign changing sweep over the interval $t \in [-\infty, \infty]$. We prepare the system in the ground state at $t = -\infty$ and track the subsequent evolution [73]. At any instant of time the state can be written as a superposition of the eigenstates of $\hat{H}_-(t)$:

$$|\psi_-(p, \theta, t)\rangle = a_-(p, t)\, |l_-(p, \theta, t)\rangle + b_-(p, t)\, |u_-(p, \theta, t)\rangle\,. \tag{2.10}$$

Using Eq. (2.5) and Eq. (2.6), one obtains

$$\nu_-(t) = \operatorname{sign} t \left( \frac{1}{2} - |b_-(0, t)|^2 \right) + \left[ \lim_{p \to \infty} - \lim_{p \to 0} \right] \left[ \frac{p}{2\sqrt{p^2 + \frac{t^2}{\tau^2}}} (a_-^*(p, t) b_-(p, t) + \text{h.c.}) \right]. \tag{2.11}$$

We now need to evaluate the coefficients $a_-(p,t)$ and $b_-(p,t)$ for $p = 0$ and $p = \infty$. For $p = 0$ the eigenstates of $\hat{H}_-(t)$ are

$$|l_-(0,\theta,t)\rangle = \begin{pmatrix} e^{-i\theta}\sqrt{\frac{1}{2}(1-\operatorname{sign} t)} \\ \sqrt{\frac{1}{2}(1+\operatorname{sign} t)} \end{pmatrix}, \tag{2.12}$$

$$|u_-(0,\theta,t)\rangle = \begin{pmatrix} -e^{-i\theta}\sqrt{\frac{1}{2}(1+\operatorname{sign} t)} \\ \sqrt{\frac{1}{2}(1-\operatorname{sign} t)} \end{pmatrix}. \tag{2.13}$$

These are time-independent for $t \neq 0$. For $p = 0$ the system remains in the lower band up to $t = 0^-$. At $t = 0^+$, the mass parameter changes sign, and at $p = 0$, it overlaps completely with the upper band:

$$|\langle l_-(0,\theta,0^-) \,|\, u_-(0,\theta,0^+)\rangle| = 1. \tag{2.14}$$

Henceforth, the $p = 0$ mode remains in the upper band. At $p = \infty$, the eigenstates are independent of time:

$$|l(\infty,\theta,t)\rangle = \begin{pmatrix} e^{-i\theta}\sqrt{\frac{1}{2}} \\ \sqrt{\frac{1}{2}} \end{pmatrix}, \tag{2.15}$$

$$|u(\infty,\theta,t)\rangle = \begin{pmatrix} -e^{-i\theta}\sqrt{\frac{1}{2}} \\ \sqrt{\frac{1}{2}} \end{pmatrix}. \tag{2.16}$$

The system remains in the lower band for $k = \infty$. Summarising, one obtains

$$|b_-(0,t)| = \begin{cases} 0, & t < 0 \\ 1, & t > 0 \end{cases} \quad \text{and} \quad |b_-(\infty,t)| = 0 \quad \forall t. \tag{2.17}$$

This parallels the situation for the quench protocol as shown by the dashed line in Fig. 2.2. The preservation of $\nu_-$ follows by substituting Eq. (2.17) into Eq. (2.11).

## 2.2 Preservation of the Chern Number

Having established the preservation of $\nu$ using the low-energy Dirac Hamiltonian, we now examine the non-equilibrium response of the Haldane model, without the low-energy approximation. Under a quantum quench it is possible to occupy high energy states, far from the Dirac points. Nevertheless, we show here that the result obtained for the Dirac Hamiltonians can be extended to the Haldane model.

Immediately after a quantum quench, the wave function, and hence the Chern number, remains unchanged. Explicitly, $\lim_{t\to 0^+} |\psi(t)\rangle = |\psi_0\rangle$, where $|\psi_0\rangle$ is the pre-quench ground-state and $|\psi(t)\rangle$ is the post-quench state. It follows that $\nu$ is continuous at $t = 0$. In order to prove the preservation of the Chern number, we only need to show that $\dot{\nu} = 0$, under unitary time-evolution.

Taking the time derivative of Eq. (1.13) and using Stokes theorem, one obtains

$$\dot{\nu} = \frac{1}{2\pi} \oint_{\partial \mathrm{BZ}} dk^\mu \dot{A}_{k_\mu}. \tag{2.18}$$

In general, $\dot{A}_{k_\mu} = i\langle\dot{\psi}|\partial_{k_\mu}|\psi\rangle + i\langle\psi|\partial_{k_\mu}|\dot{\psi}\rangle = \langle\psi|[\partial_{k_\mu}, \hat{H}]|\psi\rangle$, or equivalently, $\dot{A}_{k_\mu} = \langle\psi|(\partial_{k_\mu}\hat{H})|\psi\rangle$, and we further notice that it is gauge invariant. Expanding the initial state $|\psi\rangle = \sum_{\gamma=l,u} c_\gamma e^{-iE_\gamma t}|\gamma\rangle$ in terms of the eigenstates $|\gamma\rangle$ of the final Hamiltonian

$$\dot{A}_{k_\mu}(k_x, k_y) = \sum_{\gamma=l,u} c_\gamma c^*_{\gamma'} \langle\gamma'|\partial_{k_\mu}\hat{H}|\gamma\rangle e^{i(E_{\gamma'}-E_\gamma)t}. \tag{2.19}$$

In general, this is time-dependent. However, using the symmetries of the final Hamiltonian, the components of $\dot{A}_{k_\mu}$ along the Brillouin zone boundary occur in equal pairs and cancel in the line integral for $\dot{\nu}$. For example, within the upper and lower triangles depicted in Fig. 2.3, $\hat{H}(k_x, k_y) = \hat{H}^*(k_x, -k_y)$. Periodicity in $k$-space ensures that $\hat{H}(k_x, k_y) = \hat{H}(k_x, -k_y)$ along the corresponding zone boundaries, so that $\hat{H}$ is real on these segments. It follows that $\dot{A}_{k_x}(k_x, 2\pi/3) = \dot{A}_{k_x}(k_x, -2\pi/3)$ for $k_x \in (-\frac{2\pi}{3\sqrt{3}}, \frac{2\pi}{3\sqrt{3}})$,

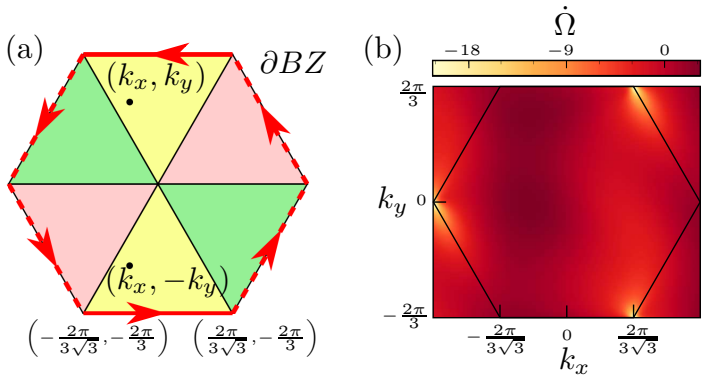


Figure 2.3: First Brillouin zone of the Haldane model. (a) In each of the triangles the Berry connection and the Berry curvature are time-dependent. However, the Chern number is given by the line integral of the Berry connection along the zone boundary, as indicated by the arrows. Following a quench, the time-dependent contributions to $\nu$ from opposite sides of the boundary cancel each other. (b) Time derivative of the Berry curvature for $M = 1$, $t_1 = 1$ and $t_2 = 1/3$ following a quench from the non-topological phase with $\varphi = \pi/6$ to the topological phase with $\varphi = \pi/3$. Although $\dot{\Omega} \neq 0$, numerical integration over the Brillouin zone confirms that $\dot{\nu} = 0$.

so these two contributions to $\dot{\nu}$ cancel. By symmetry, this argument holds also for the other two pairs of opposite triangles in Fig. 2.3, so that $\dot{\nu} = 0$. This, together with the continuity of $\nu$ at $t = 0$, concludes the proof of the *preservation of the Chern number under quantum quenches between different points of the phase diagram.*

## 2.3 Spin Textures in Quasi-Momentum Space

An intuitive way to understand the persistence of $\nu$ following a quantum quench is in terms of spin-textures in quasi-momentum space. The Dirac Hamiltonian in Eq. (1.19) can be recast as an effective spin in a $\mathbf{p}$-dependent magnetic field, $\mathbf{h}_\alpha(\mathbf{p})$. Explicitly, $\hat{H}_\alpha(\mathbf{p}) \equiv -\mathbf{h}_\alpha(\mathbf{p}) \cdot \boldsymbol{\sigma}/2$, where $\boldsymbol{\sigma}$ are the Pauli matrices. In equilibrium, the phases with $\nu_\alpha = \pm 1/2$ correspond to meron spin configurations which wind on the upper (lower) half-sphere [56]. Following a quantum quench, the spins precess in the effective magnetic field of the new Hamiltonian, preserving the topological characteristics of the initial spin

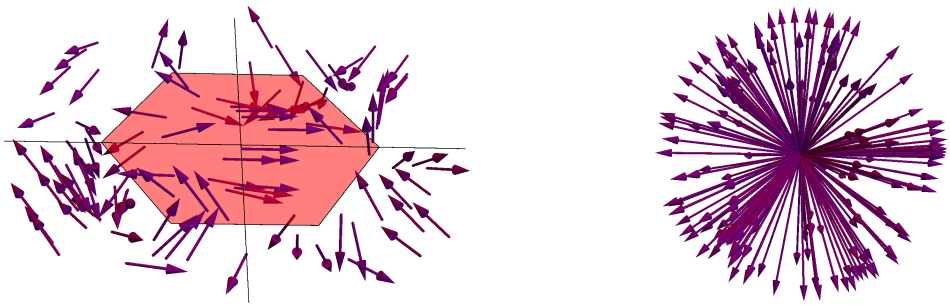

(a) (b)

Figure 2.4: (a) In quasi-momentum space, the Hamiltonian of the Haldane model, Eq. (1.16), can be thought of as the Hamiltonian for a spin in a **k**-dependent magnetic field. In equilibrium, the spins are aligned to the effective magnetic field. The resulting spin texture, in the topological phase, maps the Brillouin zone (shaded area) onto the sphere (b). A quench of the effective magnetic field results into the precession of the spins around the new field directions, which does not unwind the initial spin configuration.

configuration. A similar argument may also be applied to the Haldane model (1.15) in **k**-space; see Fig. 2.4. Indeed, one expects the preservation of topological invariants under time evolution to be a general feature for non-interacting fermions in a periodic system, where each **k**-state evolves unitarily under some Hamiltonian $\hat{H}(\mathbf{k})$, provided $\hat{H}(\mathbf{k})$ is smoothly varying in **k**-space. The persistence of the topological invariant of a state, even under changes in the topology of the underlying Hamiltonian, has also been noted in the context of quantum quenches of topological superfluids [129, 140] and Floquet-Chern insulators [132]. In principle, the preservation of the Chern index may be measured experimentally by expansion-imaging techniques, which can allow the wave functions of the occupied single particle states to be fully determined across the Brillouin zone [61, 80, 141, 142]. It is important to stress, however, that this does *not* imply the preservation of the Hall response. The latter depends on the final state Hamiltonian, not just the initial state. Out of equilibrium, the usual TKNN formula [13] does not apply [2]. We discuss the Hall response in the next Chapter.

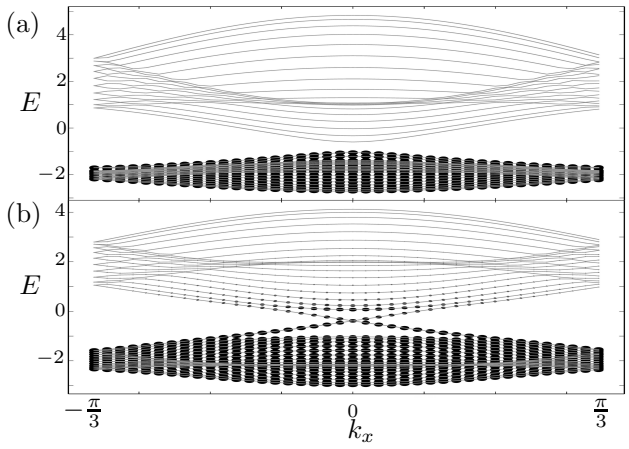


Figure 2.5: Energy spectrum of the Haldane model obtained by exact diagonalisation on a finite-size strip of width $N = 20$ unit cells with armchair edges; see Fig. C.1 in Appendix C. We take periodic (open) boundary conditions along (transverse to) the strip and set $t_1 = 1$, $t_2 = \frac{1}{3}$, and $M = 1$. (a) Equilibrium population of the energy levels in the non-topological phase with $\varphi = \frac{\pi}{6}$. (b) Re-population of the levels after a quench to the topological phase with $\varphi = \frac{\pi}{3}$, corresponding to the solid arrow in Fig. 2.1 (a). The size of the dots is proportional to the probability of finding a particle in the mode. Post-quench, the filling of the edge states and the bands is non-trivial.

## 2.4 Edge States

In the above discussion we have demonstrated that the value of $\nu$ is unchanged as one quenches and sweeps between different phases. However, there is a fundamental distinction between the topological and non-topological phases, due to the presence or absence of edge states in a finite-size sample [143]. In quenching between phases of different topological character, these edge states will either appear or disappear, depending on the direction of the quench. This is confirmed in Fig. 2.5, which shows the re-construction and re-population of the energy levels following a quench from the non-topological phase to the topological phase. It is readily seen that the edge states emerge and are populated as a result of the quench, in spite of the fact that $\nu$ remains equal to zero in the absence of boundaries. Conversely, a quench from a topological phase to the non-topological

phase eliminates the edge states, whilst $\nu$ remains pinned at unity.

Having examined the re-population of the edge states, we now consider physical observables that depend on these states, including the edge currents and the orbital magnetisation. We first consider these quantities in equilibrium, which already display interesting features.

### Edge Currents and Orbital Magnetisation

We define the local current flowing through the site $l$ by $\hat{\mathbf{J}}_l = -\frac{i}{2}\sum_j \boldsymbol{\delta}_{jl}(t_{lj}\hat{c}_l^\dagger \hat{c}_j - \text{h.c.})$, where $t_{lj}$ is the hopping parameter of the Haldane model between sites $l$ and $j$, $\boldsymbol{\delta}_{jl}$ is the vector displacement of site $l$ from $j$, and the sum is over the nearest and next nearest neighbours. The site indices may be decomposed into the triplet $\{m, n, s\}$ labelling the $x$ and $y$ positions of the unit cell and the sub-lattice index $s = A, B$; see Fig. C.1 in Appendix C. The total longitudinal current flowing along the strip in the $x$-direction at a definite transverse $y$-position is therefore given by $J_n^x = \langle \hat{J}_n^x \rangle = \sum_{ms} \langle \hat{J}_{mns}^x \rangle$. In Fig. 2.6(a) we plot this current within the topological phase for $M = 0$ and $\varphi = \pi/3$. The presence of the counter-propagating edge currents is readily seen. In Fig. 2.6(b) we show the dependence of these edge currents on $\varphi$ where, for clarity, we define the edge currents $J_{edge}^x$ precisely on the sample boundaries. Measurements of edge currents have been performed for ladder systems [144], and other forms of local imaging have been proposed [145]. Somewhat surprisingly, *the edge currents vanish on loci (i.e. for certain values of $M$ and $\varphi$) within the topological phase, in spite of the presence of edge states in the spectrum.* The edge currents are composed of counter-propagating contributions which cancel at $\varphi = \pi/2$; this can be seen in Fig. C.2 in Appendix C. Moreover, the longitudinal currents $J_n^x$ exhibit $\pi$-periodicity in $\varphi$. This is a consequence of being at half-filling and occurs in spite of the fact that the Hamiltonian and the current operator have a periodicity of $2\pi$. To prove the $\pi$-periodicity in $\varphi$ we first note that both the Hamiltonian and the current operator change sign under the transformation $M \to -M$,

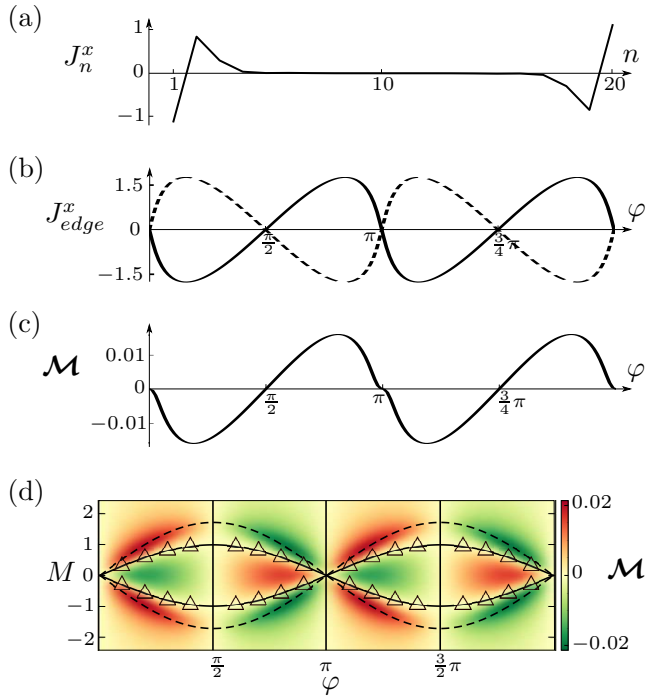


Figure 2.6: Equilibrium properties of the Haldane model on a finite-size strip as used in Fig. 2.5. (a) Total longitudinal current $J_n^x$ along the strip as a function of the transverse spatial index $n \in 1, \ldots, 20$, for $M = 0$ and $\varphi = \pi/3$. (b) Edge currents corresponding to $J_n^x$ with $n = 1$ (solid) and $n = 20$ (dashed) for $M = 0$. The edge currents exhibit $\pi$-periodicity in $\varphi$ and vanish when $\varphi = \pi/2$. (c) Orbital magnetisation $\boldsymbol{\mathcal{M}}$ as a function of $\varphi$ for $M = 0$. (d) Intensity plot of $\boldsymbol{\mathcal{M}}$ where the dashed lines correspond to the boundaries of the topological phases. Numerically we observe that $\boldsymbol{\mathcal{M}}$ vanishes on the loci $M = \pm \sin\varphi$ (solid) within the topological phases. The loci are fits to the numerical data (triangles) where $\boldsymbol{\mathcal{M}} = 0$. The magnetisation also vanishes on the vertical lines $\varphi = \pi/2, \pi, 3\pi/2, \ldots$ as follows from symmetry considerations.

$\varphi \to \varphi + \pi$, $\hat{c}_{mnA} \to \hat{c}_{mnA}$, $\hat{c}_{mnB} \to -\hat{c}_{mnB}$, thereby interchanging the upper and the lower bands. At half-filling, we fill only the lower band, and it follows that $J_n^x(M, \varphi) = J_n^x(-M, \varphi + \pi)$. In addition, the current changes sign under the parity transformation $x \to -x$. This interchanges the sub-lattices and corresponds to $M \to -M$ and $\varphi \to -\varphi$. It follows that $J_n^x(M, \varphi) = -J_n^x(-M, -\varphi) = J_n^x(-M, \varphi)$, where in the last step we use the transformation properties under time-reversal. Combining these relations, one

obtains the $\pi$-periodicity in $\varphi$ and the vanishing of the longitudinal currents for $\varphi = \pi/2$.

Similar arguments also apply to the (lattice discretisation of the) orbital magnetisation:

$$\boldsymbol{\mathcal{M}} = \frac{1}{2\mathcal{A}} \int d^2r\, \mathbf{r} \times \langle \hat{\mathbf{J}}(\mathbf{r}) \rangle, \tag{2.20}$$

where $\hat{\mathbf{J}}(\mathbf{r})$ is the local current density operator and $\mathcal{A}$ is the area. As shown in Fig. 2.6(c) this also vanishes within the topological phases and has $\pi$-periodicity in $\varphi$ [146, 147]. Our numerical computations also reveal that the magnetisation vanishes on a sinusoidal locus $M = \pm \sin(\varphi)$ within the topological phases; see Fig. 2.6(d). In addition, $\boldsymbol{\mathcal{M}}(M, \varphi)$ has extrema at $M = 0$ and on the topological phase boundaries, $M = \pm\sqrt{3}\sin(\varphi)$, for fixed $\varphi$. Away from half-filling, the particle-hole symmetry is broken and the periodicity of the currents and the magnetisation is restored to $2\pi$. The increase or decrease of the edge currents depends on the sign of the doping and on the Chern index, as shown in Fig. C.3 in Appendix C. Further details on the equilibrium edge currents and magnetisation are given in Appendix C.

## 2.5 Dynamics of the Edge Currents

Having discussed the equilibrium properties of the edge currents we now consider their response to quantum quenches. In Fig. 2.7 we show quenches from the topological to the non-topological phase. The edge currents decay towards new values that are numerically close, but *not equal*, to the equilibrium values of the post-quench Hamiltonian. In Fig. 2.8 we show magnified images of Fig. 2.7 at later times. It may be seen that the system is generically left in an excited state following a quantum quench, as follows from the evolution under a unitary Hamiltonian. Nonetheless, the values of the steady-state current, reached after the quench, are constrained by the final Hamiltonian, not just the initial state. This occurs in the spite of the fact that the Chern index is preserved in infinite-size samples. In Fig. 2.9 we show further examples of this behaviour for

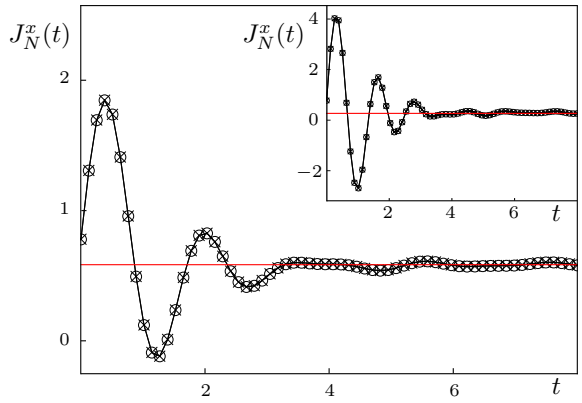


Figure 2.7: Dynamics of the edge current $J_N^x(t)$ for $N = 30$ (circles) and $N = 40$ (crosses) following a quantum quench between the topological phase and the non-topological phase with $t_1 = 1$, $t_2 = \frac{1}{3}$ and fixed $\varphi = \pi/3$. Quenches from $M = 1.4$ to $M = 1.6$ (main panel) and from $M = 1.4$ to $M = 2.2$ (inset) showing that the edge currents approach new equilibrium values. For the chosen parameters, these are very close to the ground-state expectation values of $J_N^x$ in the final Hamiltonian, as indicated by the horizontal lines.

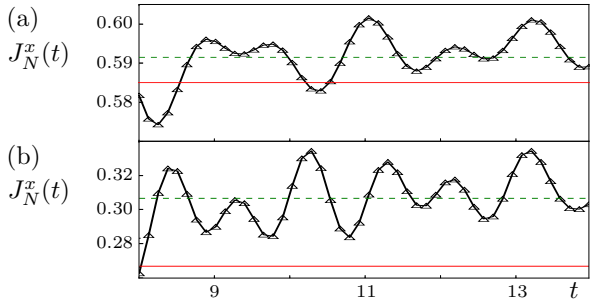


Figure 2.8: Late-time dynamics of the edge current $J_N^x(t)$ following a quantum quench from the topological to the non-topological phase. Panels (a) and (b) correspond to the parameters used in Fig. 2.7 and the inset respectively. The horizontal solid line indicates the ground-state value of the edge current in the final Hamiltonian. The system is generically left in an excited state due to unitary evolution under the post-quench Hamiltonian; the dashed line corresponds to the time average of the late-time current. Nonetheless, the edge current is close to the ground-state value and is constrained by the final Hamiltonian; see Fig. 2.7. This occurs in spite of the preservation of the Chern index in infinite-size systems.

different quench parameters. Quenches from the non-topological to topological phases exhibit similar behaviour; see Fig. 2.10. We also numerically observe that the oscillation frequencies coincide for quenches to the same final Hamiltonian; see Fig. 2.10.

Further insight into the non-equilibrium evolution may be gleaned from the time-evolution of the longitudinal currents across the two-dimensional system. As shown in Fig. 2.11, the damped oscillations of the edge currents is accompanied by the light-cone spreading of the currents into the interior of the sample. It would be interesting to observe this dynamics in experiment, which is in principle possible if local imaging is available [145]. From Fig. 2.11, it is clear that, eventually, the steady-state value reached by the edge currents will be perturbed by the onset of finite-size effects. In the

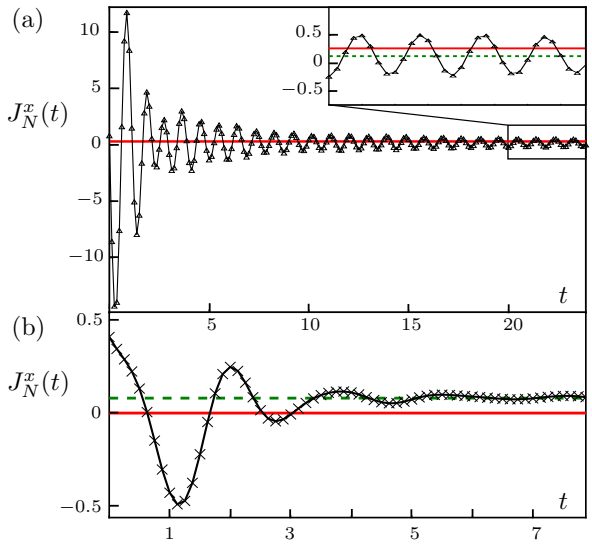


Figure 2.9: (a) Dynamics of the edge current $J_N^x(t)$ following a quantum quench from the topological to the non-topological phase with $N = 60$, $t_1 = 1$, $t_2 = 1/3$, $\varphi = \pi/3$ and $M = 1.4 \to -2.2$. The inset shows a magnified view of the edge current at late times. The solid horizontal line corresponds to the ground-state value of the edge current for the post-quench Hamiltonian. The system is generically left in an excited state under unitary evolution. The dashed line corresponds to the time-averaged edge current at late times. (b) Edge current $J_N^x(t)$ following a quench within the topological phase for $N = 40$, $t_1 = 1$, $t_2 = 1/3$, $M = 1.4$ and $\varphi = \pi/3 \to \pi/2$. Again, the system is left in a weakly excited state.

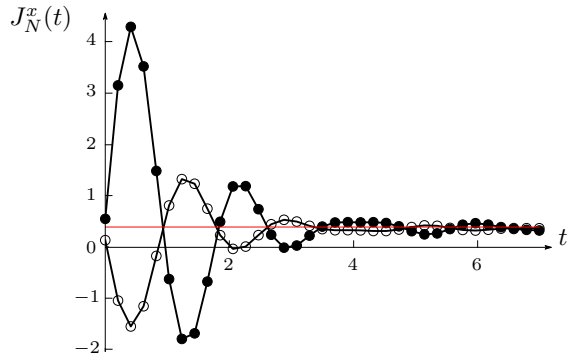


Figure 2.10: Edge current $J_N^x(t)$ following a quantum quench within the topological phase (filled circles) and from the non-topological phase to the topological phase (empty circles). We set $N = 30$, $t_1 = 1$, $t_2 = 1/3$ and $\varphi = \pi/3$ and consider quenches of the mass parameter $M = 0.5 \to 1.4$ (full circles) and $M = 2.2 \to 1.4$ (empty circles). The horizontal line corresponds to the ground-state expectation value of the edge current for the post quench Hamiltonian. The coincidence between the oscillation frequencies is consistent with the fact that we quench to the same final Hamiltonian.

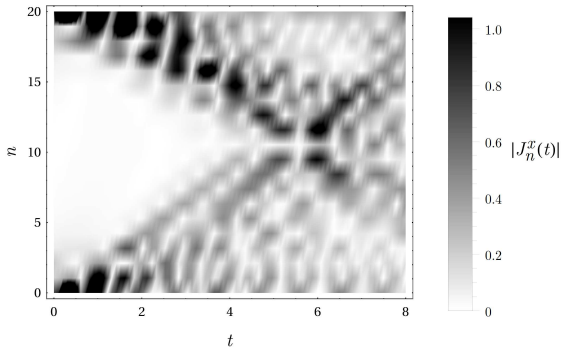


Figure 2.11: Dynamics of the currents $|J_n^x(t)|$ following a quantum quench from the topological to the non-topological phase for the parameters used in the inset of Fig. 2.7. The damped oscillations of the edge currents are clearly visible, as is the light-cone spreading of the currents into the interior of the sample, where $c = 3t_1/2\hbar = 3/2$ is the effective speed of light of the Haldane model. The waves propagating from the two edges meet at time $t \sim (N/2)\sqrt{3}/2c \sim 5.77$, leading to resurgent oscillations in finite-size samples; see Fig. 2.12.

previous examples, we have considered time scales which are simultaneously long enough to display the relaxation of the post-quench edge currents and short enough to avoid the

onset of finite-size effects. In fact, at later times, we see resurgent oscillations, due to the spreading of the currents from the opposite edge; see Fig. 2.12. The onset timescale

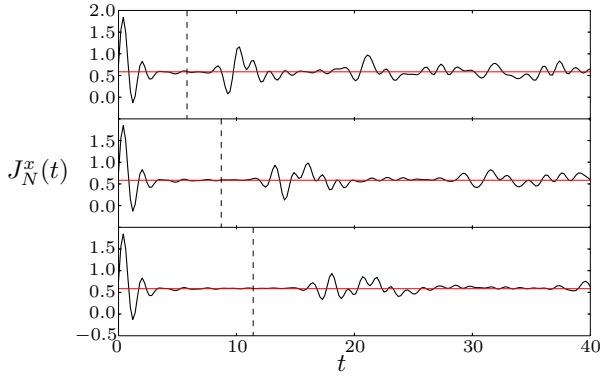


Figure 2.12: Time dependence of the edge current $J_N^x(t)$ after a quantum quench from the topological phase with $M = 1.4$ to the non-topological phase with $M = 1.6$, keeping $t_1 = 1$, $t_2 = 1/3$ and $\varphi = \pi/3$ fixed. This corresponds to the main panel of Fig. 2.7 over a longer time duration. The three panels from the top to the bottom correspond to strips of width $N = 20$, 30 and 40 respectively. The appearance of resurgent oscillations is evident in all three panels due to the finite width of our system. The dashed lines indicate the time-scale $t = (N/2)\sqrt{3}/2c$ at which signals propagating from the two edges meet, corresponding to the onset of finite-size effects. The horizontal line corresponds to the ground-state expectation value of the edge current for the post quench Hamiltonian.

for these resurgent oscillations increases with the width of the strip. This timescale is given by $t = d/2c$ where $d = N\sqrt{3}/2$ is the width of the sample and $c = 3t_1/2\hbar$ is the effective speed of light of the Haldane model. This timescale is indicated by the dashed lines in Fig. 2.12. In order to avoid finite-size effects in our predictions we restricted the domain of the previous simulations to be within this time interval. The agreement between the results for $N = 30$ and $N = 40$ in Fig. 2.7 highlights that we are probing the intrinsic dynamics of the edge currents, before finite-size effects play a role.

## 2.6 Summary

In this Chapter we have explored the non-equilibrium dynamics of the Haldane model. We have demonstrated that, in absence of system boundaries, the Chern number is preserved in both quenches and sweeps between different regions of the phase diagram. Similar results were also found by D'Alessio and Rigol [132]. However, in finite-size systems, the edge states may be re-constructed and re-populated leading to changes in the accompanying edge currents. Predictions for experiments include the vanishing of the equilibrium edge currents in the topological phases, and the light-cone spreading of the currents following a quantum quench. The experimental confirmation is in principle possible if local imaging is available [145]. In the next Chapter we further explore the quench dynamics of Chern insulators, investigating the Hall conductance and its relation to the Chern number following a quantum quench.

# Chapter 3

# Hall Response and Non-Equilibrium Dynamics

In this Chapter[1] we further analyse the quench dynamics of Chern insulators. A fundamental and defining signature of equilibrium Chern insulators is the exact quantisation of the Hall response, independently of sample defects [10, 12]. As discussed in the Introduction, its robustness is intimately linked to the topological Chern invariant $\nu$ [13, 148], via the celebrated TKNN formula [13]

$$\sigma_{xy} = \nu q^2/h, \tag{3.1}$$

where $\nu$ is the Chern number and $q = -e$ is the charge of the carriers. As shown in the previous Chapter, the Chern number is robust under unitary evolution, even following quenches between topological and non-topological phases [1, 132]. However, this does *not* imply the persistence of all physical observables. For example, the presence or absence of edge states in finite-size samples, depends on the final Hamiltonian and not just the initial state. The re-population of these states following a quantum quench leads

[1]The results presented here are published in Ref. [2].

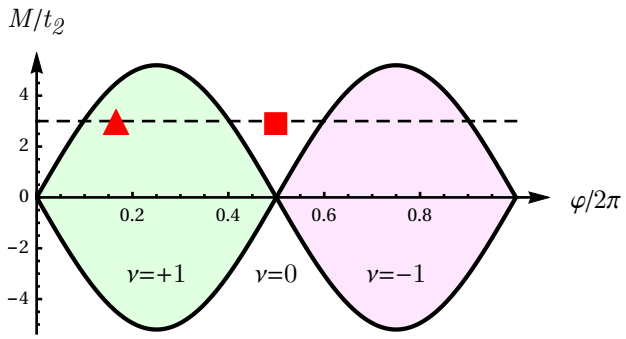


Figure 3.1: Phase diagram of the Haldane model showing topological ($\nu = \pm 1$) and non-topological phases ($\nu = 0$) [57]. The triangle and the square indicate the starting points of quenches along the dashed line, as shown in Figs 3.3 and 3.4.

to changes in the edge currents and the orbital magnetisation [1]. This is accompanied by the light-cone spreading of currents into the interior of the sample, and the onset of finite-size effects.

In a similar way, in this Chapter, we show that the Hall response does not necessarily remain quantised, providing explicit results for the Haldane model [57]. This is consistent with recent calculations by Wang *et al.* [149, 150], who have investigated the Hall response following a quantum quench, including an external reservoir to induce decoherence and reduce to the diagonal ensemble. The results are also in good agreement with analytical approximations based on the low-energy Dirac Hamiltonian. See also Refs [151, 152] for work on the Hall response out of equilibrium.

In this Chapter we also examine in more detail the dynamics of the edge currents in finite-size systems with open boundary conditions along one direction. In contrast to the previous Chapter, where we focused on the dynamics *before* the onset of finite-size effects, we here investigate the late-time dynamics. In particular, we show that after multiple traversals of the sample, the late-time behaviour is captured by a Generalised Gibbs Ensemble (GGE) [87, 94, 105]. With a view towards cold atom experiments, the final part of this Chapter is dedicated to the effects of harmonic confinement potentials.

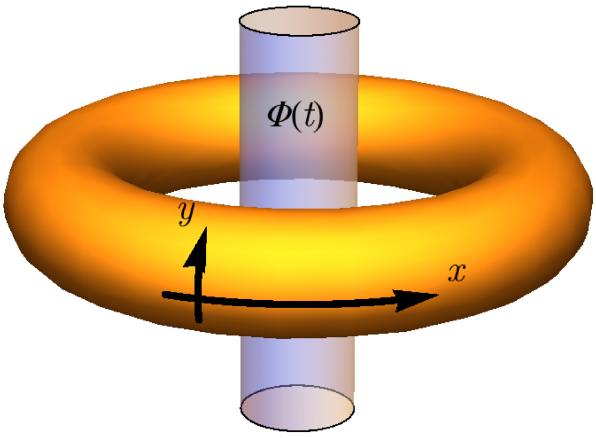


Figure 3.2: Setup used to evaluate the Hall response in the presence of periodic boundary conditions. An auxiliary time-dependent magnetic flux $\Phi(t)$ generates a longitudinal electric field $E_x(t) = -\frac{\partial \Phi(t)}{\partial t}$. Note that this flux does *not* correspond to the time-reversal symmetry breaking parameter $\varphi$ in the Haldane model. The Hall conductance $\sigma_{xy}(t)$ is obtained from the transverse current that is in phase with $E_x(t)$.

## 3.1 Hall Response

In order to further differentiate the physical characteristics of the initial and final states, we examine the Hall response following a quantum quench. We use linear response theory, as done by TKNN in Ref. [13]. Here, however, we focus on a generic excited state, rather than the ground state. In particular, we calculate the in-phase transverse response to an applied time-dependent electric field $\mathbf{E}(t) = \mathbf{E}_0 \cos \omega t$. In the presence of periodic boundary conditions it is convenient to generate this electric field by means of an auxiliary magnetic flux threading a toroidal sample [12, 13, 148]; see Fig. 3.2. For recent work examining the dynamics of one-dimensional currents following "flux quenches" in ring geometries see Ref. [153].

In momentum space, the resulting Hamiltonian may be decomposed into a sum over independent modes $\hat{H} = \sum_{\mathbf{k}} \hat{H}_{\mathbf{k}}$ where $\hbar \dot{\mathbf{k}} = q\mathbf{E}(t)$, or equivalently $\hbar \mathbf{k}(t) = \hbar \mathbf{k}(0) + (q\mathbf{E}_0/\omega) \sin \omega t$. Expanding the Hamiltonian to linear order in $\mathbf{E}_0$ yields $\hat{H}(t) = \sum_{\mathbf{k}} \hat{H}_{\mathbf{k}} +$

$\hat{\mathbf{v}}_{\mathbf{k}}.(q\mathbf{E}_0/\omega)\sin\omega t$, where $\hat{\mathbf{v}}_{\mathbf{k}} = d\hat{H}_{\mathbf{k}}/\hbar d\mathbf{k}$ is the velocity operator. Within the framework of time-dependent perturbation theory it is convenient to expand the state of the system in the basis of the unperturbed ($\mathbf{E}_0 = 0$) post-quench Hamiltonian:

$$|\psi_{\mathbf{k}}(t)\rangle = \sum_{b=l,u} c_{b,\mathbf{k}}(t) e^{-iE_{b,\mathbf{k}}t/\hbar} |b,\mathbf{k}\rangle . \tag{3.2}$$

Here $b = l, u$ refer to the lower and upper band respectively and $E_{b,\mathbf{k}}$ are the energies of the single-particle states; see Fig. 1.6. The case where the coefficients $c_{b,\mathbf{k}}$ are constant describes the unperturbed ($\mathbf{E} = 0$) evolution of the system under the post-quench Hamiltonian. In the presence of $\mathbf{E}$, first order perturbation theory yields $c_{b,\mathbf{k}}(t) \approx c_{b,\mathbf{k}} + \delta c_{b,\mathbf{k}}(t)$ where

$$\delta c_{b,\mathbf{k}}(t) = -\frac{i}{\hbar} \sum_{b'=l,u} \int_0^t dt' \mathcal{M}_{b,b'}(\mathbf{k},t') e^{i\Delta_{b,b'}(\mathbf{k})t'} c_{b',\mathbf{k}}. \tag{3.3}$$

Here, $\Delta_{b,b'}(\mathbf{k}) \equiv (E_{b,\mathbf{k}} - E_{b',\mathbf{k}})/\hbar$, and $\mathcal{M}_{b,b'}(\mathbf{k},t') \equiv \langle b,\mathbf{k}| \hat{\mathbf{v}}_{\mathbf{k}}.(q\mathbf{E}_0/\omega)\sin\omega t' |b',\mathbf{k}\rangle$ is the matrix element of the perturbation. The transverse current $\hat{J}_y = \sum_{\mathbf{k}} \langle \psi_{\mathbf{k}}(t) \,|\, q\hat{v}_y \,|\, \psi_{\mathbf{k}}(t)\rangle$, which flows in response to an electric field along the $x$-direction, is examined in order to determine the Hall conductance. In this pursuit, we neglect the zeroth order contribution which arises in the absence of $E_0^x$, due the redistribution of carriers between the bands following the quench. At first order in $E_0^x$

$$J_y^{(1)} = 2\,\mathrm{Re}\left[\sum_{\mathbf{k},b,b'} c_{b,\mathbf{k}}^* \delta c_{b',\mathbf{k}}(t) e^{i\Delta_{b,b'}(\mathbf{k})t} \langle b,\mathbf{k}| \, e\hat{v}_y \, |b',\mathbf{k}\rangle\right]. \tag{3.4}$$

Substituting Eq. (3.3) into Eq. (3.4) and restricting attention to frequencies below the gap $\omega \ll \Delta_{b,b'}(\mathbf{k})$, one obtains

$$J_y^{(1)} = -\frac{E_x}{\hbar\omega} \sum_{\mathbf{k},b,b'} \mathrm{Re}\left[\mathcal{C}\left(\frac{e^{i\omega t}}{\omega + \Delta_{b,b'}(\mathbf{k})} + \frac{e^{-i\omega t}}{\omega - \Delta_{b,b'}(\mathbf{k})}\right)\right], \tag{3.5}$$

where $\mathcal{C} \equiv -i|c_{b,\mathbf{k}}|^2 \langle b,\mathbf{k}| \, q\hat{v}_y \, |b',\mathbf{k}\rangle \langle b',\mathbf{k}| \, q\hat{v}_x \, |b,\mathbf{k}\rangle$. In order to define the Hall conduc-

tance we extract the contribution to $J_y^{(1)}$ that is in phase with the electric field. Denoting $J_y^{(1)} = I_y \cos\omega t + \tilde{I}_y \sin\omega t$ we define $\sigma_{xy}(\omega) \equiv I_y/AE_x$, where $A$ is the area of the sample. This yields

$$\sigma_{xy}(\omega) = \frac{q^2}{2\pi h} \sum_b \int d^2k \, |c_{b,\mathbf{k}}|^2 \tilde{\Omega}_b(\mathbf{k}), \tag{3.6}$$

where

$$\tilde{\Omega}_b(\mathbf{k}) = -i \sum_{b' \neq b} \frac{\langle b, \mathbf{k}| \, \hat{v}_x \, |b', \mathbf{k}\rangle \, \langle b', \mathbf{k}| \, \hat{v}_y \, |b, \mathbf{k}\rangle - \text{H.c.}}{\omega^2 - \Delta_{b,b'}(\mathbf{k})^2}. \tag{3.7}$$

In the limit $\omega \to 0$, $\tilde{\Omega}_b(\mathbf{k})$ reduces to the Berry curvature of the $b$-th band, and the post-quench d.c. Hall conductance is given by

$$\sigma_{xy}(0) = \frac{q^2}{2\pi h} \sum_b \int d^2k \, |c_{b,\mathbf{k}}|^2 \Omega_b(\mathbf{k}), \tag{3.8}$$

in agreement with Refs [149, 150]. An analogous result is also found in the context of Floquet-Chern insulators [133]. Equation (3.8) provides a generalisation of the TKNN formula [13] to handle (arbitrarily prepared) excited states. The usual TKNN formula is recovered in the limit where $|c_{l,\mathbf{k}}|^2 = 1$ and $|c_{u,\mathbf{k}}|^2 = 0$, corresponding to the ground state with $\sigma_{xy}(0) = \nu q^2/h$. The result (3.8) has a straightforward physical interpretation in terms of a semi-classical Boltzmann-like approach. The centre of mass velocity of a wave-packet with momentum $\mathbf{k}$ and band index $b$ is given by $\dot{\mathbf{r}}_{b,\mathbf{k}} = \partial\varepsilon_b(\mathbf{k})/\hbar\partial\mathbf{k} - (\dot{\mathbf{k}} \times \hat{z})\Omega_b(\mathbf{k})$, where $\hbar\dot{\mathbf{k}} = q\mathbf{E}_0$. The second term is the anomalous velocity associated with the Berry curvature $\Omega_b(\mathbf{k})$ [154–157], where $\hat{z}$ is a unit vector perpendicular to the sample. The corresponding current is given by

$$\mathbf{J} \equiv \mathbf{J}^{(0)} + \mathbf{J}^{(1)} = \sum_b \int \frac{d^2k}{(2\pi)^2} \, q\dot{\mathbf{r}}_{b,\mathbf{k}} |c_{b,\mathbf{k}}|^2. \tag{3.9}$$

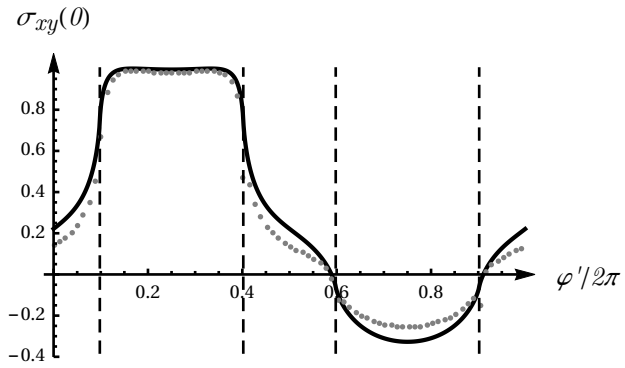


Figure 3.3: Hall conductance in units of $q^2/h$ following a quantum quench from the topological phase with $\varphi = \pi/3$ and $M = 1$ (as indicated by the triangular symbol in Fig. 3.1) to $\varphi = \varphi'$ and $M = 1$. The gray dots are numerical results for the Haldane model obtained from Eq. (3.8). The black solid line is the analytical result for the corresponding quenches in the low-energy Dirac approximation, obtained by summing contributions from Eq. (3.12). The results are in quantitative agreement for small quenches in the vicinity of $\varphi = \pi/3$, and in qualitative agreement for larger quenches. The vertical dashed lines correspond to the boundaries of the topological phases. The Hall conductance remains numerically close to $q^2/h$ for quenches within the same topological phase ($\nu = 1$), but does not saturate at $-q^2/h$ when quenching to the other topological phase ($\nu = -1$).

This yields a contribution proportional to $\mathbf{E}_0$:

$$\mathbf{J}^{(1)} = -\frac{q^2}{2\pi h} \sum_b \int d^2k \, |c_{b,\mathbf{k}}|^2 (\mathbf{E}_0 \times \hat{z}) \Omega_b(\mathbf{k}), \tag{3.10}$$

in agreement with the Hall response (3.8). In equilibrium, this can be used to extract the Berry curvature [158] from measurements of the transverse drift [59, 159].

In Fig. 3.3 we show numerical results for the Hall conductance in the post-quench state, starting from the topological phase. It is readily seen that the values are no longer quantised in integer multiples of $q^2/h$. Similarly, quenches from the non-topological to the topological phase also fail to yield the quantised values found in the equilibrium ground state with $\nu = \pm 1$; see Fig. 3.4. Heuristically, the quench "heats up" the sample by promoting carriers to the upper band which contribute to the Hall response by the

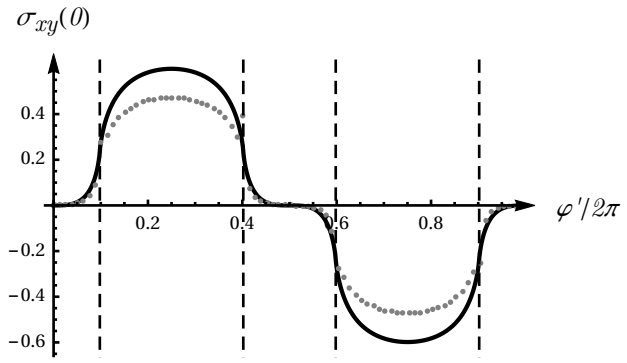


Figure 3.4: Hall conductance in units of $q^2/h$ following a quantum quench from the non-topological phase with $\varphi = \pi$ and $M = 1$ (as indicated by the square symbol in Fig. 3.1) to $\varphi = \varphi'$ and $M = 1$. The gray dots are numerical results for the Haldane model obtained from Eq. (3.8). The black solid line is the analytical result for the corresponding quenches in the low-energy Dirac approximation, obtained by summing contributions from Eq. (3.12). The results are in quantitative agreement for small quenches in the vicinity of $\varphi = \pi$, and in qualitative agreement for larger quenches. The vertical dashed lines correspond to the boundaries of the topological phases.

Berry curvature of that band, thus yielding a non-quantised Hall response.

More generally, we may use Eq. (3.6) to determine the a.c. Hall response for frequencies smaller than the band gap, $\omega \ll \Delta_{b,b'}(\mathrm{k})$; see Fig. 3.5. For larger frequencies,

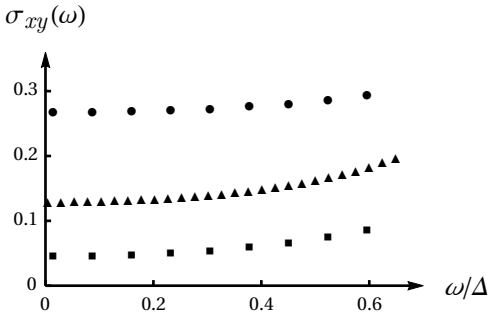


Figure 3.5: Hall response $\sigma_{xy}(\omega)$ in units of $q^2/h$ evaluated using Eq. (3.6) for frequencies below the direct band gap $\Delta \equiv \min[\Delta_{b,b'}(\mathbf{k})]$, following a quantum quench from the topological phase with $M = 1$ and $\varphi = \pi/3$, to the non-topological phase with $M = 1$ and $\varphi = \varphi'$. The three curves correspond to $\varphi' = 7\pi/8$ (circles), $\varphi' = \pi$ (triangles) and $\varphi' = 9\pi/8$ (squares), for which $\Delta \sim 0.67$, 2, and $0.67 \times t_1/\hbar$, respectively.

non-diagonal contributions of the form $c_{b,\mathbf{k}}c^*_{b',\mathbf{k}}$ do not disappear under unitary evolution and the current (3.4) must be employed.

## 3.2 Low-Energy Approximation

Analytical results for the Hall response (3.8) may be obtained within the framework of the low-energy Dirac Hamiltonian for sufficiently small quenches. We recall that, at low-energies, the Haldane model may be described as the sum of two Dirac Hamiltonians $H = H_+ + H_-$ [57], with $H_\alpha$, and $\alpha = \pm$ labels the two inequivalent Dirac points [57]. We also remind the reader that, in this representation, a quench of the Haldane parameters $M \to M'$ and $\varphi \to \varphi'$ corresponds to quenches of the effective masses $m_\alpha \to m'_\alpha$.

For a single Dirac point $\alpha$, the occupation probability amplitudes of the lower and upper bands following an effective mass quench $m_\alpha \to m'_\alpha$, are given by Eq. (2.9)[2]. The Berry curvature of the upper band is given by $\alpha\Omega_{\rm D}(p,m)$, where $\Omega_{\rm D}(p,m) = cpm/(p^2 + m^2c^2)^{3/2}$; the Berry curvature of the lower band has the opposite sign [158]. Substituting these results into Eq. (3.8) it follows that after a quench $m_\alpha \to m'_\alpha$,

$$\sigma^\alpha_{xy}(0) = \frac{\alpha q^2}{2h}\int_0^\infty dp\ \Omega_{\rm D}(p,m'_\alpha)\ \left(|b_\alpha(p)|^2 - |a_\alpha(p)|^2\right). \tag{3.11}$$

More explicitly,

$$\sigma^\alpha_{xy}(0) = \frac{\alpha q^2}{2h}\int_0^\infty dp \frac{cpm'_\alpha(p^2 + c^2 m_\alpha m'_\alpha)}{\sqrt{p^2 + c^2 m_\alpha^2}(p^2 + c^2 {m'_\alpha}^2)^2} \tag{3.12}$$

for the two Dirac points. This is in agreement with Refs [149, 150]. In deriving this result, the integral over the two-dimensional Brillouin zone has been replaced by an integral over the infinite two-dimensional momentum-space. The solid lines in Figs 3.3 and 3.4 correspond to the low-energy approximation $\sigma_{xy}(0) = \sigma^+_{xy}(0) + \sigma^-_{xy}(0)$. The

[2]Actually, Eq. (2.9) only shows the occupations $a_-(p)$ and $b_-(p)$. However, the occupations $a_+(p)$ and $b_+(p)$ have the same form, with $m_+$ and $m'_+$ in place of $m_-$ and $m'_-$.

approximation is in good agreement with the exact numerical results for the lattice model (1.15). For small quenches, which do not explore the non-linear regime of the dispersion relation, the results agree quantitatively. For larger quenches, the approximation breaks down, but it still captures the qualitative features. For large quenches, with $|m - m'| \to \infty$, the contribution to the Hall conductance from a single Dirac point shows plateaus at $(\pm\pi/8)q^2/h$; see Fig. 3.6. These results are consistent with the notion that preservation of $\nu$ does *not* imply the preservation of the Hall response $\sigma_{xy}(0)$. In the absence of interactions, the final state is non-thermal, and characterised by the occupations $c_{b,\mathbf{k}}$ in Eq. (3.8). In this excited state the Hall response need not be quantised.

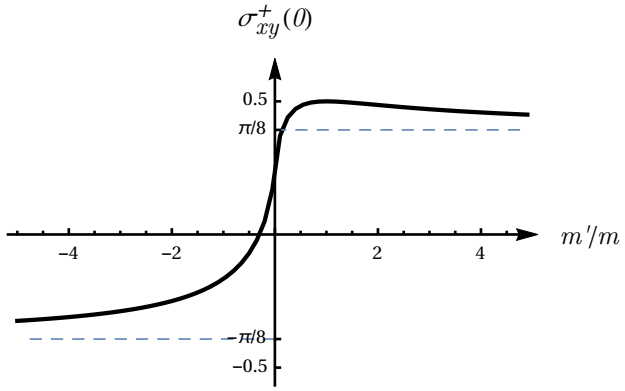


Figure 3.6: Post-quench Hall conductance in units of $q^2/h$ for a single Dirac point ($\alpha = +$), following a quench from $m > 0$ to $m'$. For the same choice of quench parameters, the other Dirac point ($\alpha = -$) displays the opposite Hall conductance. Note that for quenches in the Haldane model, the changes in mass for each Dirac point may differ, yielding a non-zero Hall response. The dashed lines correspond to the asymptotes $\sigma_{xy}(0) = \pm(\pi/8)q^2/h$, which can be determined analytically from Eq. (3.12).

### On the preservation of the Chern number

In contrast to the Chern number, which remains fixed to its initial value, we have shown that the Hall response does change after a quantum quench. We here comment on the time-scales associated with the preservation of the Chern number. It is evident that, for a

finite-size system, the concept of a Chern index must eventually break down at late times following a quantum quench, as one cannot resolve momenta on scales smaller than the inverse system size, $L^{-1}$.[3] The Berry phase acquired upon circulating a plaquette of size $2\pi/L$ becomes ill-defined once the Berry connection $A_{k_\mu}$ becomes as large as $|A_{k_\mu}| \sim L$, and so too does the Chern number. Since, out of equilibrium, $|\psi\rangle$ is in a superposition of ground and excited states, it oscillates at the energy difference $\Delta E_{\boldsymbol{k}}$. The associated Berry connection $A_{k_\mu} = \langle\psi(t)|\partial_{k_\mu}|\psi(t)\rangle$ grows in time, $t$, as $A_{k_\mu} \sim [\partial\Delta E_{\boldsymbol{k}}/\partial(\hbar k)_\mu]t = vt$ where $v = \partial\Delta E_{\boldsymbol{k}}/\partial(\hbar k_\mu)$ is a characteristic difference of band velocities, limited by $v \lesssim 2v_{max}$ with $v_{max}$ the maximum group velocity. Thus $|A_{k_\mu}| \sim L$ when $vt \sim L$. The Chern number becomes ill-defined for timescales larger than the time required for light-cone propagation across the interior of the sample, $t \gtrsim L/2c$.

## 3.3 Generalised Gibbs Ensemble

A quantitative description of the non-thermal post-quench state can be obtained by considering the system in a cylindrical geometry with open boundary conditions along one direction; see Fig. 3.7. In Section 2.5, we showed that the resulting edge currents undergo non-trivial dynamics, due to the presence or absence of edge modes in the spectrum [1]. In particular, we showed that the edge currents decay towards new values that depend on the post-quench Hamiltonian, and not just the initial state; see Figs 2.7, 2.9, 2.10, and 3.8. This evolution is accompanied by light-cone spreading of currents into the interior of the sample, with the eventual onset of finite-size effects and resurgent oscillations; see Fig. 2.11. Here, we study the evolution of the total edge currents at longer times, after many traversals of the sample. We show that the long-time behaviour is captured by a Generalised Gibbs Ensemble (GGE) [87, 94, 105].

In the finite-size cylindrical geometry depicted in Fig. 3.7, the Hamiltonian can be

[3] We are grateful to Prof. B. I. Halperin for this argument.

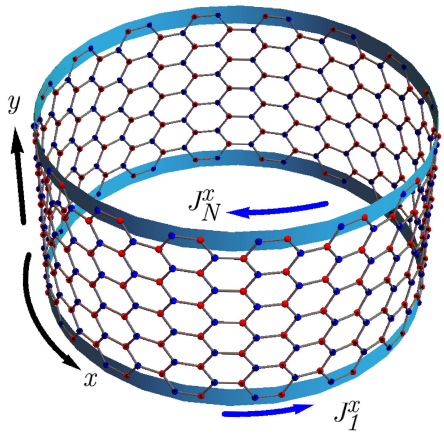


Figure 3.7: Finite-size cylindrical geometry with periodic (open) boundary conditions along the $x$- ($y$-) direction. When $\varphi \neq 0$ there are generically edge currents, $J_1^x$ and $J_N^x$, flowing along the sample boundaries in opposite directions. After a quantum quench, the edge currents evolve as a function of time, and currents flow into the interior of the sample.

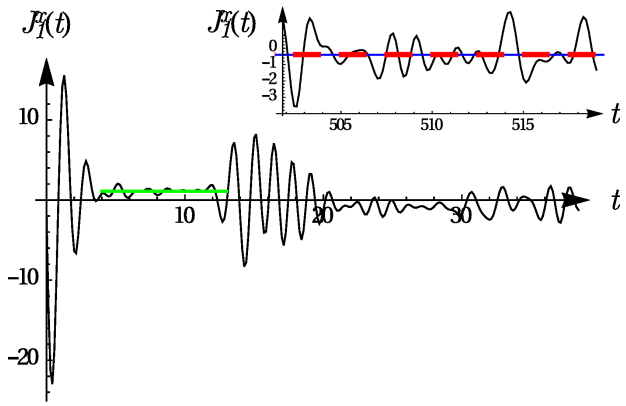


Figure 3.8: (Main) Total edge current $J_1^x(t)$ in units of $qt_1a/\hbar$ following a quantum quench within the topological phase with $\nu = -1$. The time $t$ is measured in units of $\hbar/t_1$. We set $\varphi = \pi/3$ and quench $M$ from 1.4 to $-1.4$. The solid horizontal (green) line corresponds to the time-averaged total edge current, in the quasi-stationary regime before the onset of finite-size traversals. (Inset) Late-time data after 29 traversals of the sample. The dashed (red) line corresponds to the prediction of the GGE. This agrees with the time-average of the late-time data, as shown by the solid horizontal line (blue), to within approximately 3%.

diagonalised as $\hat{H} = \sum_{\Upsilon,k_x} \epsilon_\Upsilon(k_x)\hat{f}^\dagger_\Upsilon(k_x)\hat{f}_\Upsilon(k_x)$, where we have exploited the periodicity in the $x$-direction, and $\Upsilon = 1, \ldots, 2N$ labels the energy levels at each $k_x$-point. In the non-interacting model (1.15), the number operators $\hat{n}_\Upsilon(k_x) = \hat{f}^\dagger_\Upsilon(k_x)\hat{f}_\Upsilon(k_x)$ are the conserved observables $\hat{I}$ of Eq. (1.22). Denoting the pair of indices $\{\Upsilon, k_x\}$ by $\gamma$, the late-time values of the time-averaged edge currents are described by the GGE density matrix

$$\hat{\rho}_{\mathrm{GGE}} = Z^{-1} \exp\left(-\sum_\gamma \lambda_\gamma \hat{n}_\gamma\right), \tag{3.13}$$

where $\hat{n}_\gamma$ are the conserved occupations of a given energy state, $\gamma$ labels the energy level and the momentum index, and $Z = \mathrm{Tr}\exp\left(-\sum_\gamma \lambda_\gamma \hat{n}_\gamma\right)$. Here, the $\lambda_\gamma$'s are generalised inverse temperatures. These are determined by the self-consistency condition that the mode occupations immediately after the quench coincide with the averages computed via the GGE, $\langle \hat{n}_\gamma \rangle = \mathrm{Tr}(\hat{\rho}_{\mathrm{GGE}}\hat{n}_\gamma)$. This yields $\lambda_\gamma = \ln[(1 - \langle \hat{n}_\gamma \rangle)/\langle \hat{n}_\gamma \rangle]$ [94]. In Fig. 3.9 we show the comparison between the time-averaged total edge current along a single edge at late times, and the predictions of the GGE. The results are in excellent agreement.

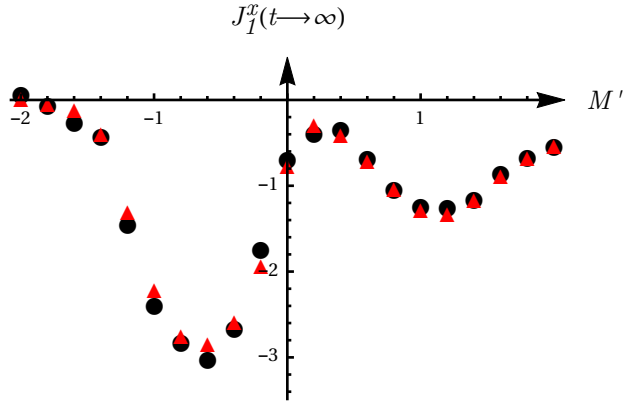


Figure 3.9: Comparison of the time-averaged total edge current in the Haldane model at late times (circles) and the prediction $\left\langle \hat{\rho}_{\mathrm{GGE}}\hat{J}^x_1 \right\rangle$ of the GGE (triangles) for quantum quenches with $\varphi = \pi/3$ held fixed and $M = 1.4 \to M'$. The time averaging is performed over a single traversal period of the finite-size system, following 29 traversals of the sample. The currents are measured in units of $qt_1a/\hbar$.

## 3.4 Confinement Potentials

Thus far, we have explored the dynamics of the Haldane model in toroidal and cylindrical geometries, as periodic boundary conditions provide considerable simplifications for theory and simulation. In order to make clear predictions for experiment, it is instructive to consider finite-size samples with open boundaries, especially due to the use of optical traps for cold atoms. We first consider the effects of transverse confinement in the cylindrical geometry depicted in Fig. 3.7, before discussing the case of rotationally symmetric confinement. For earlier work exploring the effects of trapping potentials on the equilibrium edge physics of topological systems see Refs [160, 161].

We consider the Haldane model in the setup shown in Fig. 3.7, with an additional harmonic confinement potential applied along the $y$-direction, $V(y) \propto (y - y_0)^2$. Here $y_0$ is the centre of the trap which we take to be located at the midpoint of the strip. It is convenient to parameterise the potential as

$$V_n = \mathcal{C} \left( \frac{n - N/2}{\zeta - N/2} \right)^2 , \tag{3.14}$$

where $n = 1, \ldots, N$ labels the row of the strip, $\zeta$ controls the effective width of the confined sample, and $\mathcal{C}$ is a constant. For suitable choices of $\mathcal{C}$ and $\zeta$, for a strip of a given width $N$, the equilibrium particle density is approximately uniform for $\zeta < n < N - \zeta$; see Fig. 3.10(a). The corresponding current profile in the topological phase shows clearly separated edge currents that are broadened due to the smooth confinement potential; see Fig. 3.10(b). In contrast to the case of hard wall boundaries [1], the bulk also contains longitudinal Hall currents if it corresponds to a topological phase with non-zero Chern number. These arise due to the effective transverse electric field generated by the harmonic potential.

Following a quantum quench, the edge currents spread towards the interior of the sample, as found in the case of hard wall boundaries [1]; see Fig. 3.11. The currents also

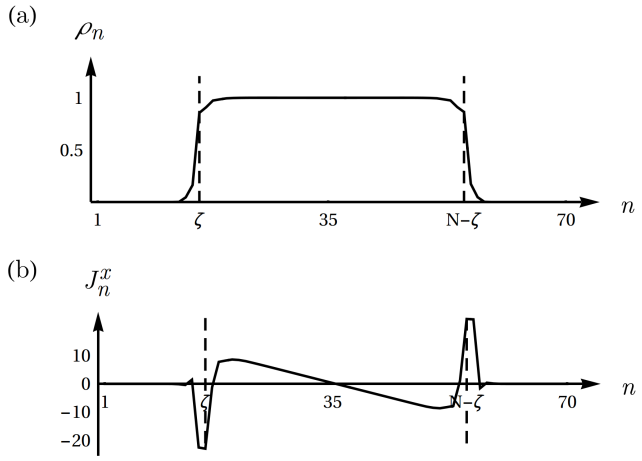


Figure 3.10: Equilibrium properties of the Haldane model in the cylindrical geometry shown in Fig. 3.7, with an additional harmonic confinement potential $V_n$ given by Eq. (3.14). We consider the topological phase with $M = 0$ and $\varphi = \pi/3$ and set $N = 70$, $\mathcal{C} = 1.2$ and $\zeta = 15$. (a) Particle density $\rho_n$ as a function of the row index $n \in 1, ..., 70$. At half-filling, the potential confines the particles into the region $\zeta < n < N - \zeta$, as indicated by the vertical dashed lines. This imposes an effective system size in which it is possible to observe edge effects. (b) Total longitudinal current $J_n^x$ along the cylinder showing clearly separated edge currents, broadened due to the smooth potential. Hall currents exist in the interior of the sample due to the effective electric field generated by the trap.

spread outside the initial sample area to a lesser extent due to the harmonic confinement; see also Fig. 3.12. The light-cone propagation is clearly visible in the presence of the trap, but the apparent speed of light differs slightly from the uniform case. This is attributed to the broadening of the edge current profiles and the presence of the equilibrium bulk Hall currents, induced by the harmonic potential.

The case of fully open boundary conditions presents a significant increase in the numerical computations required, but is not expected to lead to different results. In the presence of a rotationally symmetric harmonic trap, as shown in Fig. 3.13(a), broadened edge currents will flow on the effective sample boundaries; see Fig. 3.13(b). Likewise, equilibrium bulk Hall currents will also circulate (in the opposite sense to the edge

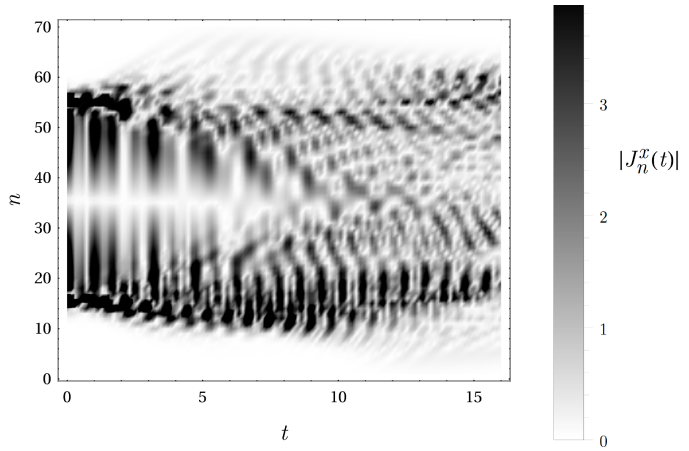


Figure 3.11: Dynamics of the currents $|J_n^x(t)|$ following a quantum quench from the topological phase with $M = 0$ and $\varphi = \pi/3$ to the non-topological phase $M = 3$ and $\varphi = \pi/3$. We set $N = 70$, $\mathcal{C} = 1.2$ and $\zeta = 15$. The spreading of the currents into the interior (and to a lesser extent the exterior) of the effective sample is visible even in the presence of the harmonic potential. However, the propagation speed departs from the effective speed of light, due to the broadening of the edge currents and the contribution of bulk Hall currents.

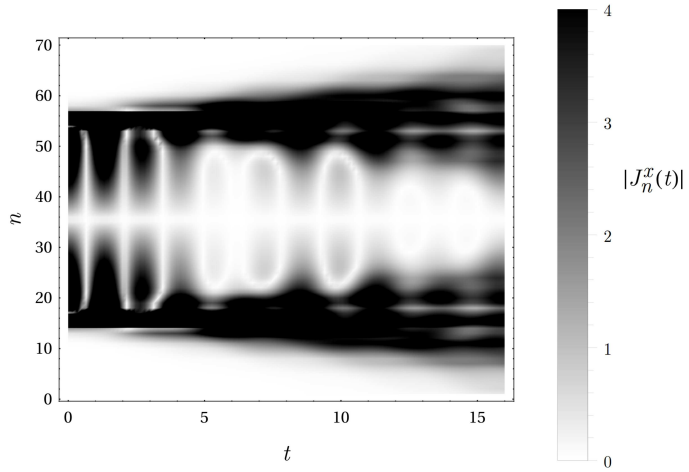


Figure 3.12: Dynamics of the currents $|J_n^x(t)|$ following the instantaneous release of the confining potential, for fixed $M = 0$, $\varphi = \pi/3$, and $N = 70$. We start with $\mathcal{C} = 1.2$ and $\zeta = 15$, and, at time $t = 0$, we switch off the trapping potential, i.e. we set $\mathcal{C} = 0$. The edge currents, initially localised around $n = \xi$ and $n = N - \xi$, spread towards the interior and the exterior of the sample. Simultaneously, the bulk Hall currents in the $x$-direction, due to the potential trap $V(y)$, are suppressed.

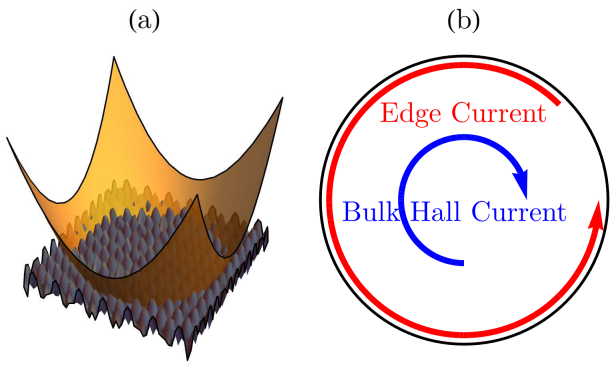


Figure 3.13: (a) Illustration of the potential landscape of a hexagonal optical lattice in the presence of a rotationally symmetric harmonic trap. (b) Circulating equilibrium currents in the resulting disk geometry. Following a quantum quench between the topological and the non-topological phases the edge currents are expected to propagate into the interior (and the exterior) of the sample at the effective speed of light. This will be smoothed out due to the broadening of the edge currents and the presence of the bulk Hall currents.

currents) due to the effective radial electric field. Following a quantum quench, the edge currents will flow towards the interior of the sample, exhibiting light-cone propagation; this will be smoothed out by the edge current broadening and the bulk Hall currents, which are present even in equilibrium.

An estimate of the timescales for the light-cone propagation can be inferred from the experimental parameters used for the realisation of the Haldane model [59]. Using the typical hopping parameter $t_1 \sim 10^2\, h\text{Hz}$, the effective speed of light is $c \sim 10^3\, a/\text{s}$, measured in inter-site spacings per second. Lattice site propagation occurs on millisecond timescales. The timescale for observing the onset of the current plateau in Fig. 3.8, and the light-cone propagation in Fig. 3.11, is thus of the order of several milliseconds; the unit of time in Figs 3.8 and 3.11 is $\hbar/t_1 \sim 10^{-3}\,\text{s}$. This is comparable with the timescales explored in experiment [59].

## 3.5 Summary

In this Chapter, we have explored the transport properties of Chern insulators following a quantum quench in an isolated system undergoing unitary evolution. The Hall conductance is no longer described by the ground-state relation $\sigma_{xy}(0) = \nu q^2/h$, in spite of the preservation of $\nu$ in infinite-size systems. This is explained by the fact that the Chern index is a property of the state, while the Hall response depends on both the state and the final Hamiltonian.

By studying finite-size geometries, we have shown that the total edge currents are described by a GGE at late times. It would be interesting to explore the quench dynamics of Chern insulators in experiment, probing their Hall response and the edge current dynamics.

# Chapter 4

# Role of Disorder

A defining characteristic of topological phases of matter is their resilience to *local perturbations* and *sample defects*. So far, we have probed the non-equilibrium response of the Haldane model to *abrupt global perturbations*. A natural question which arises is whether sample defects can affect the non-equilibrium dynamics of Chern insulators. Here, we address this question by studying the Haldane model in the presence of *on-site potential disorder*. The Hamiltonian is given by

$$\begin{aligned}\hat{H} &= -t_1 \sum_{\langle i,j \rangle} \left( \hat{c}_i^\dagger \hat{c}_j + \text{h.c.} \right) - t_2 \sum_{\langle\langle i,j \rangle\rangle} \left( e^{i\varphi_{ij}} \hat{c}_i^\dagger \hat{c}_j + \text{h.c.} \right) \\ &\quad + M \sum_{i \in A} \hat{n}_i - M \sum_{i \in B} \hat{n}_i + \sum_i v_i \hat{n}_i, \end{aligned} \tag{4.1}$$

where[1] $v_i \in [-V, V]$ is a random variable drawn from a flat distribution of width $2V$. The Haldane model, in Eq. (1.15), is retrieved for $V = 0$. For the numerical results shown in the remainder of this Chapter, we set $t_2 = t_1/3$, as done in Chapters 2 and 3.

The inclusion of disorder comes with a number of technical challenges. Not least is the fact that it breaks translational symmetry, and hence prevents us from characterising the topological phases by means of the Chern number defined via integration over momentum

[1] $V$ should not be confused with the potential trap of Chapter 3.

space, Eq. (1.13). However, proposals exist to characterise the Chern insulator phase in disordered systems, ranging from the analysis of the entanglement spectrum [162], to matrix-coupling approaches [163]. Here we use the local "Chern marker" introduced by Bianco and Resta [139]. This has been used successfully in equilibrium for clean and disordered systems [139, 164], and out of equilibrium for clean systems [135].

In this Chapter[2], after briefly introducing the Chern marker, we discuss the evolution of the equilibrium phase diagram with increasing disorder strength. We then study the dynamics following quantum quenches between different points of the phase diagram. In contrast to the global Chern index, which is preserved under unitary evolution in clean systems [1], the local Chern marker undergoes non-trivial dynamics in both clean and disordered samples. Similarly to the non-equilibrium dynamics of the edge currents discussed in Chapter 2, following a quantum quench, the local Chern marker spreads from the boundaries of the finite-size sample towards the interior. However, this spreading is inhibited by the presence of disorder.

## 4.1 Topological Characterisation in Coordinate Space

In order to define the local "Chern marker" [139], let us go back to the Chern number, as defined in Eq. (1.13) for a toroidal infinite-size system, and rewrite it as [13]

$$\nu = -\frac{1}{\pi}\mathrm{Im}\sum_{p}^{\mathrm{occ}}\int_{BZ} d\mathbf{k}\,\langle\partial_{k_x}\psi_{p\mathbf{k}}|\partial_{k_y}\psi_{p\mathbf{k}}\rangle, \tag{4.2}$$

where $\psi_{p\mathbf{k}}(\mathbf{r}) = e^{-i\mathbf{k}\cdot\mathbf{r}}\phi_{p\mathbf{k}}(\mathbf{r})$ is the periodic part of the occupied Bloch states. Note that we have slightly changed the notation; with respect to Eq. (1.13), here we substitute $|\psi(k)\rangle$ with $|\psi_{p\mathbf{k}}(\mathbf{r})\rangle$. This choice is motivated by the necessity of labelling the band $p$ and keeping the spatial dependence explicit. For free-electron systems, the ground

[2]The results presented in this Chapter are currently being prepared for publication [3], in collaboration with Dr M. J. Bhaseen, Prof. N. R. Cooper, and Dr G. Möller.

state is uniquely determined by the ground-state projector operator $P(\mathbf{r}, \mathbf{r}')$ which, for insulators, is exponentially decreasing with $|\mathbf{r} - \mathbf{r}'|$. The idea is that, by writing the Chern number in terms of this projector, it is possible to define a local topological marker in real space. By inserting a complete set of states in Eq. (4.2), we obtain

$$\nu = -\frac{1}{\pi}\mathrm{Im}\sum_{p}^{\mathrm{occ}}\sum_{q}^{\mathrm{unocc}}\int_{BZ} d\mathbf{k}\,\langle\partial_{k_x}\psi_{p\mathbf{k}}|\psi_{q\mathbf{k}}\rangle\langle\psi_{q\mathbf{k}}|\partial_{k_y}\psi_{p\mathbf{k}}\rangle \tag{4.3}$$

where the missing terms are real. Although the position operator is ill-defined in the case of periodic boundary conditions, it is still possible to define its non-diagonal matrix elements as [165]

$$\langle\phi_{q\mathbf{k}}|\hat{\mathbf{r}}|\phi_{p\mathbf{k}}\rangle = i\langle\psi_{q\mathbf{k}}|\partial_{\mathbf{k}}\psi_{p\mathbf{k}}\rangle \tag{4.4}$$

such that

$$\begin{aligned}\nu &= -\frac{A_c}{4\pi^3}\mathrm{Im}\sum_{p}^{\mathrm{occ}}\sum_{q}^{\mathrm{unocc}}\int_{BZ} d\mathbf{k}\int_{BZ} d\mathbf{k}'\langle\phi_{p\mathbf{k}}|\hat{x}|\phi_{q\mathbf{k}'}\rangle\langle\phi_{q\mathbf{k}'}|\hat{y}|\phi_{p\mathbf{k}}\rangle \\ &= -\frac{4\pi}{A_c}\mathrm{Im}\mathrm{Tr}(\hat{P}\hat{x}\hat{Q}\hat{y})\end{aligned} \tag{4.5}$$

where $A_c$ is the area of the unit cell. For $\mathbf{k} \neq \mathbf{k}'$, the matrix elements vanish and, in the second line, we recognise the projectors $\hat{P} = \frac{A_c}{(2\pi)^2}\sum_p^{\mathrm{occ}}\int_{BZ} d\mathbf{k}\,|\phi_{p\mathbf{k}}\rangle\langle\phi_{p\mathbf{k}}|$ and $\hat{Q} = 1 - \hat{P}$ onto the occupied and empty states, respectively. A real-space formula, similar to Eq. (4.5), can be found in earlier work by Kitaev [166].

The pivotal point to define the Chern marker is to realise that the trace in Eq. (4.5) is independent of the representation. Using simple properties of projectors and of the trace, we obtain the Chern marker $\nu(\mathbf{r})$ as [139]

$$\nu(\mathbf{r}) = \frac{2\pi i}{A_c}\langle\mathbf{r}|\left(\hat{x}_P\hat{y}_Q - \hat{y}_P\hat{x}_Q\right)|\mathbf{r}\rangle \tag{4.6}$$

where $\hat{x}_P = \hat{P}\hat{x}\hat{Q}$, $\hat{y}_Q = \hat{Q}\hat{y}\hat{P}$, and the Chern number can be retrieved as $\nu =$

$\lim_{V\to\infty}\frac{1}{V}\int_V d\mathbf{r}\,\nu(\mathbf{r})$. The local Chern marker shares some similarities with the Bott index [167] used in Refs [131, 132]. However, no rigorous matching of the two exists. Out of equilibrium, the Chern marker is computed via Eq. (4.6), using the projector $\hat{P}(t)$ onto the time-evolved Slater determinant.

Even though we exploited periodic boundary conditions whilst defining the Chern marker, it has been shown in Ref. [139] that this Chern marker can also be used to characterise topological phases in finite-size samples. Here, we characterise the state by averaging the Chern marker $\nu(\mathbf{r})$ over a sub-region $\mathfrak{V}$ of the finite-size sample:

$$\mathfrak{C} = \sum_{\mathbf{r}\in\mathfrak{V}} \frac{1}{\mathcal{N}}\nu(\mathbf{r}), \tag{4.7}$$

where $\mathcal{N}$ is the number of sites in the sub-region $\mathfrak{V}$, see Fig. 4.1. We further define $\overline{\mathfrak{C}}$, where the bar indicates an average over $N_V$ different realisations of the disorder. In the following numerical results, we fix $N_V = 20$. For convenience in the site-indexing of the numerical computations, the finite-size geometry we use has a diamond shape; see Fig. 4.1. Note that it is important for $\mathfrak{V}$ to be smaller than the sample, as the integral of $\nu(\mathbf{r})$ over the whole finite-size sample necessarily has to vanish [139]. In fact, $\mathrm{Im}\mathrm{Tr}(\hat{P}\hat{x}\hat{Q}\hat{y})$ in Eq. (4.5) can be rewritten as $\frac{1}{2i}\mathrm{Tr}[\hat{P}\hat{x}\hat{P},\hat{P}\hat{y}\hat{P}]$ and the trace of a commutator vanishes. However, this argument is only valid for finite-size samples, as $\mathrm{Tr}[\hat{P}\hat{x}\hat{P},\hat{P}\hat{y}\hat{P}]$ is not well defined in the presence of periodic boundary conditions. As a consequence, looking at the value of the Chern marker, say for values of $M$ and $\varphi$ which, in the infinite-size system, correspond to a topological phase with $\nu = 1$, one finds that $\nu(\mathbf{r}) \sim 1$ in the bulk of the sample and becomes largely negative on the boundaries, such that the total Chern number vanishes; see Fig. 4.2. If the sub-region $\mathfrak{V}$ is far enough from the boundary region of the sample, the averaged Chern marker $\mathfrak{C}$ will not be affected by them, and, in the limit of large $\mathfrak{V}$, it will capture the bulk topological characteristic.

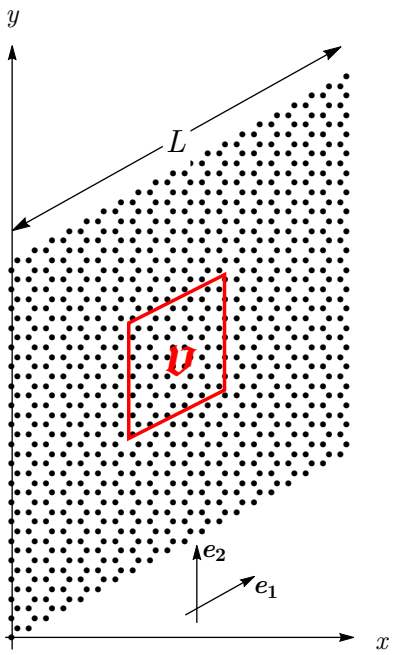


Figure 4.1: Finite-size diamond shape geometry used to compute the local Chern marker $\nu(\mathbf{r})$. $\mathbf{e}_1$ and $\mathbf{e}_2$ are the directions of the primitive vectors of the honeycomb lattice. The lattice is composed of a total of $N = 2\,l^2$ sites, where $l$ is the number of unit cells in the $\mathbf{e}_1$ and $\mathbf{e}_2$ directions. $L = \sqrt{3}\,a\,l$ is the length of the sample, where $a = 1$ is the lattice spacing. The averaged Chern marker $\mathfrak{C}$ is computed as the average over the $\mathcal{N}$ sites belonging to the sub-region $\mathfrak{V}$ (red diamond).

## 4.2 Equilibrium Phase Diagram

Before interrogating the response of the Chern marker to global quantum quenches, we first study the behaviour of the Chern marker at equilibrium. First we want to verify that, in the absence of disorder, the phase diagram calculated in this fashion agrees with the phase diagram of the clean Haldane model. Comparing Fig. 4.3(a) with the phase diagram of Fig. 1.5, we observe that, away from the phase boundaries ($M/t_2 = \pm 3\sqrt{3}\sin\varphi$), the averaged Chern marker agrees with the quantised values $\nu = 0, \pm 1$ of the clean Haldane model. A vertical slice through the phase diagram shows clear plateaus, with values of $\overline{\mathfrak{C}}$ close to integers; see Fig. 4.4. In the region close to the boundaries of the topological phases, $\overline{\mathfrak{C}}$ is not quantised, but instead goes smoothly

from $\overline{\mathfrak{C}} = \pm 1$ to 0, due to the finite-size of the sample. As pointed out in Ref. [139], near the phase transitions, the effective size of the boundary region increases and it is not possible to distinguish the bulk from the edges; see Fig. 4.2. Indeed, at the phase transition, the bulk gap closes and the notion of well-defined edge energy states ceases to exist, as they become indistinguishable from the bulk energy states of the bands. This suggests that, at the phase transition, independently of the ratio between the area of $\mathfrak{V}$ and the total area of the sample, the averaged Chern marker ceases to be a good estimator of the topology of the state.

The smearing of the phase boundary increases with increasing disorder strength, see Fig. 4.3, where the phase diagram $(M, \varphi)$ is plotted for different values of the disorder $V$. In Fig. 4.4, we specialise to the case $\varphi = \pi/2$, and study the variation of $\overline{\mathfrak{C}}$ for $M \in (0, 3)$, increasing the disorder strength $V = 0, 0.5, 1, 1.5$ and 2, in units of $t_1$. With

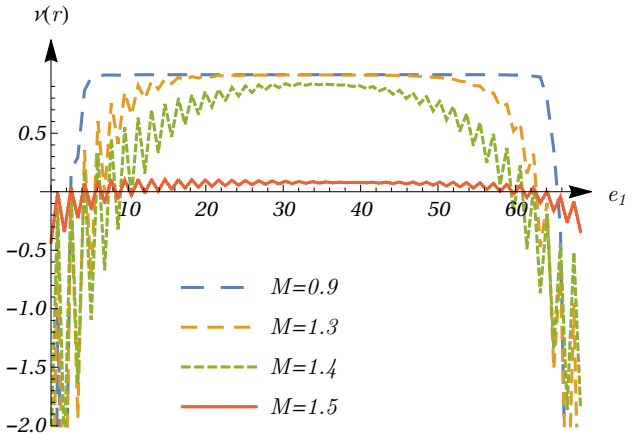


Figure 4.2: Local Chern marker $\nu(\mathbf{r})$ for a cut through the centre of the sample in the direction $\mathbf{e}_1$, showing the broadening of the boundary region near the phase transition. In the figure, $e_1$ is the coordinate in the $\mathbf{e}_1$ direction. We set $t_1 = 1$, $t_2 = 1/3$, $V = 0$, and $\varphi = \pi/3$. Far from the transition ($M = 0.9$), it is possible to clearly distinguish a bulk region, with $\nu(\mathbf{r}) \sim 1$, from the boundary regions. An increase of $M$ towards the transition ($M = 1.5$), makes the boundary region infiltrate the bulk. It follows that, independently of the size of $\mathfrak{V}$, $\mathfrak{C}$ is not pinned at unity close to the transition. This figure, necessary for our discussion, reproduces Fig. 4 from Ref. [139].

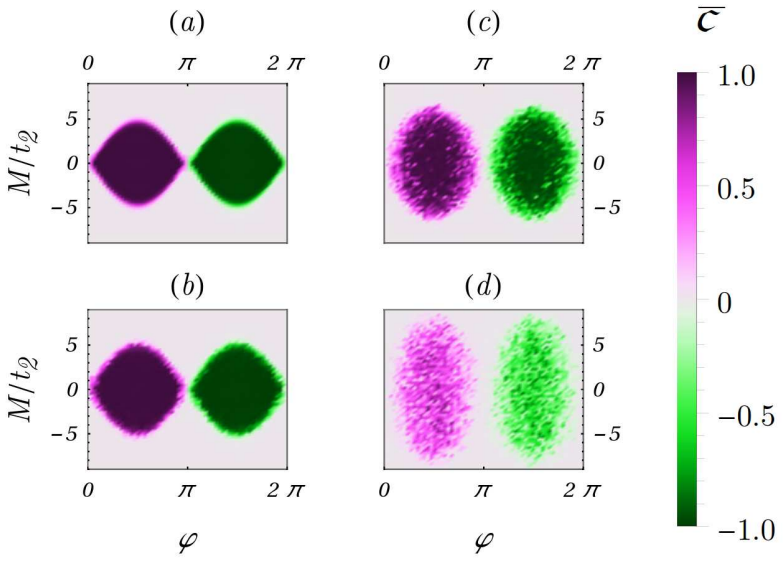


Figure 4.3: Exact diagonalisation results for the spatially and disorder averaged Chern marker $\overline{\mathfrak{C}}$ with increasing disorder strength. The results are obtained for a sub-region with $\mathcal{N} = 288$ sites in an $N = 512$ site sample, for fixed $t_2 = t_1/3$ and (a) $V = 0$, (b) $V = t_1$, (c) $V = 2t_1$, and (d) $V = 3t_1$. The data in panel (a) are consistent with the equilibrium phase diagram of the clean Haldane model.

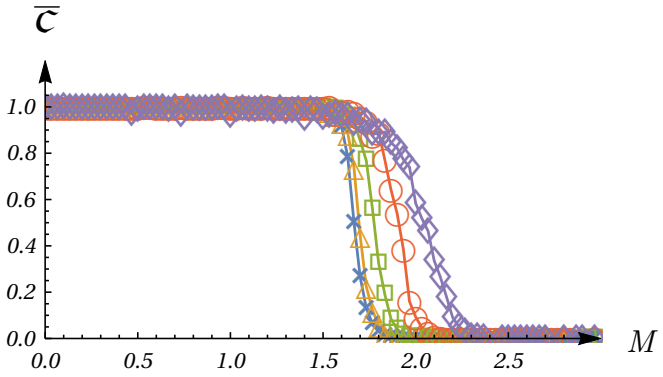


Figure 4.4: Exact diagonalisation results for the disordered Haldane model. Spatially and disorder averaged local Chern marker $\overline{\mathfrak{C}}$ as a function of $M$, for a sub-region of $\mathcal{N} = 512$ sites in an $N = 2048$ site sample, with fixed $\varphi = \pi/2$. The disorder strength is $V = 0$ (crosses), $0.5t_1$ (triangles), $1.0t_1$ (squares), $1.5t_1$ (circles), and $2t_1$ (diamonds). The value of $\overline{\mathfrak{C}}$ shows clear plateaus at 0 and 1.

increasing disorder, the size of the region where the averaged Chern marker $\overline{\mathfrak{C}}$ fails to give a quantised value increases, making it harder to establish a definite transition point between the topological and non-topological phases. Nonetheless, $\overline{\mathfrak{C}}$ provides a good characterisation of the phases, away from the transition.

For the clean Haldane model, we fit the spatially averaged Chern marker of Fig. 4.4, obtained through exact diagonalisation, to Fermi functions $1/(1+\exp[k(M-M_0)])$. This is a standard fitting choice to characterise discrete, logic (0 or 1) quantities. This allows us to define, for each system size, an effective transition point as the midpoint of the Fermi function, $M_0$. In Fig. 4.5, we show the fitted Fermi functions for data obtained with the size of $\mathfrak{V}$ kept fixed, and increasing total system size $N$. By increasing the

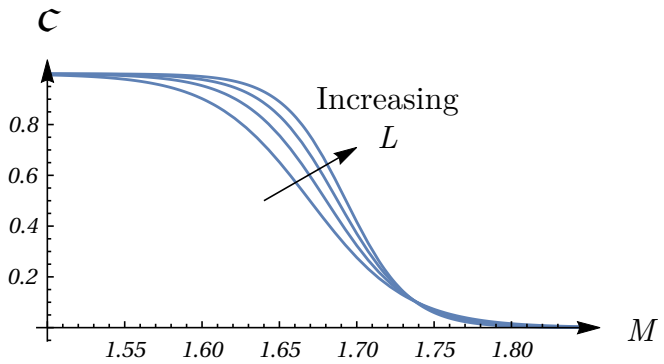


Figure 4.5: Fermi functions $1/(1+\exp[k(M-M_0)])$ resulting from the fitting of $\mathfrak{C}$ for the clean Haldane model, corresponding to $V=0$. Here, we fix $\varphi=\pi/2$ and $\mathcal{N}=512$. Increasing the total system size (from left to right $N=2048, 2592, 3200, 3872$) makes the transition sharper.

system size, the transition region shrinks and the transition becomes sharper. In Fig. 4.6, we show that the effective transition point $M_0$ varies as $1/L$, where $L$ is the system size shown in Fig. 4.1. The extrapolation of the transition point to the thermodynamic limit agrees with the exact transition point of the clean Haldane model; see Fig. 4.6. As the disorder strength is increased, the topological regions of the phase diagram appear to expand slightly, as illustrated in Figs. 4.3(b) and (c). This is consistent with the extrapolation in the thermodynamic limit shown in Fig. 4.7. Similar behaviour was

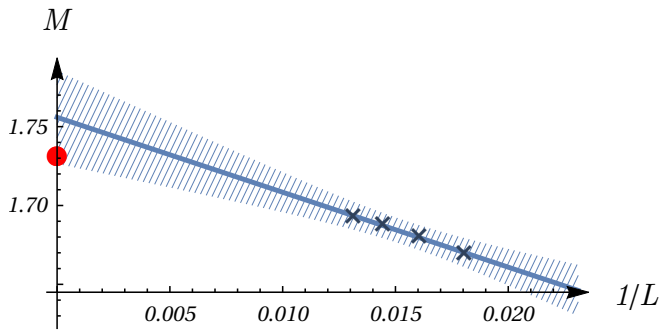


Figure 4.6: Effective transition point $M_0$ as a function of the system size (crosses), for the topological to non-topological phase boundary, with $V = 0$ and $\varphi = \pi/2$. The extrapolation of the transition point to the thermodynamic limit is compatible with the exact result for the clean Haldane model (red dot). The shaded region corresponds to a 99% confidence interval for the linear regression.

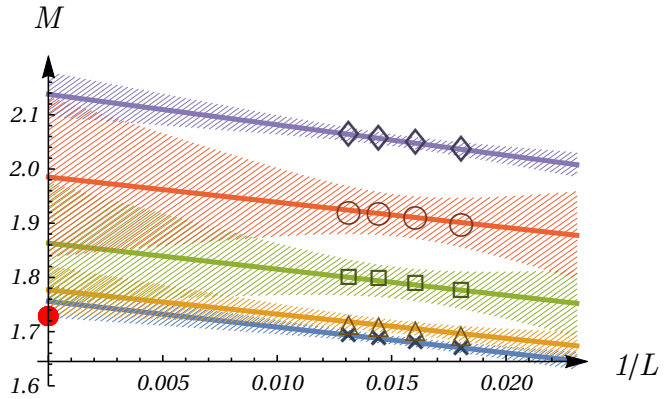


Figure 4.7: Extrapolation to the thermodynamic limit of the topological to non-topological phase boundary as in Fig. 4.6, for $V = 0, 0.5, 1, 1.5, 2$ in units of $t_1$. The shaded areas correspond to 99% confidence intervals for the linear regression. The data are compatible with a slight expansion of the topological regions of the phase diagram with increasing weak disorder, as suggested by Fig. 4.3. However, stronger disorder ultimately destroys the topological phases. The red dot corresponds to the exact location of the transition in the clean Haldane model.

observed in Ref. [168].

For stronger disorder, it becomes harder to infer the presence or absence of well defined phases and of a sharp transition; see Fig. 4.3(d). Indeed, disorder is ultimately expected to destroy the topological phases. In Fig. 4.8, we show the value of $\overline{\mathfrak{C}}$ as a

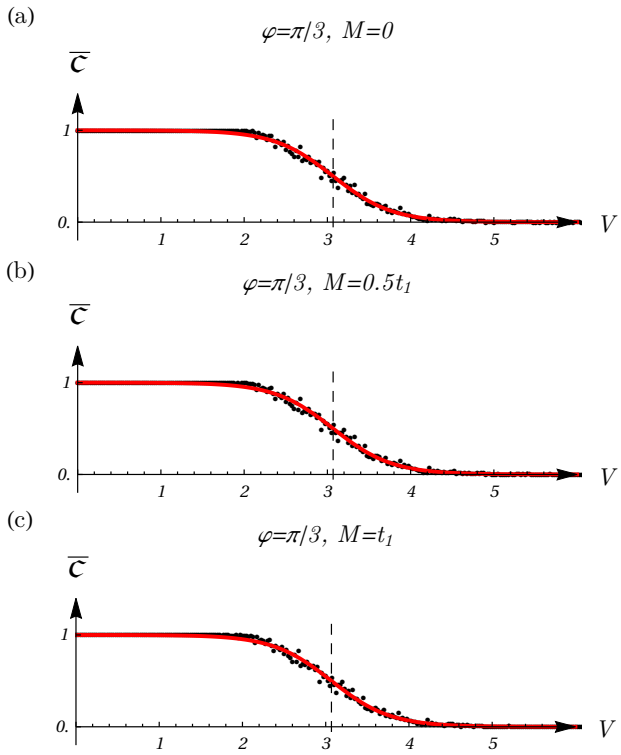


Figure 4.8: Spatially and disorder averaged Chern marker $\overline{\mathfrak{C}}$ as a function of the disorder strength $V$, for fixed values of $M$ and $\varphi$. The system size is fixed to $\mathcal{N} = 288$ and $N = 512$. The solid line is a fit to the Fermi function $1/(1 + \exp[k(V - V_0)])$ where the vertical dashed line corresponds to $V_0$. Increasing the system size does not reduce the transition region; see Fig. 4.9.

function of the disorder strength $V$ for three fixed choices of $\varphi$ and $M$. The value of $\overline{\mathfrak{C}}$ continuously decreases from unity to zero, at the same rate. The transition of $\overline{\mathfrak{C}}$ from unity to zero, as a function of the disorder, does not sharpen up as the system size increases, at least in the tested range of system sizes, and for fixed $\mathfrak{V}$; see Fig. 4.9. If much larger systems could be simulated, one might expect that the transition would approach a step function.

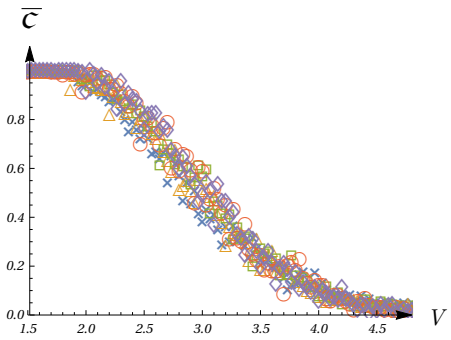


Figure 4.9: Spatially and disorder averaged Chern marker $\overline{\mathfrak{C}}$ as a function of the disorder strength $V$, for fixed values of $M = 0$ and $\varphi = \pi/3$. We fix $\mathcal{N} = 128$ and show results for different values of the system size $N = 512$ (crosses), 648 (triangles), 800 (squares), 968 (circles), and 1152 (diamonds). The data do not show a clear trend towards the sharpening of the phase boundary and do not allow us to obtain an extrapolation as done in Fig. 4.7.

## 4.3 Dynamics of the Local Chern Marker

Having discussed the equilibrium phase diagram of the Haldane model in the presence of on-site potential disorder, we now interrogate the non-equilibrium dynamics of the local Chern marker $\nu(\mathbf{r})$, and of its averaged value $\overline{\mathfrak{C}}$. Here, we perform quenches between the topological and non-topological phases, for fixed values of the disorder strength $V$. In Chapter 2, we saw that the Chern number, in infinite-size systems, is robust under quenches of this kind [1, 132]. However, in spite of this preservation, in the presence of boundaries, observables sensitive to the presence or absence of edge states, such as the longitudinal currents in Chapter 2, undergo non-trivial non-equilibrium dynamics. In contrast to the global Chern number, we find that the local Chern marker shows non-trivial time-dependence. In Fig. 4.10, we consider quenches from the topological to the non-topological phase. It is readily seen that the averaged Chern marker $\overline{\mathfrak{C}}$ initially remains pinned at unity, independently of the disorder strength, until a characteristic time-scale is reached. After this, the time-evolution is dependent on the disorder strength. We observe that increasing the disorder strength hinders changes of the averaged Chern marker, as one might naively expect on physical grounds.

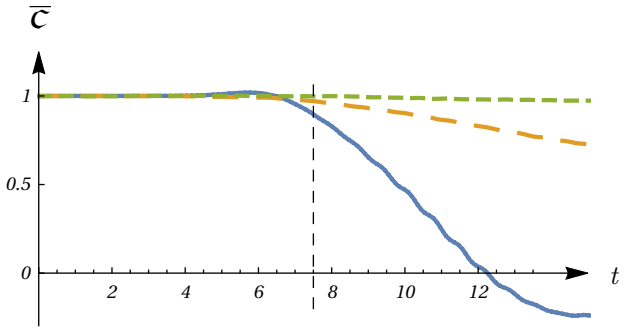


Figure 4.10: Time-evolution of the averaged Chern marker $\overline{\mathfrak{C}}$ after a quantum quench from the topological phase (with $M = 0$) to the non-topological phase (with $M = 5$), with fixed $\varphi = \pi/3$, $t_1 = 1$, $t_2 = 1/3$, $\mathcal{N} = 800$, $N = 3200$, and increasing values of the disorder $V = 0$ (solid), $V = t_1$ (long dashes), $V = 2t_2$ (short dashes). The dashed vertical line corresponds to the time-scale at which a signal, travelling at the maximum speed allowed by the band structure, reaches the area $\mathfrak{V}$, starting from the boundary of the sample. The departure of $\overline{\mathfrak{C}}$ from unity at a slightly earlier time is qualitatively compatible with the fact that at time $t = 0$, the boundary region already penetrates into the interior of the sample. Note that there is a sharp light-cone even in the presence of disorder.

The reason for the initial plateau close to $\overline{\mathfrak{C}} = 1$ in Fig. 4.10 is readily understood from the space-time diagram for the local Chern marker shown in Fig. 4.11. Here, the light-cone propagation of the local Chern marker is reminiscent of the non-equilibrium behaviour of the longitudinal currents in cylindrical geometries shown in Fig. 2.11. From this figure, one can see that most of the spreading happens at the effective speed of light of the Haldane model ($c = 3t_1 a/2\hbar$). However, this is *not* the maximum speed allowed by the exact bands, and the apparent "superluminal" motion is consistent with the band structure; see Fig. 4.10. As discussed above, the boundaries of the topological phases are not well defined due to the broadening of the sample's boundary region close to the phase transition. The non-vanishing size of the transition region in the phase diagram of Fig. 4.3, currently prevents us from simulating quenches between points $(M_0, \varphi_0)$ in the topological phase and $(M, \varphi)$ in the non-topological phase, such that $M_0 - M \ll 1$ and $\varphi_0 - \varphi \ll 1$. It would be possible to simulate these small quenches only if much

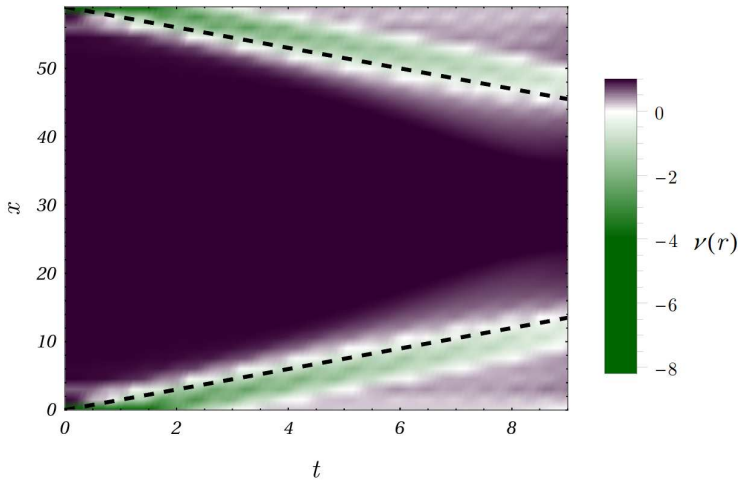


Figure 4.11: Dynamics of the local Chern marker along a cut through the middle of the sample of Fig. 4.1, in the direction $\mathbf{e}_1$, following the same quench depicted in Fig. 4.10, for the clean case corresponding to $V = 0$. Here, we show $\nu(\mathbf{r})$ as a function of the projection of $\mathbf{r}$ onto the $x$-axis. The light-cone propagation of the local Chern marker towards the interior of the sample is reminiscent of the spreading of the currents in Fig. 2.11. The dashed lines correspond to signals propagating at the effective speed of light of the clean Haldane model.

larger system sizes were available. In this case, the quench would only excite low-energy modes in the linear regime of the band structure. If such small quenches were accessible, we would expect the spreading to occur at the effective speed of light $c$. In Fig. 4.12, we show further data for the spreading of the local Chern marker in the interior of the sample, following a quantum quench in the presence of disorder.

## 4.4 Summary

In this Chapter we have studied the role of disorder on the non-equilibrium dynamics of Chern insulators. Characterising the topological phases via the local Chern marker, averaged over space and over disorder realisations, we have examined the equilibrium phase diagram of the disordered Haldane model. For a range of disorder strengths, we found a slight expansion of the topological lobes of the phase diagram. However, the

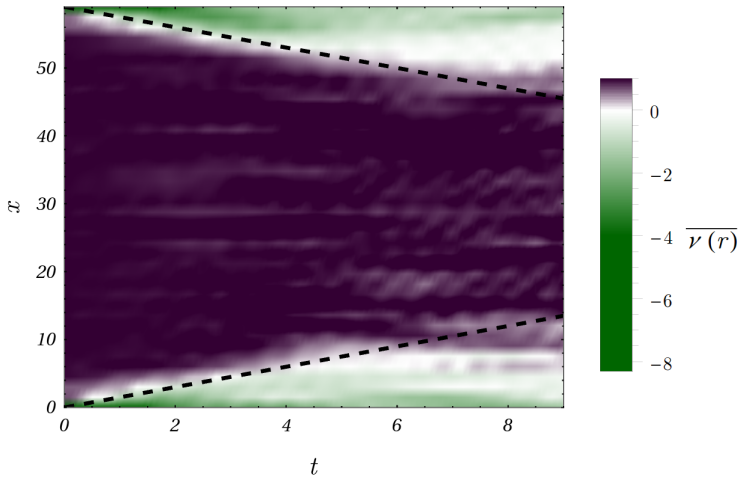


Figure 4.12: Dynamics of the disorder averaged local Chern marker along a cut through the middle of the sample of Fig. 4.1, in the direction $\mathbf{e}_1$, following the same quench depicted in Fig. 4.10, for the disordered case corresponding to $V = t_1$. Here we show $\overline{\nu(\mathbf{r})}$ as a function of the projection of $\mathbf{r}$ onto the $x$-axis. The dashed lines correspond to signals propagating at the effective speed of light of the clean Haldane model. The spreading toward the interior of the sample is inhibited as a result of the disorder.

topological phase is ultimately destroyed for strong disorder. Similar non-monotonic behaviour was also found in Ref. [168].

We also studied the dynamics of the local Chern marker, and of its average over space and disorder realisations. In contrast to the global Chern marker, preserved in infinite-size samples, the local Chern marker displays non-trivial dynamics. In particular, we found a spreading of the local Chern marker towards the interior of the sample, reminiscent of the spreading of the edge currents in Chapter 2. We finally showed that the presence of disorder hinders changes of the local Chern marker, and of its average over space and disorder realisations.

# Chapter 5

# Conclusions

In this thesis, we have discussed the non-equilibrium dynamics of Chern insulators. By focusing on the Haldane model, we have demonstrated that in infinite-size systems, after a quench or a linear sweep, the Chern number remains fixed to its initial quantised value.

In spite of this preservation, we have shown that other physical observables, such as the edge currents and the magnetisation, do change under such a quantum quench. In particular, we showed that, following a quantum quench, the edge currents spread towards the interior of the sample in a light-cone fashion, and that their long-time behaviour is captured by a Generalised Gibbs Ensemble. We confirmed the spreading of the currents for the case of harmonic confinement, relevant for experiments in cold atom settings.

In order to further study the transport properties of the Haldane model, we considered the Hall response. As expected on physical grounds, the Hall conductance changes following a quantum quench, in contrast to the Chern number which remains preserved. The Hall conductance, under the non-equilibrium unitary evolution, is found to be directly related to the non-trivial occupation of the bands. Therefore, the equilibrium TKNN formula does not capture the relation between the preserved Chern number and the changed Hall response, following a quantum quench.

We finally analysed the role of disorder in finite-size Chern insulators. We first examined the phase diagram of the disordered Haldane model. We characterised the phases with the local Chern marker introduced by Bianco and Resta [139], averaged over a sub-region of the system and over multiple disorder realisations. Increasing the disorder strength, we noted a slight expansion of the topological lobes, with respect to the phase diagram of the clean system. However, as expected, a high disorder strength ultimately destroys the topological phase. Lastly, we investigated the non-equilibrium dynamics of the local Chern marker and of its average over space and disorder realisations. As opposed to the global Chern number, which remains fixed to its initial quantised value, the local Chern marker and its averaged value undergo non-trivial dynamics. We observed a light-cone spreading of the Chern marker, reminiscent of the non-equilibrium behaviour of the longitudinal currents.

## 5.1 Work in progress

This thesis focused on the non-equilibrium dynamics of the Chern number and of several *local* observables. Therefore, it is natural to ask about the dynamics of *non-local* observables. For example, one might interrogate the non-equilibrium evolution of the entanglement entropy and/or of the entanglement spectrum[1].

It is well known that the scaling of entanglement entropy of topological systems is given by[2] $S(L) = \alpha L - \gamma + ...$, where the term $\gamma$ is inherent to topological systems, and is known as the *topological entanglement entropy* [169–172]. Here, $\alpha > 0$ is a constant, and the ellipsis represents terms that vanish in the limit of infinite system size, i.e. $L \to \infty$. However, $\gamma$ is vanishing in the case of the integer quantum Hall effect [171]. Thus, it is not immediately clear whether a computation of the non-equilibrium dynamics of

[1] A thorough definition of these observables goes beyond the scope of this thesis. However, a complete discussion of the equilibrium entanglement entropy and spectrum can be found, for example, in Ref. [56].

[2] $\gamma$ should not be confused with the joint index used in Section 3.3.

the entanglement entropy of the Haldane model would give any extra insights into its topological properties.

Nevertheless, a correspondence exists between the energy spectrum of finite-size Chern insulators and the entanglement spectrum of an infinite-size system, where the edge is provided by the entanglement cut [173]. In particular, in the topological phase, both spectra present degenerate edge modes. This holds true also for the broader class of topological insulators. Furthermore, for non-interacting systems, there exists an additional mapping between the entanglement spectrum and the spectrum of the correlation matrix, $C_{\mathcal{R}} = \langle c_i^\dagger c_j \rangle$, with $i, j \in \mathcal{R}$ [174, 175]. Here, $\mathcal{R}$ is the region delimited by the entanglement cut, and the spectrum of $C_{\mathcal{R}}$ is known as the *single-particle entanglement spectrum* [176]. This spectrum also displays degenerate edge states; see Fig. 5.1.

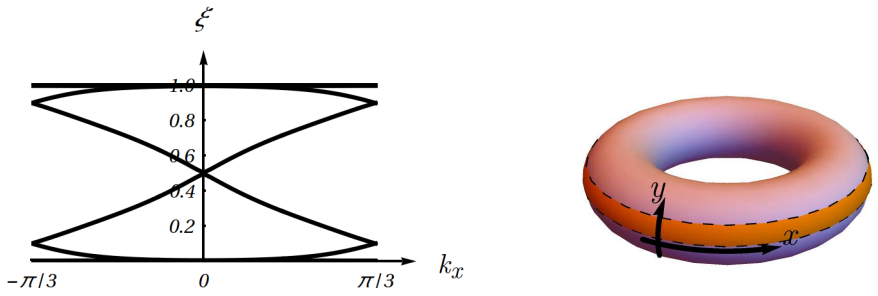


(a) (b)

Figure 5.1: (a) Single-particle entanglement spectrum $\xi$ of the Haldane model in the topological phase with $\varphi = \pi/3$ and $M = 0$. In the topological phase, the spectrum displays degenerate edge states. (b) Torus geometry used to compute the single-particle entanglement spectrum. The dashed lines, corresponding to the entanglement cuts, delimit the region $\mathcal{R}$.

The study of the single-particle entanglement spectrum of the Haldane model following quantum quenches might therefore give extra insights into the non-equilibrium dynamics of Chern insulators. Interesting work on the non-equilibrium dynamics of the entanglement spectrum for Floquet-Chern insulators was recently published [177]. However, it is interesting to study the evolution of the entanglement spectrum for the

Haldane model, so as to decouple the dynamics due to the quench from the driven dynamics of Floquet systems.

Preliminary results show that a quantum quench from the topological phase to the non-topological phase opens a gap in the spectrum. However, the dynamics of the single-particle entanglement spectrum does not have a straightforward interpretation. Work in progress focuses on the characterisation of the time-scales at which the gap opens.

## 5.2 Future Directions

The work presented in this thesis provides a natural starting point for further investigation into the non-equilibrium aspects of topological phases of matter. Building upon this work, one could study the role played by interactions on the non-equilibrium dynamics of the Haldane model. Furthermore, in this thesis, we have shown how disorder hinders changes of the local Chern marker. It would be interesting to examine localisation aspects which might be connected to this inhibition. In this context, one might even interrogate the role of many-body localisation and Anderson localisation in the presence or absence of interactions. Further extensions to our work include the study of the non-equilibrium dynamics of topological insulators. For example, one could focus on quantum quenches in the Kane–Mele model. This would be the next step towards the non-equilibrium dynamics of surface states in three-dimensional topological insulators.

Research is thriving both in the field of topological phases of matter and of non-equilibrium physics. Advances in these areas promise to have a strong impact on future technologies. We believe that part of the excitement is surely given by the experimental advances in cold atom and photonic settings. Our work places itself at the interface between these two areas, and has contributed insights into the non-equilibrium dynamics of Chern insulators.

# Appendix A

# Quantum Hall Effect

In order for this thesis to be self-contained, we provide an overview of the quantum Hall effect; see Fig. A.1. Following Ref. [178], we discuss the Landau quantisation, and the role played by disorder for the appearance of the plateaus in the Hall conductance shown in Fig. 1.

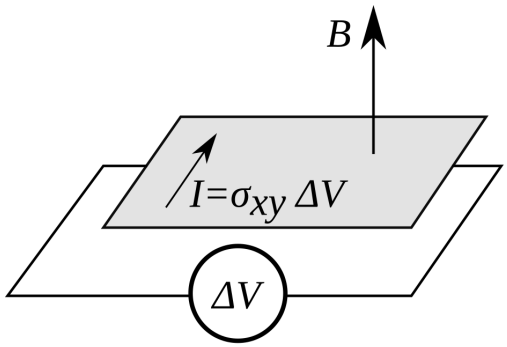


Figure A.1: Schematic setting for the quantum Hall effect. An electron gas confined in a two-dimensional plane is subjected to a strong magnetic field **B** perpendicular to the plane. A voltage difference $\Delta V$ induces a Hall current $I = \sigma_{xy}\Delta V$ in the transverse direction. For strong magnetic fields, the Hall conductance $\sigma_{xy}$ becomes quantised and edge currents are localised on the boundaries of the sample.

## Landau Quantisation

Consider a particle with mass $m$ and charge $q$ in the $x$-$y$ plane, subject to a transverse magnetic field $\mathbf{B} = B\hat{z}$, where $\hat{z}$ is a unit vector in the $z$-direction. In the Hamiltonian, the field is accounted for by the minimal substitution of $\hat{\mathbf{p}} = (\hat{p}_x, \hat{p}_y)$ with $\hat{\mathbf{\Pi}} = (\hat{\Pi}_x, \hat{\Pi}_y) = \hat{\mathbf{p}} - q\hat{\mathbf{A}}$. For the gauge-invariant momentum, $[\hat{\Pi}_x, \hat{\Pi}_y] = iq\hbar B$. Since the Hamiltonian is quadratic in $\hat{\mathbf{\Pi}}$, it is convenient to introduce ladder operators $\hat{a} = \frac{l_B}{\sqrt{2}\hbar}(\hat{\Pi}_x - i\hat{\Pi}_y)$ and $\hat{a}^\dagger = \frac{l_B}{\sqrt{2}\hbar}(\hat{\Pi}_x + i\hat{\Pi}_y)$, such that $[\hat{a}, \hat{a}^\dagger] = 1$ and

$$\hat{H}_B = \hat{\mathbf{\Pi}}^2/2m = \hbar\omega_c(\hat{a}^\dagger\hat{a} + 1/2). \tag{A.1}$$

Here, $\omega_c = \hbar/ml_B^2$ is the cyclotron frequency and $l_B = \sqrt{\hbar/qB}$ is the magnetic length. The corresponding energy levels, known as Landau levels, are those of a harmonic oscillator $\epsilon_n = \hbar\omega_c(n + 1/2)$, with eigenstates $|n\rangle$. Since we have so far identified only one quantum number $n$ and the system is two-dimensional, the Landau levels have to be degenerate. To account for this degeneracy, we introduce the gauge-dependent quantity $\hat{\tilde{\mathbf{\Pi}}} = \hat{\mathbf{p}} + q\hat{\mathbf{A}}$, for which $[\hat{\tilde{\Pi}}_x, \hat{\tilde{\Pi}}_y] = -[\hat{\Pi}_x, \hat{\Pi}_y]$. Since $\hat{\tilde{\mathbf{\Pi}}}$ is gauge-dependent, we have to fix the gauge. For convenience, we choose the symmetric gauge $\hat{\mathbf{A}} = B/2(-\hat{y}, \hat{x}, 0)$. By introducing a second set of ladder operators $\hat{b} = \frac{l_B}{\sqrt{2}\hbar}(\hat{\tilde{\Pi}}_x + i\hat{\tilde{\Pi}}_y)$ and $\hat{b}^\dagger = \frac{l_B}{\sqrt{2}\hbar}(\hat{\tilde{\Pi}}_x - i\hat{\tilde{\Pi}}_y)$, we obtain a second integer quantum number $l$, via $\hat{b}^\dagger\hat{b}\,|l\rangle = l\,|l\rangle$. The Hilbert space is spanned by $|l, n\rangle = |l\rangle \otimes |n\rangle$. Within a semi-classical approach, we can get a physical intuition for this degeneracy. The particle in the strong magnetic field undergoes circular cyclotron motion, and the position operators of the centre of motion are $\hat{X} = \hat{\tilde{\Pi}}_y/qB$ and $\hat{Y} = -\hat{\tilde{\Pi}}_x/qB$ [178]. Since $[\hat{X}, \hat{Y}] = il_B^2$, this guiding centre is smeared out over a surface of area $\Delta X\Delta Y = 2\pi l_B^2$. In a $L \times L$ sample, the degeneracy is then $N_B = L^2/2\pi l_B^2 = L^2qB/h$.

## Importance of Disorder

We shall now see why disorder plays a crucial role in the quantum Hall effect. Let us assume a potential landscape given by a disorder impurity potential, smooth on the scale of the magnetic length. We can therefore write the potential as a function of the position of the guiding centre $\hat{\mathbf{R}} = (\hat{X}, \hat{Y})$, and the Hamiltonian becomes $\hat{H} = \hat{H}_B + U(\hat{\mathbf{R}})$. Because of the translational symmetry breaking disorder, $[\hat{H}, \hat{\mathbf{R}}] = [U(\hat{\mathbf{R}}), \hat{\mathbf{R}}] \neq 0$. The equations of motion for the guiding centre are $i\hbar\dot{\hat{X}} = [\hat{X}, \hat{H}] = il_B^2 \frac{\partial \hat{V}}{\partial \hat{Y}}$ and $i\hbar\dot{\hat{Y}} = [\hat{Y}, \hat{H}] = -il_B^2 \frac{\partial \hat{V}}{\partial \hat{X}}$; i.e. $\dot{\hat{\mathbf{R}}} \perp \nabla V$. From a semi-classical point of view, the guiding centre moves along equipotential lines. For closed equipotential lines, therefore, there is no transport through the sample. However, in the presence of a confining potential, say in the $y$ direction, the equipotential lines on the edges of the sample are open and allow for transport in the $x$ direction; see Fig. A.2. Because the strength of the confining potential,

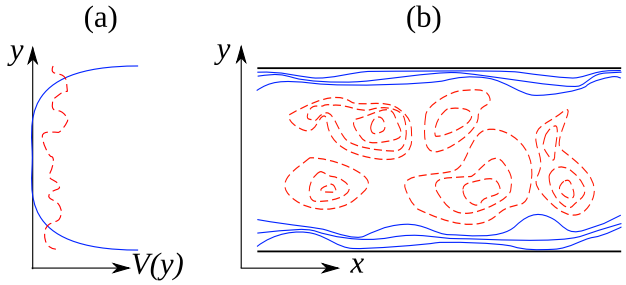


Figure A.2: (a) The potential in the $y$-direction is composed of disorder (dashed) and trapping potential (solid). (b) The equipotential lines corresponding to the disorder potential form closed paths (dashed lines) and do not contribute to charge transport. Those corresponding to the trapping potential are open (solid lines), and contribute to the transport along the edges of the sample.

with translational invariance along the $x$-direction, varies strongly on the edges of the sample, let us treat it from a quantum-mechanical point of view. Choosing the Landau gauge to exploit the translational invariance, one finds that the harmonic oscillator levels are shifted: $\epsilon_{n,k_x} = \hbar\omega_c(n + 1/2) + U(y_0)$, with $y_0 = k_x l_B^2 - \frac{1}{m\omega_c^2} \frac{\partial U_{conf}}{\partial y}\Big|_{y=k_x l_B^2}$ [178]. Notice that with this gauge choice, the degeneracy of the Landau levels (in the absence

of any potential) is given by the momentum vector $k_x = p_x/\hbar = 2\pi l/L$, with integer $l$.

The current carried by a filled Landau level, $J_n^x = q/L \sum_{k_x} \langle n, k_x \,|\, v_x \,|\, n, k_x \rangle$, where $\langle n, k_x \,|\, v_x \,|\, n, k_x \rangle = \frac{1}{\hbar} \frac{\partial \epsilon_{n,k_x}}{\partial k_x} \sim \frac{L}{2\pi\hbar} \frac{\Delta \epsilon_{nl}}{\Delta l}$, is readily found to be $J_n^x = (q^2/h)\Delta V$, where $\Delta V = \Delta U/q$ is the voltage difference between the upper and lower edges of the sample. A completely filled Landau level contributes a quantum of conductance $q^2/h$ to the charge transport. However, the plateaus in the conductance as a function of the magnetic field (and thus of the filling) in Fig. 1 are not yet explained. The plateaus become clear in the semi-classical approximation. The equipotential lines of disorder in the bulk give rise to a landscape of valleys and peaks which is suitable for a percolation interpretation. The idea is that, at low filling of the Landau level, the particles fill the bottom of the valleys and do not contribute to the transport. As the filling is increased, the adjacent "lakes" of particles start merging. At half filling, a transition occurs, and the lakes of particles may be able to join the two sides of the sample, thus contributing to the transport with an extra quantum of conductance; see Fig. A.3.

The stronger the disorder, the broader the plateaus in the Hall conductance. For further and more comprehensive readings on the quantum Hall effect, see Refs. [178–180].

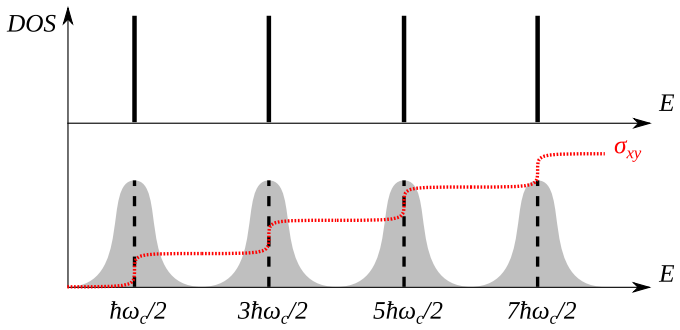


Figure A.3: Density of states without (top) and with (bottom) disorder. In the presence of disorder, the Landau levels broaden. The dotted line is a depiction of the Hall conductance as a function of the filling. At low filling of each broadened Landau level, the particles fill localised states and do not contribute to the transport. At half filling, the particles fill a delocalised state (dashed vertical lines), and thus contribute to the transport with an extra quantum of conductance.

# Appendix B

# Experimental Realisation of the Haldane Model

> *"It doesn't matter how beautiful your theory is, it doesn't matter how smart you are. If it doesn't agree with experiment, it's wrong."*
> Richard Feynman

The interest in the Haldane model has increased substantially, following its experimental realisation using ultracold atoms [59]. The main strength of ultracold atom experiments lies in the possibility of fine-tuning the parameters of the system, from the shape of the lattice structure to the tunnelling amplitudes or the interactions. This makes them ideal to simulate complex quantum mechanical behaviours of real materials. In recent years, great effort has been made to simulate topological phases of matter in cold atom settings; see, for example, Refs. [159, 181–192]. In the following, we review the experimental realisation of the Haldane model performed by Esslinger's group at ETH Zürich.

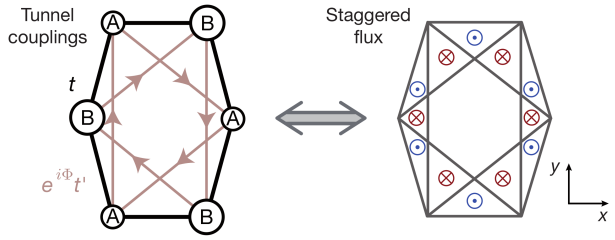


Figure B.1: Unit cell of the Haldane model, as reproduced in the experiment at ETH Zürich. The lattice positions are modulated in time to simulate the presence of the staggered magnetic flux of Haldane's paper. Figure adapted from [59].

## Experiment at ETH Zürich

In the Haldane model, there are two key components: inversion symmetry breaking and time-reversal symmetry breaking. In cold atom experiments, the former is somewhat simpler to implement. It consists in modulating spatially the lattice potential between the $A$ and $B$ lattice sites [193]; see Fig. B.1. This modulation is achieved by frequency-detuning the $\bar{\text{X}}$ and X beams in Fig. B.2. However, the feature of the Haldane model

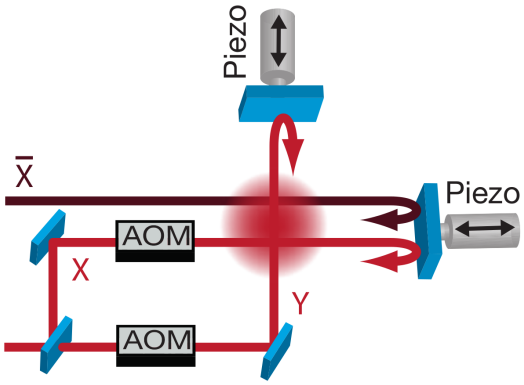


Figure B.2: Laser beam set-up for the experimental realisation of the Haldane model. A frequency detuning between the $\bar{\text{X}}$ and X laser beams breaks the inversion symmetry between the $A$ and $B$ sites of Fig. B.1. Two retro-reflecting mirrors are mounted on piezo-electric actuators, to control the phase shift of the reflected beams. The shaking of the lattice introduced by the moving mirrors gives rise to the phase in the next-to-nearest neighbour hopping parameter of the Haldane model. Figure adapted from [59].

which makes its realisation difficult is the phase $\varphi$ in the next-to-nearest neighbour hopping parameter. This phase is responsible for the time-reversal symmetry breaking, and provides the interesting physics of the model. In Haldane's original paper [57], he assumed this phase to be an Aharonov–Bohm phase resulting from a staggered magnetic field. However, one of the problems of this approach is that the atoms are electrically neutral. Nevertheless, the technical challenge to create the required complex tunnelling parameter in the optical lattice was overcome by modulating (or "shaking") the lattice [65, 66] via circular polarisation of the lattice positions; see Fig. B.2. The resulting gap in the energy spectrum is probed by driving Landau-Zener transitions at the Dirac points. A constant force in one direction (say the $x$-direction) is applied, giving rise to Bloch oscillations. After one full Bloch oscillation, it is possible to measure the fraction of particles in the upper band with band mapping techniques [193]. The number of particles excited to the upper band is an indicator of the size of the band gap, and has a maximum when the gap is vanishing; see Fig. B.3. This is in qualitative agreement

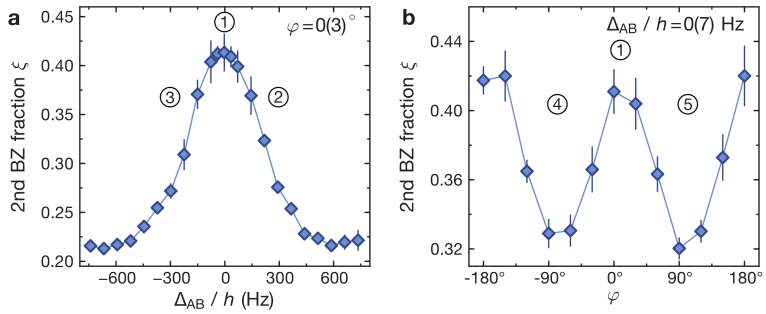


Figure B.3: Experimental measurement of the fraction of particles in the upper band $\xi$ following the application of a constant force for the duration of a Bloch oscillation. Here, $\xi$ is measured as a function of (a) the energy offset between $A$ and $B$ sub-lattices, with fixed $\varphi = 0$, and (b) the phase $\varphi$ of the next-to-nearest neighbour hopping, keeping the energy offset fixed to zero. The maxima correspond to a vanishing band gap. Figure adapted from [59].

with the phase boundaries of the Haldane model. However, the energy spectrum alone is not enough to measure the Berry curvature. As shown in Refs. [157, 158, 194, 195],

the impact of a non-trivial Berry curvature on the equations of motion is analogous to having a magnetic field in momentum space. To measure the Berry curvature, a force $F_y$ is applied, in the $y$-direction. As particles move in quasi-momentum space, they acquire a drift velocity in the transverse direction $v^x_{\mathbf{k}}(F_y) \propto F_y \Omega(\mathbf{k})$. In order to avoid measuring other sources of orthogonal-drift [196, 197], they measure the drift resulting from $F_y$ and $-F_y$ [158]. In the topological phase, $v^x_{\mathbf{k}}(F_y) - v^x_{\mathbf{k}}(-F_y) \propto 2F_y\Omega(\mathbf{k})$, and is zero otherwise. By looking at this *differential drift* $\mathcal{D}(k)$, they retrieve the phase diagram shown in Fig. B.4.

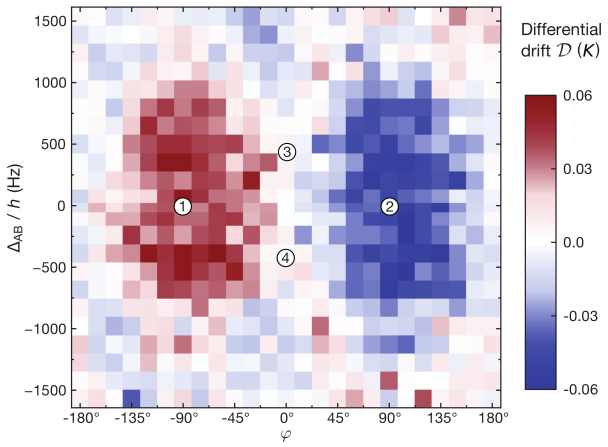


Figure B.4: Experimental data for the differential drift $\mathcal{D}(k)$ in quasi-momentum space as a function of the energy offset $\Delta_{AB} = M$ between the sub-lattices $A$ and $B$, and of the phase $\varphi$ of the next-to-nearest neighbour hopping. The differential drift is measured in order to probe the non-trivial Berry curvature of the topological phases. Indeed, comparing the data with Fig. 1.5, we see that the differential drift, corresponding to opposite senses of the Hall effect, well represents the presence of a non-trivial Chern number. Figure adapted from [59].

# Appendix C

# Edge Currents and Orbital Magnetisation

In this Appendix, we give further details about the equilibrium properties of the edge currents and of the orbital magnetisation of the Haldane model. In order to examine the behaviour of the edge currents we consider the Haldane model on a finite-size strip with armchair edges and periodic (open) boundary conditions along (transverse to) the strip. The geometry we use is shown in Fig. C.1. The numerical computations in the main text are performed on strips of width $N = 20$, 30 or 40 unit cells. For a tight binding model, the total current operator is computed as the time derivative of the polarisation operator $\hat{\mathbf{P}} = \sum_j \mathbf{R}_j \hat{n}_j$, i.e. $\mathbf{J} = i[\hat{H}, \hat{\mathbf{P}}]$, as shown for example in Refs. [198, 199]. Clearly, the only term of the Hamiltonian which contributes to the commutator is the kinetic one and we find $\hat{\mathbf{J}} = -i \sum_{lj} t_{lj}\, \boldsymbol{\delta}_{li}\, \hat{c}_l^\dagger \hat{c}_j$, where $\boldsymbol{\delta}_{jl} = \mathbf{R}_l - \mathbf{R}_j$ is the vector that goes from site $l$ to $j$. We are interested in the current along the x-direction

$$\hat{J}^x = -i \sum_{lj} t_{lj}\, \delta^x_{jl}\, \hat{c}_l^\dagger \hat{c}_j \tag{C.1}$$

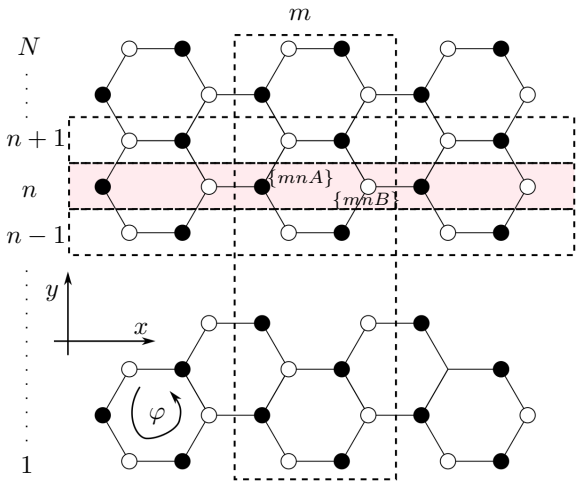


Figure C.1: The strip geometry used for the finite-size computations. The strip is $N$ cells wide with arm chair edges and has periodic (open) boundary conditions in the longitudinal (transverse) directions. Each unit cell is labelled by two indices $m$ and $n$, and contains two sites belonging to the $A$ or $B$ sub-lattices. The phase $\varphi$ of the Haldane model is taken as positive for anticlockwise next-to-nearest neighbour hopping.

with $t_{lj} = t_1$ for $l, j$ being nearest neighbours, $t_{lj} = t_2 e^{i\phi_{lj}}$ for next-to-nearest neighbours and $t_{lj} = 0$ otherwise. The indices $l, j$ are each a triplet $\{m, n, s\}$ which label the $x$ and $y$ positions of the unit cell, and the sub-lattice $s = A, B$ of the site within the unit cell. We define the local current flowing through one site as

$$\hat{J}^x_l = -\frac{i}{2}\sum_j \delta^x_{jl}(t_{lj}\hat{c}^\dagger_l \hat{c}_j - t_{jl}\hat{c}^\dagger_j \hat{c}_l) \quad (= \hat{J}^x_{mns}) \tag{C.2}$$

where we have used $t^\dagger_{lj} = t_{jl}$. We also define the longitudinal current operator flowing along the $n$-th row of the strip, where $n \in 1, \ldots, N$ as shown by the shaded area in Fig. C.1, as

$$\hat{J}^x_n = \sum_{ms} \hat{J}^x_{mns} = -\frac{i}{2}\sum_{ms}\sum_{m'n's'} \delta^x_{m'n's',mns}(t_{mns,m'n's'}\hat{c}^\dagger_{mns}\hat{c}_{m'n's'} - \text{h.c.}). \tag{C.3}$$

We exploit the periodic boundary conditions along $x$ by taking its Fourier transform. The annihilation operator can be decomposed in Fourier modes as

$$\hat{c}_{mns} = \frac{1}{\sqrt{L_x}} \sum_{k_x} e^{ik_x R^x_{mns}} \hat{c}_{ns}(k_x). \tag{C.4}$$

The longitudinal current operator is thus explicitly given by

$$\begin{aligned}
\hat{J}^x_n = \sum_{k_x} \hat{J}^x_n(k_x) = \sum_{k_x} \Bigg\{ & \frac{it_1}{2} \left[ e^{ik_x} \hat{c}^\dagger_{nA}(k_x) \hat{c}_{nB}(k_x) - \text{h.c.} \right] \\
& - \frac{it_1}{4} \left[ e^{-\frac{i}{2}k_x} \hat{c}^\dagger_{nA}(k_x) \hat{c}_{n+1B}(k_x) + e^{-\frac{i}{2}k_x} \hat{c}^\dagger_{nA}(k_x) \hat{c}_{n-1B}(k_x) - \text{h.c.} \right] \\
& + \frac{it_1}{4} \left[ e^{\frac{i}{2}k_x} \hat{c}^\dagger_{nB}(k_x) \hat{c}_{n+1A}(k_x) + e^{\frac{i}{2}k_x} \hat{c}^\dagger_{nB}(k_x) \hat{c}_{n-1A}(k_x) - \text{h.c.} \right] \\
& - \frac{3}{2} t_2 \sin\left(\frac{3}{2}k_x\right) \Big[ e^{-i\varphi} \hat{c}^\dagger_{nA}(k_x) \hat{c}_{n+1A}(k_x) + e^{i\varphi} \hat{c}^\dagger_{nA}(k_x) \hat{c}_{n-1A}(k_x) \\
& \qquad e^{i\varphi} \hat{c}^\dagger_{nB}(k_x) \hat{c}_{n+1B}(k_x) + e^{-i\varphi} \hat{c}^\dagger_{nB}(k_x) \hat{c}_{n-1B}(k_x) + \text{h.c.} \Big] \Bigg\},
\end{aligned} \tag{C.5}$$

where we have set the lattice spacing to unity. The Hamiltonian, in the same basis, takes the form

$$\begin{aligned}
\hat{H} = \sum_{k_x, n} \Big\{ & t_1 \Big[ e^{ik_x} \hat{c}^\dagger_{nA}(k_x) \hat{c}_{nB}(k_x) + e^{-\frac{i}{2}k_x} \hat{c}^\dagger_{nA}(k_x) \hat{c}_{n+1B}(k_x) \\
& + e^{-\frac{i}{2}k_x} \hat{c}^\dagger_{nA}(k_x) \hat{c}_{n-1B}(k_x) + e^{-ik_x} \hat{c}^\dagger_{nB}(k_x) \hat{c}_{nA}(k_x) + e^{\frac{i}{2}k_x} \hat{c}^\dagger_{nB}(k_x) \hat{c}_{n+1A}(k_x) \\
& + e^{\frac{i}{2}k_x} \hat{c}^\dagger_{nB}(k_x) \hat{c}_{n-1A}(k_x) \Big] + 2t_2 \cos\left(\frac{3}{2}k_x\right) \Big[ e^{-i\varphi} \hat{c}^\dagger_{nA}(k_x) \hat{c}_{n+1A}(k_x) \\
& + e^{i\varphi} \hat{c}^\dagger_{nA}(k_x) \hat{c}_{n-1A}(k_x) + e^{i\varphi} \hat{c}^\dagger_{nB}(k_x) \hat{c}_{n+1B}(k_x) + e^{-i\varphi} \hat{c}^\dagger_{nB}(k_x) \hat{c}_{n-1B}(k_x) \Big] \\
& + t_2 \Big[ e^{i\varphi} \hat{c}^\dagger_{nA}(k_x) \hat{c}_{n+2A}(k_x) + e^{-i\varphi} \hat{c}^\dagger_{nA}(k_x) \hat{c}_{n-2A}(k_x) + e^{-i\varphi} \hat{c}^\dagger_{nB}(k_x) \hat{c}_{n+2B}(k_x) \\
& + e^{i\varphi} \hat{c}^\dagger_{nB}(k_x) \hat{c}_{n-2B}(k_x) \Big] + M \left[ \hat{c}^\dagger_{nA}(k_x) \hat{c}_{nA}(k_x) - \hat{c}^\dagger_{nB}(k_x) \hat{c}_{nB}(k_x) \right] \Big\}.
\end{aligned} \tag{C.6}$$

As shown in Fig. C.2, the terms in the summation of Eq. (C.5) appear with both positive and negative signs. In particular, the edge currents, $\langle \hat{J}^x_1 \rangle$ and $\langle \hat{J}^x_N \rangle$, receive

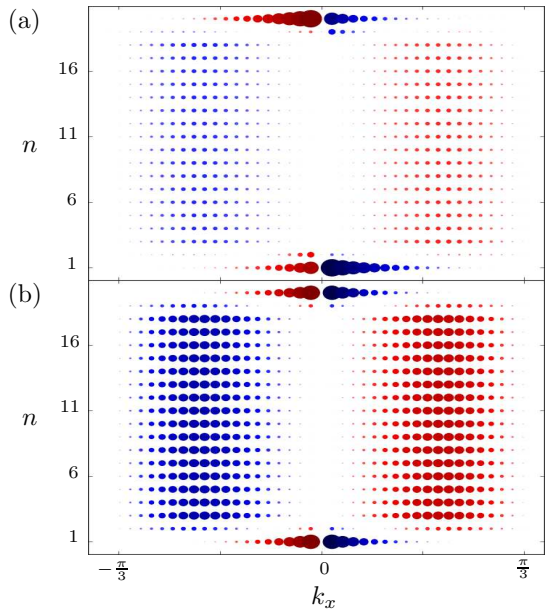


Figure C.2: Momentum space contributions to the equilibrium currents along the strip, $\langle \hat{J}^x_n(k_x) \rangle$, with $N = 20$, $t_1 = 1$, $t_2 = 1/3$ and $M = 0$. For clarity, the size of the dots is proportional to the fourth power of $\langle \hat{J}^x_n(k_x) \rangle$ and the blue (red) dots indicate negative (positive) values. (a) $\varphi = \pi/3$ showing counter-propagating contributions to the currents. The net currents vanish in the bulk but are non-zero close to the edges; see Fig. 2.6(a). (b) $\varphi = \pi/2$ showing balanced contributions throughout the strip, leading to $\langle \hat{J}^x_n \rangle = 0$.

opposite contributions which perfectly cancel when $\varphi = \pi/2$. Doping the system with particles or holes breaks this symmetry and restores the $2\pi$-periodicity, as shown in Fig. C.3. The effect of doping is to change the relative contributions of the bulk and the edge states to the total edge currents; for particle (hole) doping the edge (bulk) states contribute more to the overall edge current.

Zeros of the orbital magnetisation also occur within the topological phases. As shown in Fig. C.4, $\boldsymbol{\mathcal{M}}(M, \varphi)$ has extrema at $M = 0$ and on the boundaries of the topological phases at $M = \pm\sqrt{3}\sin\varphi$. Numerically we observe that the zeros of $\boldsymbol{\mathcal{M}}$ occur on the sinusoidal loci $M = \pm\sin\varphi$. Once again, the effect of doping is to change the relative contributions of the bulk and the edge states to the orbital magnetisation; for particle

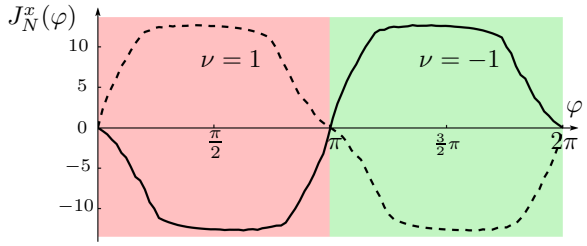


Figure C.3: Equilibrium edge current $J_N^x$ for $N = 20$, $t_1 = 1$, $t_2 = 1/3$ and $M = 0$ with a 5% particle (solid) or hole (dashed) doping. In contrast to the half-filled case shown in Fig. 2.6(b), the currents no longer vanish at $\varphi = \pi/2$. Instead, the currents have the same periodicity as the Hamiltonian. The increase or decrease of the edge current at $\varphi = \pi/2$ reflects both the sign of the doping and the Chern index.

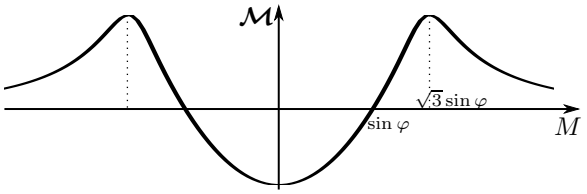


Figure C.4: Orbital magnetisation $\boldsymbol{\mathcal{M}}$ with $N = 20$, $t_1 = 1$, $t_2 = 1/3$ and $\varphi = \pi/3$. Numerically we observe that $\boldsymbol{\mathcal{M}}$ vanishes within the topological phases when $M = \pm\sin\varphi$. We also observe that $\boldsymbol{\mathcal{M}}$ has extrema for $M = 0$ and $M = \pm\sqrt{3}\sin\varphi$; the latter correspond to the boundaries of the topological phases as indicated by the dotted lines.

(hole) doping the edge (bulk) states contribute more to $\boldsymbol{\mathcal{M}}$.

# Bibliography


[1] M. D. Caio, N. R. Cooper, and M. J. Bhaseen, "Quantum Quenches in Chern Insulators," Phys. Rev. Lett. **115**, 236403 (2015).

[2] M. D. Caio, N. R. Cooper, and M. J. Bhaseen, "Hall response and edge current dynamics in Chern insulators out of equilibrium," Phys. Rev. B **94**, 155104 (2016).

[3] M. D. Caio, "Non-equilibrium Dynamics of Disordered Chern Insulators," Prep. (2017).

[4] L. D. Landau, "On the theory of phase transitions," Zh. Eksp. Teor. Fiz. **7**, 19 (1937).

[5] L. D. Landau and V. L. Ginzburg, "On the theory of superconductivity (in Russian)," Zh. Eksp. Teor. Fiz. **20**, 1064 (1950).

[6] J. M. Kosterlitz and D. J. Thouless, "Long range order and metastability in two dimensional solids and superfluids. (Application of dislocation theory)," J. Phys. C Solid State Phys. **5**, L124 (1972).

[7] J. M. Kosterlitz and D. J. Thouless, "Ordering, metastability and phase transitions in two-dimensional systems," J. Phys. C Solid State Phys. **6**, 1181 (1973).

[8] D. J. Bishop and J. D. Reppy, "Study of the Superfluid Transition in Two-Dimensional $^4$He Films," Phys. Rev. Lett. **40**, 1727 (1978).

[9] T. Ando, Y. Matsumoto, and Y. Uemura, "Theory of Hall Effect in a Two-Dimensional Electron System," J. Phys. Soc. Japan **39**, 279 (1975).

[10] K. Klitzing, G. Dorda, and M. Pepper, "New Method for High-Accuracy Determination of the Fine-Structure Constant Based on Quantized Hall Resistance," Phys. Rev. Lett. **45**, 494 (1980).

[11] Nobelprize.org, "Press Release: The 1998 Nobel Prize in Physics," R. Swedish Acad. Sci. (1998).

[12] R. Laughlin, "Quantized Hall conductivity in two dimensions," Phys. Rev. B **23**, 5632 (1981).

[13] D. Thouless, M. Kohmoto, M. Nightingale, and M. den Nijs, "Quantized Hall Conductance in a Two-Dimensional Periodic Potential," Phys. Rev. Lett. **49**, 405 (1982).

[14] D. C. Tsui, H. L. Stormer, and A. C. Gossard, "Two-Dimensional Magnetotransport in the Extreme Quantum Limit," Phys. Rev. Lett. **48**, 1559 (1982).

[15] R. B. Laughlin, "Anomalous Quantum Hall Effect: An Incompressible Quantum Fluid with Fractionally Charged Excitations," Phys. Rev. Lett. **50**, 1395 (1983).

[16] V. J. Goldman and B. Su, "Resonant Tunneling in the Quantum Hall Regime: Measurement of Fractional Charge," Science **267** (1995).

[17] R. De-Picciotto, M. Reznikov, M. Heiblum, V. Umansky, G. Bunin, and D. Mahalu, "Direct observation of a fractional charge," Nature **389**, 162 (1997).

[18] L. Saminadayar, D. C. Glattli, Y. Jin, and B. Etienne, "Observation of the $e/3$ Fractionally Charged Laughlin Quasiparticle," Phys. Rev. Lett. **79**, 2526 (1997).

[19] F. D. M. Haldane, "Nonlinear Field Theory of Large-Spin Heisenberg Antiferromagnets: Semiclassically Quantized Solitons of the One-Dimensional Easy-Axis Néel State," Phys. Rev. Lett. **50**, 1153 (1983).

[20] F. Haldane, "Continuum dynamics of the 1-D Heisenberg antiferromagnet: Identification with the O(3) nonlinear sigma model," Phys. Lett. A **93**, 464 (1983).

[21] W. J. L. Buyers, R. M. Morra, R. L. Armstrong, M. J. Hogan, P. Gerlach, and K. Hirakawa, "Experimental evidence for the Haldane gap in a spin-1 nearly isotropic, antiferromagnetic chain," Phys. Rev. Lett. **56**, 371 (1986).

[22] M. Kenzelmann, R. A. Cowley, W. J. L. Buyers, Z. Tun, R. Coldea, and M. Enderle, "Properties of Haldane excitations and multiparticle states in the antiferromagnetic spin-1 chain compound $CsNiCl_3$," Phys. Rev. B **66**, 244071 (2002).

[23] C. L. Kane and E. J. Mele, "Quantum Spin Hall Effect in Graphene," Phys. Rev. Lett. **95**, 226801 (2004).

[24] C. L. Kane and E. J. Mele, "Z2 topological order and the quantum spin Hall effect," Phys. Rev. Lett. **95**, 146802 (2005).

[25] B. A. Bernevig and S.-C. Zhang, "Quantum Spin Hall Effect," Phys. Rev. Lett. **96**, 106802 (2006).

[26] B. A. Bernevig, T. L. Hughes, and S.-C. Zhang, "Quantum spin Hall effect and topological phase transition in HgTe quantum wells," Science **314**, 1757 (2006).

[27] M. König, S. Wiedmann, C. Brüne, A. Roth, H. Buhmann, L. W. Molenkamp, X.-L. Qi, and S.-C. Zhang, "Quantum spin hall insulator state in HgTe quantum wells," Science **318**, 766 (2007).

[28] L. Fu, C. L. Kane, and E. J. Mele, "Topological Insulators in Three Dimensions," Phys. Rev. Lett. **98**, 106803 (2007).

[29] D. Hsieh, D. Qian, L. Wray, Y. Xia, Y. S. Hor, R. J. Cava, and M. Z. Hasan, "A topological Dirac insulator in a quantum spin Hall phase," Nature **452**, 970 (2008).

[30] A. P. Schnyder, S. Ryu, A. Furusaki, and A. W. W. Ludwig, "Classification of topological insulators and superconductors in three spatial dimensions," Phys. Rev. B **78**, 195125 (2008).

[31] M. König, H. Buhmann, L. W. Molenkamp, T. Hughes, C.-X. Liu, X.-L. Qi, and S.-C. Zhang, "The Quantum Spin Hall Effect: Theory and Experiment," J. Phys. Soc. Japan **77**, 031007 (2008).

[32] G. E. Volovik, "Topological invariant for superfluid $^3$He-B and quantum phase transitions," JETP Lett. **90**, 587 (2009).

[33] A. Kitaev, "Periodic table for topological insulators and superconductors," AIP Conf. Proc. **1134**, 22 (2009).

[34] Y. Xia, D. Qian, D. Hsieh, L. Wray, A. Pal, H. Lin, A. Bansil, D. Grauer, Y. S. Hor, R. J. Cava, and M. Z. Hasan, "Observation of a large-gap topological-insulator class with a single Dirac cone on the surface," Nat. Phys. **5**, 18 (2009).

[35] H. Zhang, C.-X. Liu, X.-L. Qi, X. Dai, Z. Fang, and S.-C. Zhang, "Topological insulators in Bi2Se3, Bi2Te3 and Sb2Te3 with a single Dirac cone on the surface," Nat. Phys. **5**, 438 (2009).

[36] J. E. Moore, "The birth of topological insulators," Nature **464**, 194 (2010).

[37] M. Z. Hasan and C. L. Kane, "Colloquium: Topological insulators," Rev. Mod. Phys. **82**, 3045 (2010).

[38] H. Lin, L. A. Wray, Y. Xia, S. Xu, S. Jia, R. J. Cava, A. Bansil, and M. Z. Hasan, "Half-Heusler ternary compounds as new multifunctional experimental platforms for topological quantum phenomena," Nat. Mater. **9**, 546 (2010).

[39] S. Chadov, X. Qi, J. Kübler, G. H. Fecher, C. Felser, and S. C. Zhang, "Tunable multifunctional topological insulators in ternary Heusler compounds," Nat. Mater. **9**, 541 (2010).

[40] X.-L. Qi and S.-C. Zhang, "Topological insulators and superconductors," Rev. Mod. Phys. **83**, 1057 (2011).

[41] K. L. Wang, M. Lang, and X. Kou, "Spintronics of Topological Insulators," in *Handb. Spintron.* (Springer Netherlands, Dordrecht, 2016) pp. 431–462.

[42] C. Nayak, S. H. Simon, A. Stern, M. Freedman, and S. Das Sarma, "Non-Abelian anyons and topological quantum computation," Rev. Mod. Phys. **80**, 1083 (2008).

[43] J. Bardeen, L. N. Cooper, and J. R. Schrieffer, "Microscopic Theory of Superconductivity," Phys. Rev. **106**, 1175 (1957).

[44] N. D. Mermin and H. Wagner, "Absence of Ferromagnetism or Antiferromagnetism in One- or Two-Dimensional Isotropic Heisenberg Models," Phys. Rev. Lett. **17**, 1133 (1966).

[45] P. C. Hohenberg, "Existence of Long-Range Order in One and Two Dimensions," Phys. Rev. **158**, 383 (1967).

[46] S. Coleman, "There are no Goldstone bosons in two dimensions," Commun. Math. Phys. **31**, 259 (1973).

[47] Nobelprize.org, "Scientific Background on the Nobel Prize in Physics 2016," R. Swedish Acad. Sci. (2016).

[48] F. S. Cataliotti, S. Burger, C. Fort, P. Maddaloni, F. Minardi, A. Trombettoni, A. Smerzi, and M. Inguscio, "Josephson Junction Arrays with Bose-Einstein Condensates," Science **293** (2001).

[49] V. L. Berezinskii, "Destruction of Long-range Order in One-dimensional and Two-dimensional Systems Possessing a Continuous Symmetry Group. I. Classical Systems." Zh. Eksp. Teor. Fiz. **32**, 907 (1971).

[50] V. L. Berezinskii, "Destruction of Long-range Order in One-dimensional and Two-dimensional Systems Possessing a Continuous Symmetry Group. II. Quantum Systems." J. Exp. Theor. Phys. **34**, 610 (1971).

[51] K. S. Novoselov, Z. Jiang, Y. Zhang, S. V. Morozov, H. L. Stormer, U. Zeitler, J. C. Maan, G. S. Boebinger, P. Kim, and A. K. Geim, "Room-temperature quantum Hall effect in graphene," Science **315**, 1379 (2007).

[52] S.-S. Chern, "Characteristic Classes of Hermitian Manifolds," Ann. Math. Second Ser. **47**, 85 (1946).

[53] M. V. Berry, "Quantal Phase Factors Accompanying Adiabatic Changes," Proc. R. Soc. A **392**, 45 (1984).

[54] Y. Aharonov and D. Bohm, "Significance of Electromagnetic Potentials in the Quatum Thery," Phys. Rev. **123**, 1511 (1959).

[55] Y. Aharonov and D. Bohm, "Further Considerations on Electromagnetic Potentials in the Quantum Theory," Phys. Rev. **123**, 1511 (1961).

[56] E. Fradkin, *Field Theories of Condensed Matter Physics*, 2nd ed. (Cambridge University Press, 2013).

[57] F. D. M. Haldane, "Model for a Quantum Hall Effect without Landau Levels: Condensed-Matter Realization of the "Parity Anomaly"," Phys. Rev. Lett. **61**, 2015 (1988).

[58] D. R. Hofstadter, "Energy levels and wave functions of Bloch electrons in rational and irrational magnetic fields," Phys. Rev. B **14**, 2239 (1976).

[59] G. Jotzu, M. Messer, R. Desbuquois, M. Lebrat, T. Uehlinger, D. Greif, and T. Esslinger, "Experimental realization of the topological Haldane model with ultracold fermions," Nature **515**, 237 (2014).

[60] N. Goldman, A. Kubasiak, A. Bermudez, P. Gaspard, M. Lewenstein, and M. Martin-Delgado, "Non-Abelian Optical Lattices: Anomalous Quantum Hall Effect and Dirac Fermions," Phys. Rev. Lett. **103**, 035301 (2009).

[61] E. Alba, X. Fernandez-Gonzalvo, J. Mur-Petit, J. K. Pachos, and J. J. Garcia-Ripoll, "Seeing Topological Order in Time-of-Flight Measurements," Phys. Rev. Lett. **107**, 235301 (2011).

[62] M. Aidelsburger, M. Atala, S. Nascimbène, S. Trotzky, Y.-A. Chen, and I. Bloch, "Experimental realization of strong effective magnetic fields in optical superlattice potentials," Appl. Phys. B **113**, 1 (2013).

[63] N. Goldman, E. Anisimovas, F. Gerbier, P. Öhberg, I. B. Spielman, and G. Juzeliūnas, "Measuring topology in a laser-coupled honeycomb lattice: from Chern insulators to topological semi-metals," New J. Phys. **15**, 013025 (2013).

[64] A. R. Wright, "Realising Haldane's vision for a Chern insulator in buckled lattices," Sci. Rep. **3**, 2736 (2013).

[65] T. Oka and H. Aoki, "Photovoltaic Hall effect in graphene," Phys. Rev. B **79**, 081406 (2009).

[66] W. Zheng and H. Zhai, "Floquet topological states in shaking optical lattices," Phys. Rev. A **89**, 061603 (2014).

[67] D. P. DiVincenzo and E. J. Mele, "Self-consistent effective-mass theory for intralayer screening in graphite intercalation compounds," Phys. Rev. B **29**, 1685 (1984).

[68] K. S. Novoselov, "Electric Field Effect in Atomically Thin Carbon Films," Science **306**, 666 (2004).

[69] K. S. Novoselov, A. K. Geim, S. V. Morozov, D. Jiang, M. I. Katsnelson, I. V. Grigorieva, S. V. Dubonos, and A. A. Firsov, "Two-dimensional gas of massless Dirac fermions in graphene," Nature **438**, 197 (2005).

[70] Y. Zhang, Y.-W. Tan, H. L. Stormer, and P. Kim, "Experimental observation of the quantum Hall effect and Berry's phase in graphene," Nature **438**, 201 (2005).

[71] C.-Z. Chang, J. Zhang, X. Feng, J. Shen, Z. Zhang, M. Guo, K. Li, Y. Ou, P. Wei, L.-L. Wang, Z.-Q. Ji, Y. Feng, S. Ji, X. Chen, J. Jia, X. Dai, Z. Fang, S.-C. Zhang, K. He, Y. Wang, L. Lu, X.-C. Ma, and Q.-K. Xue, "Experimental Observation of the Quantum Anomalous Hall Effect in a Magnetic Topological Insulator," Science **340**, 167 (2013).

[72] A. B. Khanikaev, S. H. Mousavi, W.-K. Tse, M. Kargarian, A. H. MacDonald, and G. Shvets, "Photonic topological insulators," Nat. Mater. **12**, 233 (2013).

[73] A. Dutta, R. R. P. Singh, and U. Divakaran, "Quenching through Dirac and semi-Dirac points in optical lattices: Kibble-Zurek scaling for anisotropic quantum critical systems," Europhys. Lett. **89**, 67001 (2010).

[74] B. Dóra and R. Moessner, "Dynamics of the spin Hall effect in topological insulators and graphene," Phys. Rev. B **83**, 073403 (2011).

[75] T. Uehlinger, D. Greif, G. Jotzu, L. Tarruell, T. Esslinger, L. Wang, and M. Troyer, "Double transfer through Dirac points in a tunable honeycomb optical lattice," Eur. Phys. J. Spec. Top. **217**, 121 (2013).

[76] E. Perfetto, "Dynamical Formation and Manipulation of Majorana Fermions in Driven Quantum Wires in Contact with a Superconductor," Phys. Rev. Lett. **110**, 087001 (2013).

[77] R. Barnett, "Edge-state instabilities of bosons in a topological band," Phys. Rev. A **88**, 063631 (2013).

[78] A. A. Patel, S. Sharma, and A. Dutta, "Quench dynamics of edge states in 2-D topological insulator ribbons," Eur. Phys. J. B **86**, 367 (2013).

[79] G. Kells, D. Sen, J. K. Slingerland, and S. Vishveshwara, "Topological blocking in quantum quench dynamics," Phys. Rev. B **89**, 235130 (2014).

[80] P. Hauke, M. Lewenstein, and A. Eckardt, "Tomography of Band Insulators from Quench Dynamics," Phys. Rev. Lett. **113**, 045303 (2014).

[81] L. Stojchevska, I. Vaskivskyi, T. Mertelj, P. Kusar, D. Svetin, S. Brazovskii, and D. Mihailovic, "Ultrafast switching to a stable hidden quantum state in an electronic crystal," Science **344**, 177 (2014).

[82] P. D. Sacramento, "Fate of Majorana fermions and Chern numbers after a quantum quench," Phys. Rev. E **90**, 032138 (2014).

[83] B. Galilo, D. K. Lee, and R. Barnett, "Selective Population of Edge States in a 2D Topological Band System," Phys. Rev. Lett. **115**, 245302 (2015).

[84] J. Deutsch, "Quantum statistical mechanics in a closed system," Phys. Rev. A **43**, 2046 (1991).

[85] M. Srednicki, "Chaos and quantum thermalization," Phys. Rev. E **50**, 888 (1994).

[86] M. Srednicki, "The approach to thermal equilibrium in quantized chaotic systems," J. Phys. A. Math. Gen. **32**, 1163 (1999).

[87] M. Rigol, V. Dunjko, and M. Olshanii, "Thermalization and its mechanism for generic isolated quantum systems," Nature **452**, 854 (2008).

[88] M. Rigol and M. Srednicki, "Alternatives to Eigenstate Thermalization," Phys. Rev. Lett. **108**, 110601 (2012).

[89] T. Kinoshita, T. Wenger, and D. S. Weiss, "A quantum Newton's cradle." Nature **440**, 900 (2006).

[90] M. Greiner, O. Mandel, T. W. Hänsch, and I. Bloch, "Collapse and revival of the matter wave field of a Bose-Einstein condensate," Nature **419**, 51 (2002).

[91] G. D. Chiara, S. Montangero, P. Calabrese, and R. Fazio, "Entanglement entropy dynamics of Heisenberg chains," J. Stat. Mech. Theory Exp. **2006**, P03001 (2006).

[92] P. Calabrese and J. Cardy, "Time Dependence of Correlation Functions Following a Quantum Quench," Phys. Rev. Lett. **96**, 136801 (2006).

[93] C. Kollath, A. M. Läuchli, and E. Altman, "Quench Dynamics and Nonequilibrium Phase Diagram of the Bose-Hubbard Model," Phys. Rev. Lett. **98**, 180601 (2007).

[94] M. Rigol, V. Dunjko, V. Yurovsky, and M. Olshanii, "Relaxation in a Completely Integrable Many-Body Quantum System: An Ab Initio Study of the Dynamics of the Highly Excited States of 1D Lattice Hard-Core Bosons," Phys. Rev. Lett. **98**, 050405 (2007).

[95] M. Moeckel and S. Kehrein, "Interaction Quench in the Hubbard Model," Phys. Rev. Lett. **100**, 175702 (2008).

[96] M. Cramer, C. M. Dawson, J. Eisert, and T. J. Osborne, "Exact Relaxation in a Class of Nonequilibrium Quantum Lattice Systems," Phys. Rev. Lett. **100**, 030602 (2008).

[97] S. R. Manmana, S. Wessel, R. M. Noack, and A. Muramatsu, "Time evolution of correlations in strongly interacting fermions after a quantum quench," Phys. Rev. B **79**, 155104 (2009).

[98] P. Barmettler, M. Punk, V. Gritsev, E. Demler, and E. Altman, "Relaxation of Antiferromagnetic Order in Spin-1/2 Chains Following a Quantum Quench," Phys. Rev. Lett. **102**, 130603 (2009).

[99] P. Calabrese, F. H. L. Essler, and M. Fagotti, "Quantum Quench in the Transverse-Field Ising Chain," Phys. Rev. Lett. **106**, 227203 (2011).

[100] A. Polkovnikov, K. Sengupta, A. Silva, and M. Vengalattore, "Colloquium : Nonequilibrium dynamics of closed interacting quantum systems," Rev. Mod. Phys. **83**, 863 (2011).

[101] V. Yukalov, "Equilibration and thermalization in finite quantum systems," Laser Phys. Lett. **8**, 485 (2011).

[102] S. Trotzky, Y.-A. Chen, A. Flesch, I. P. McCulloch, U. Schollwöck, J. Eisert, and I. Bloch, "Probing the relaxation towards equilibrium in an isolated strongly correlated one-dimensional Bose gas," Nat. Phys. **8**, 325 (2012).

[103] J.-S. Caux and F. H. L. Essler, "Time Evolution of Local Observables After Quenching to an Integrable Model," Phys. Rev. Lett. **110**, 257203 (2013).

[104] J. Eisert, M. Friesdorf, and C. Gogolin, "Quantum many-body systems out of equilibrium," Nat. Phys. **11**, 124 (2015).

[105] J.-S. Caux and R. M. Konik, "Constructing the Generalized Gibbs Ensemble after a Quantum Quench," Phys. Rev. Lett. **109**, 175301 (2012).

[106] R. Schützhold, M. Uhlmann, Y. Xu, and U. R. Fischer, "Sweeping from the Superfluid to the Mott Phase in the Bose-Hubbard Model," Phys. Rev. Lett. **97**, 200601 (2006).

[107] W. S. Bakr, A. Peng, M. E. Tai, R. Ma, J. Simon, J. I. Gillen, S. Fölling, L. Pollet, and M. Greiner, "Probing the superfluid-to-Mott insulator transition at the single-atom level," Science **329**, 547 (2010).

[108] B. Dóra, M. Haque, and G. Zaránd, "Crossover from Adiabatic to Sudden Interaction Quench in a Luttinger Liquid," Phys. Rev. Lett. **106**, 156406 (2011).

[109] A. del Campo and W. H. Zurek, "Universality of phase transition dynamics: Topological defects from symmetry breaking," Int. J. Mod. Phys. A **29**, 1430018 (2014).

[110] S. Braun, M. Friesdorf, S. S. Hodgman, M. Schreiber, J. P. Ronzheimer, A. Riera, M. del Rey, I. Bloch, J. Eisert, and U. Schneider, "Emergence of coherence and the dynamics of quantum phase transitions," Proc. Natl. Acad. Sci. **112**, 201408861 (2015).

[111] P. Calabrese and J. Cardy, "Entanglement and correlation functions following a local quench: a conformal field theory approach," J. Stat. Mech. Theory Exp. **2007**, P10004 (2007).

[112] P. R. Zangara, A. D. Dente, E. J. Torres-Herrera, H. M. Pastawski, A. Iucci, and L. F. Santos, "Time fluctuations in isolated quantum systems of interacting particles," Phys. Rev. E **88**, 032913 (2013).

[113] P. Jurcevic, B. P. Lanyon, P. Hauke, C. Hempel, P. Zoller, R. Blatt, and C. F. Roos, "Quasiparticle engineering and entanglement propagation in a quantum many-body system," Nature **511**, 202 (2014).

[114] M. Cheneau, P. Barmettler, D. Poletti, M. Endres, P. Schauß, T. Fukuhara, C. Gross, I. Bloch, C. Kollath, and S. Kuhr, "Light-cone-like spreading of correlations in a quantum many-body system," Nature **481**, 484 (2012).

[115] N. Fläschner, D. Vogel, M. Tarnowski, B. S. Rem, D.-S. Lühmann, M. Heyl, J. C. Budich, L. Mathey, K. Sengstock, and C. Weitenberg, "Observation of a dynamical topological phase transition," (2016), arXiv:1608.05616 .

[116] A. A. Houck, H. E. Türeci, and J. Koch, "On-chip quantum simulation with superconducting circuits," Nat. Phys. **8**, 292 (2012).

[117] S. Schmidt and J. Koch, "Circuit QED lattices: Towards quantum simulation with superconducting circuits," Ann. Phys. (Berlin) **525**, 395 (2013).

[118] I. Carusotto and C. Ciuti, "Quantum fluids of light," Rev. Mod. Phys. **85**, 299 (2013).

[119] L. Lu, J. D. Joannopoulos, and M. Soljačić, "Topological photonics," Nat. Photonics **8**, 821 (2014).

[120] M. Fitzpatrick, N. M. Sundaresan, A. C. Y. Li, J. Koch, and A. A. Houck, "Observation of a Dissipative Phase Transition in a One-Dimensional Circuit QED Lattice," Phys. Rev. X **7**, 011016 (2017).

[121] K. Le Hur, L. Henriet, A. Petrescu, K. Plekhanov, G. Roux, and M. Schiró, "Many-body quantum electrodynamics networks: Non-equilibrium condensed matter physics with light," Comptes Rendus Phys. **17**, 808 (2016).

[122] M. J. Hartmann, "Quantum simulation with interacting photons," J. Opt. **18**, 104005 (2016).

[123] L. M. Sieberer, M. Buchhold, and S. Diehl, "Keldysh field theory for driven open quantum systems," Reports Prog. Phys. **79**, 096001 (2016).

[124] C. Noh and D. G. Angelakis, "Quantum simulations and many-body physics with light," Reports Prog. Phys. **80**, 016401 (2017).

[125] G. Floquet, "Sur les équations différentielles linéaires à coefficients périodiques," Ann. Sci. l'École Norm. Supérieure **12**, 47 (1883).

[126] N. H. Lindner, G. Refael, and V. Galitski, "Floquet topological insulator in semiconductor quantum wells," Nat. Phys. **7**, 490 (2011).

[127] A. Gómez-León and G. Platero, "Floquet-Bloch Theory and Topology in Periodically Driven Lattices," Phys. Rev. Lett. **110**, 200403 (2013).

[128] J. Cayssol, B. Dóra, F. Simon, and R. Moessner, "Floquet topological insulators," Phys. status solidi - Rapid Res. Lett. **7**, 101 (2013).

[129] M. S. Foster, V. Gurarie, M. Dzero, and E. A. Yuzbashyan, "Quench-Induced Floquet Topological p -Wave Superfluids," Phys. Rev. Lett. **113**, 076403 (2014).

[130] A. G. Grushin, Á. Gómez-León, and T. Neupert, "Floquet Fractional Chern Insulators," Phys. Rev. Lett. **112**, 156801 (2014).

[131] P. Titum, N. H. Lindner, M. C. Rechtsman, and G. Refael, "Disorder-Induced Floquet Topological Insulators," Phys. Rev. Lett. **114**, 056801 (2015).

[132] L. D'Alessio and M. Rigol, "Dynamical preparation of Floquet Chern insulators," Nat. Commun. **6**, 8336 (2015).

[133] H. Dehghani, T. Oka, and A. Mitra, "Out-of-equilibrium electrons and the Hall conductance of a Floquet topological insulator," Phys. Rev. B **91**, 155422 (2015).

[134] H. Dehghani and A. Mitra, "Occupation probabilities and current densities of bulk and edge states of a Floquet topological insulator," Phys. Rev. B **93**, 205437 (2016).

[135] L. Privitera and G. E. Santoro, "Quantum annealing and nonequilibrium dynamics of Floquet Chern insulators," Phys. Rev. B **93**, 241406 (2016).

[136] A. Russomanno and E. G. Dalla Torre, "Kibble-Zurek scaling in periodically driven quantum systems," Europhys. Lett. **115**, 30006 (2016).

[137] T. Kitagawa, E. Berg, M. Rudner, and E. Demler, "Topological characterization of periodically driven quantum systems," Phys. Rev. B **82**, 235114 (2010).

[138] M. C. Rechtsman, J. M. Zeuner, Y. Plotnik, Y. Lumer, D. Podolsky, F. Dreisow, S. Nolte, M. Segev, and A. Szameit, "Photonic Floquet topological insulators," Nature **496**, 196 (2013).

[139] R. Bianco and R. Resta, "Mapping topological order in coordinate space," Phys. Rev. B **84**, 241106 (2011).

[140] M. S. Foster, M. Dzero, V. Gurarie, and E. A. Yuzbashyan, "Quantum quench in a p + i p superfluid: Winding numbers and topological states far from equilibrium," Phys. Rev. B **88**, 104511 (2013).

[141] E. Zhao, N. Bray-Ali, C. J. Williams, I. B. Spielman, and I. I. Satija, "Chern numbers hiding in time-of-flight images," Phys. Rev. A **84**, 063629 (2011).

[142] N. Flaschner, B. S. Rem, M. Tarnowski, D. Vogel, D.-S. Luhmann, K. Sengstock, and C. Weitenberg, "Experimental reconstruction of the Berry curvature in a Floquet Bloch band," Science **352**, 1091 (2016).

[143] N. N. Hao, P. Zhang, Z. G. Wang, W. Zhang, and Y. P. Wang, "Topological edge states and quantum Hall effect in the Haldane model," Phys. Rev. B **78**, 075438 (2008).

[144] M. Atala, M. Aidelsburger, M. Lohse, J. T. Barreiro, B. Paredes, and I. Bloch, "Observation of chiral currents with ultracold atoms in bosonic ladders," Nat. Phys. **10**, 588 (2014).

[145] N. Goldman, J. Dalibard, A. Dauphin, F. Gerbier, M. Lewenstein, P. Zoller, and I. B. Spielman, "Direct imaging of topological edge states in cold-atom systems," Proc. Natl. Acad. Sci. **110**, 6736 (2013).

[146] T. Thonhauser, D. Ceresoli, D. Vanderbilt, and R. Resta, "Orbital Magnetization in Periodic Insulators," Phys. Rev. Lett. **95**, 137205 (2005).

[147] D. Ceresoli, T. Thonhauser, D. Vanderbilt, and R. Resta, "Orbital magnetization in crystalline solids: Multi-band insulators, Chern insulators, and metals," Phys. Rev. B **74**, 024408 (2006).

[148] Q. Niu, D. J. Thouless, and Y.-S. Wu, "Quantized Hall conductance as a topological invariant," Phys. Rev. B **31**, 3372 (1985).

[149] P. Wang and S. Kehrein, "Phase transitions in the diagonal ensemble of two-band Chern insulators," New J. Phys. **18**, 053003 (2016).

[150] P. Wang, M. Schmitt, and S. Kehrein, "Universal nonanalytic behavior of the Hall conductance in a Chern insulator at the topologically driven nonequilibrium phase transition," Phys. Rev. B **93**, 085134 (2015).

[151] Y. Hu, P. Zoller, and J. C. Budich, "Dynamical Buildup of a Quantized Hall Response from Nontopological States," Phys. Rev. Lett. **117**, 126803 (2016).

[152] J. H. Wilson, J. C. W. Song, and G. Refael, "Remnant Geometric Hall Response in a Quantum Quench," Phys. Rev. Lett. **117**, 235302 (2016).

[153] Y. O. Nakagawa, G. Misguich, and M. Oshikawa, "Flux quench in a system of interacting spinless fermions in one dimension," Phys. Rev. B **93**, 174310 (2016).

[154] R. Karplus and J. M. Luttinger, "Hall Effect in Ferromagnetics," Phys. Rev. **95**, 1154 (1954).

[155] W. Kohn and J. M. Luttinger, "Quantum Theory of Electrical Transport Phenomena," Phys. Rev. **108**, 590 (1957).

[156] D. Xiao, M.-C. Chang, and Q. Niu, "Berry phase effects on electronic properties," Rev. Mod. Phys. **82**, 1959 (2010).

[157] M. Chang and Q. Niu, "Berry phase, hyperorbits, and the Hofstadter spectrum," Phys. Rev. Lett. **75**, 1348 (1995).

[158] H. M. Price and N. R. Cooper, "Mapping the Berry curvature from semiclassical dynamics in optical lattices," Phys. Rev. A **85**, 033620 (2012).

[159] M. Aidelsburger, M. Lohse, C. Schweizer, M. Atala, J. T. Barreiro, S. Nascimbène, N. R. Cooper, I. Bloch, and N. Goldman, "Measuring the Chern number of Hofstadter bands with ultracold bosonic atoms," Nat. Phys. **11**, 162 (2014).

[160] T. D. Stanescu, V. Galitski, and S. Das Sarma, "Topological states in two-dimensional optical lattices," Phys. Rev. A **82**, 013608 (2010).

[161] M. Buchhold, D. Cocks, and W. Hofstetter, "Effects of smooth boundaries on topological edge modes in optical lattices," Phys. Rev. A **85**, 063614 (2012).

[162] E. Prodan, T. L. Hughes, and B. A. Bernevig, "Entanglement Spectrum of a Disordered Topological Chern Insulator," Phys. Rev. Lett. **105**, 115501 (2010).

[163] Y.-F. Zhang, Y.-Y. Yang, Y. Ju, L. Sheng, R. Shen, D.-N. Sheng, and D.-Y. Xing, "Coupling-matrix approach to the Chern number calculation in disordered systems," Chinese Phys. B **22**, 117312 (2013).

[164] D.-T. Tran, A. Dauphin, N. Goldman, and P. Gaspard, "Topological Hofstadter insulators in a two-dimensional quasicrystal," Phys. Rev. B **91**, 085125 (2015).

[165] S. Baroni, S. de Gironcoli, A. Dal Corso, and P. Giannozzi, "Phonons and related crystal properties from density-functional perturbation theory," Rev. Mod. Phys. **73**, 515 (2001).

[166] A. Kitaev, "Anyons in an exactly solved model and beyond," Ann. Phys. **321**, 2 (2006).

[167] M. B. Hastings and T. A. Loring, "Topological insulators and $C^*$-algebras: Theory and numerical practice," Ann. Phys. **326**, 1699 (2011).

[168] E. Prodan, "Disordered topological insulators: a non-commutative geometry perspective," J. Phys. A Math. Theor. **44**, 113001 (2011).

[169] A. Hamma, R. Ionicioiu, and P. Zanardi, "Ground state entanglement and geometric entropy in the Kitaev model," Phys. Lett. A **337**, 22 (2005).

[170] A. Hamma, R. Ionicioiu, and P. Zanardi, "Bipartite entanglement and entropic boundary law in lattice spin systems," Phys. Rev. A **71**, 022315 (2005).

[171] A. Kitaev and J. Preskill, "Topological Entanglement Entropy," Phys. Rev. Lett. **96**, 110404 (2006).

[172] M. Levin and X.-G. Wen, "Detecting Topological Order in a Ground State Wave Function," Phys. Rev. Lett. **96**, 110405 (2006).

[173] L. Fidkowski, "Entanglement Spectrum of Topological Insulators and Superconductors," Phys. Rev. Lett. **104**, 130502 (2010).

[174] I. Peschel, "Calculation of reduced density matrices from correlation functions," J. Phys. A. Math. Gen. **36**, L205 (2003).

[175] I. Peschel and V. Eisler, "Reduced density matrices and entanglement entropy in free lattice models," J. Phys. A Math. Theor. **42**, 33 (2009).

[176] M. Legner and T. Neupert, "Relating the entanglement spectrum of noninteracting band insulators to their quantum geometry and topology," Phys. Rev. B **88**, 115114 (2013).

[177] D. J. Yates, Y. Lemonik, and A. Mitra, "Entanglement properties of Floquet-Chern insulators," Phys. Rev. B **94**, 205422 (2016).

[178] M. O. Goerbig, "Quantum Hall Effects," (2009), arXiv:0909.1998 .

[179] S. M. Girvin, "The Quantum Hall Effect: Novel Excitations and Broken Symmetries," (1999), arXiv:9907002 [cond-mat] .

[180] D. Tong, "Lectures on the Quantum Hall Effect," (2016), arXiv:1606.06687 .

[181] M. Aidelsburger, M. Atala, M. Lohse, J. T. Barreiro, B. Paredes, and I. Bloch, "Realization of the Hofstadter Hamiltonian with Ultracold Atoms in Optical Lattices," Phys. Rev. Lett. **111**, 185301 (2013).

[182] H. Miyake, G. A. Siviloglou, C. J. Kennedy, W. C. Burton, and W. Ketterle, "Realizing the Harper Hamiltonian with Laser-Assisted Tunneling in Optical Lattices," Phys. Rev. Lett. **111**, 185302 (2013).

[183] M. Atala, M. Aidelsburger, J. T. Barreiro, D. Abanin, T. Kitagawa, E. Demler, and I. Bloch, "Direct measurement of the Zak phase in topological Bloch bands," Nat. Phys. **9**, 795 (2013).

[184] M. Lohse, C. Schweizer, O. Zilberberg, M. Aidelsburger, and I. Bloch, "A Thouless quantum pump with ultracold bosonic atoms in an optical superlattice," Nat. Phys. **12**, 350 (2015).

[185] S. Nakajima, T. Tomita, S. Taie, T. Ichinose, H. Ozawa, L. Wang, M. Troyer, and Y. Takahashi, "Topological Thouless pumping of ultracold fermions," Nat. Phys. **12**, 296 (2016).

[186] C. Schweizer, M. Lohse, R. Citro, and I. Bloch, "Spin Pumping and Measurement of Spin Currents in Optical Superlattices," Phys. Rev. Lett. **117**, 170405 (2016).

[187] J. Dalibard, F. Gerbier, G. Juzeliūnas, and P. Öhberg, "Colloquium : Artificial gauge potentials for neutral atoms," Rev. Mod. Phys. **83**, 1523 (2011).

[188] N. Goldman, G. Juzeliūnas, P. Öhberg, and I. B. Spielman, "Light-induced gauge fields for ultracold atoms," Reports Prog. Phys. **77**, 126401 (2014).

[189] F. Setiawan, K. Sengupta, I. B. Spielman, and J. D. Sau, "Dynamical Detection of Topological Phase Transitions in Short-Lived Atomic Systems," Phys. Rev. Lett. **115**, 190401 (2015).

[190] N. Goldman, G. Jotzu, M. Messer, F. Görg, R. Desbuquois, and T. Esslinger, "Creating topological interfaces and detecting chiral edge modes in a two-dimensional optical lattice," Phys. Rev. A **94**, 043611 (2016).

[191] N. Goldman, J. C. Budich, and P. Zoller, "Topological quantum matter with ultracold gases in optical lattices," Nat. Phys. **12**, 639 (2016).

[192] S. Mukherjee, A. Spracklen, M. Valiente, E. Andersson, P. Öhberg, N. Goldman, and R. R. Thomson, "Experimental observation of anomalous topological edge modes in a slowly driven photonic lattice," Nat. Commun. **8**, 13918 (2017).

[193] L. Tarruell, D. Greif, T. Uehlinger, G. Jotzu, and T. Esslinger, "Creating, moving and merging Dirac points with a Fermi gas in a tunable honeycomb lattice," Nature **483**, 302 (2012).

[194] A. M. Dudarev, R. B. Diener, I. Carusotto, and Q. Niu, "Spin-Orbit Coupling and Berry Phase with Ultracold Atoms in 2D Optical Lattices," Phys. Rev. Lett. **92**, 153005 (2004).

[195] A. Dauphin and N. Goldman, "Extracting the Chern Number from the Dynamics of a Fermi Gas: Implementing a Quantum Hall Bar for Cold Atoms," Phys. Rev. Lett. **111**, 135302 (2013).

[196] S. Mossmann, A. Schulze, D. Witthaut, and H. J. Korsch, "Two-dimensional Bloch oscillations: a Lie-algebraic approach," J. Phys. A. Math. Gen. **38**, 3381 (2005).

[197] J. M. Zhang and W. M. Liu, "Directed coherent transport due to the Bloch oscillation in two dimensions," Phys. Rev. A **82**, 025602 (2010).

[198] G. D. Mahan, *Many-Particle Physics* (Springer Science & Business Media, 2000) p. 785.

[199] A. L. Kuzemsky, "Electronic Transport in Metallic Systems and Generalized Kinetic Equations," Int. J. Mod. Phys. B **25**, 3071 (2011).